Durham E-Theses

Micro-machined membrane deformable mirrors for cryogenic adaptive optics

Dyson, Harold Michael

How to cite:

Dyson, Harold Michael (2002) *Micro-machined membrane deformable mirrors for cryogenic adaptive optics*, Durham theses, Durham University. Available at Durham E-Theses Online: http://etheses.dur.ac.uk/4164/

Use policy

The full-text may be used and/or reproduced, and given to third parties in any format or medium, without prior permission or charge, for personal research or study, educational, or not-for-profit purposes provided that:

- a full bibliographic reference is made to the original source
- a link is made to the metadata record in Durham E-Theses
- the full-text is not changed in any way

The full-text must not be sold in any format or medium without the formal permission of the copyright holders.

Please consult the full Durham E-Theses policy for further details.

Micro-Machined Membrane Deformable Mirrors for Cryogenic Adaptive Optics

by Harold Michael Dyson

February 2002

Abstract

In this Thesis, the suitability of 37 actuator Micro-machined membrane deformable mirrors (MMDM) for adaptive optics at cryogenic temperatures is evaluated. A method is described to safely cool MMDMs to 78K. The initial surface figures of three MMDMs are examined using a Zygo phase shifting interferometer to evaluate the effects of both evacuating and cooling the MMDM. The cooling process increases the aberrations inherent in the MMDMs' membranes. One of the MMDMs evaluated is found to have intrinsic aberrations sufficiently small to leave substantial dynamic range free for wavefront correction; the available range is determined by the beam diameter being corrected. The influence functions of the actuators of the MMDMs are then examined; the cooling process leaves the form of the influence functions unchanged, but reduces the magnitude by 20%.

The dynamic response is evaluated for MMDMs up to a driving frequency of 500Hz. Evacuation, which removes air damping, has no effect on the dynamic response. Cooling the MMDMs shows a high frequency ringing at a frequency of 2kHz, irrespective of MMDM driving frequency. This effect is very small for the MMDM with the superior initial surface figure, which can be considered to be suitable for operation in a cryogenic adaptive optics system. This was the first demonstration of an adaptive optical element functioning at cryogenic temperatures.

A simulation is developed to demonstrate that an adaptive optics system could be constructed utilising a MMDM and a curvature sensor that corrects wavefronts without a wavefront reconstruction step. This system gives good correction for defocus, coma and spherical aberration, with reasonable correction for astigmatism. Potential avenues for future exploration are discussed, notably the prospect of optimising the design of MMDMs for cryogenic operation.

Micro-Machined Membrane Deformable Mirrors for Cryogenic Adaptive Optics
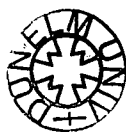
by Harold Michael Dyson

A thesis submitted to the University of Durham

in accordance with the regulations for

admittance to the Degree of Doctor of Philosophy.

Department of Physics

University of Durham

February 2002

− 3 MAY 2002

Thesis
2002/
DYS

Declaration

The work described in this thesis was undertaken between 1998 and 2002 whilst the author was a research student under the supervision of Prof. Ray Sharples and Dr. Nigel Dipper in the Department of Physics at the University of Durham. This work has not been submitted for any other degree at the University of Durham or at any other University.

Portions of this work have appeared in the following paper:

- Dyson H. M., Sharples R. M., Dipper N. A., Vdovin G. V., 2001, Optics Express, **8**, 17 (Chapters 4 and 6).

Acknowledgements

Contents

List of Figures

List of Tables

Chapter 1
Introduction

1.1 Background

The purpose of an astronomical observation is to obtain information about an astronomical object. The principle goal of astronomical instrumentation is to increase the amount of information being collected. The main limitation to the information that can be gathered from a ground-based observation is that the atmosphere itself distorts the incoming light from the astronomical object, a phenomenon called seeing. Adaptive optics (AO) is the science of detecting these distortions and correcting them through some form of adaptive optical element, so that the detector measures the corrected wavefront, and hence the observation has a higher resolution (Hardy 1998, Roddier 1999). AO systems have been deployed on numerous telescopes, for optical and near-infrared observations. A review of astronomical adaptive optics systems for medium-sized telescopes has been conducted by Rigaut (1996). All proposed and existing large ground-based telescopes now include some form of adapative optics system; a summary for the systems on existing large telescopes can be found in Table 2.1. AO systems have yet to be deployed further into the mid–infrared since the adaptive optical element has to be in the optical path leading to the detector, and the infrared emissions from the adaptive optical element would negate the benefits of the AO system. Cryogenic adaptive optics would be advantageous for both ground-based infrared astronomy and space-based astronomy. Space-based systems would not require conventional adaptive optics, since the observations are not taken through a distorting atmosphere, but some form of optical correction will be required for large space-based telescopes (Holota, Vdovin, Collings, Sodnik, Sesselmann and Manhart 1999). A solution to both of these problems is to devise some form of adaptive optical element which functions adequately at cryogenic temperatures, such that it can be utilised in an AO system. One potential solution is discussed in this Thesis. The devices being examined here are micromachined membrane deformable mirrors, kindly donated to this project by OKO Technologies (Vdovin 2001b).

1.2   Aims of this Thesis

The aims of this Thesis are to examine the suitability of micromachined membrane deformable mirrors for wavefront correction at cryogenic temperatures. This involves several stages, outlined below.

In Chapter 2, a summary of the historical development of AO is presented. This proceeds into an exploration of the current state of the art, including a summary of current wavefront sensors and correctors. The motive for cryogenically cooling an AO system is then investigated, before the characteristics of an ideal cryogenic temperature wavefront corrector are explored. Micro-machined Membrane Deformable Mirrors (MMDM) are then introduced, before being evaluated against the criteria of an ideal cryogenic temperature wavefront corrector.

In Chapter 3, the method used to cool the micromachined membrane deformable mirrors is analysed. In particular, the issues that need to be considered when designing a system for the cooling of MMDMs are investigated. A method for remotely sensing the temperature of the MMDMs is also described.

In Chapter 4, static performance measurements of the MMDMs are presented. Quantitative measurements of the variation in the primary Seidel aberrations with membrane temperature are presented for 3 MMDM. Phase maps are then shown for three sets of environmental conditions; room temperature and atmospheric pressure, room temperature and evacuated and evacuated at 78K. The phase maps are used to qualitatively illustrate the initial aberrations inherent in the membranes' surface for each MMDM, and to explore the influence functions of each actuator for each device. Finally, three questions are quantitatively answered through the use of cross-sections through these influence functions. These questions are:

1) Does the influence function for an actuator depend on the azimuthal position of the actuator?

2) What is the effect on an actuators' influence functions of the device being in air or vacuum?

3) What effect does cryogenically cooling the device have on the influence functions of the actuators?

In Chapter 5, dynamic performance measurements of the MMDMs are presented. Here, the dynamic response of the electronics used to drive the MMDMs is quantified.

The effects of evacuation on the dynamic response is then assessed. Finally, the effect on the dynamic response due to cryogenic cooling is evaluated.

In Chapter 6, a simulation is constructed to demonstrate the feasibility of using a curvature wavefront sensor and an MMDM to perform wavefront correction without explicitly reconstructing the wavefront. Various parameters within this system are investigated, such as the effect of the beam diameter. The response of the wavefront sensor to each actuator is then presented, along with the wavefront sensor response to the low-order Zernike aberrations. These are then combined to demonstrate wavefront correction.

Finally, in Chapter 7, conclusions from the preceding Chapters are drawn. Areas for potential future work are then discussed.

Chapter 2

Background

2.1   Active and Adaptive Optics

The resolution of astronomical observations are limited, for all but the very smallest of telescopes, by wavefront distortions introduced as the wavefront passes through the turbulent atmosphere, a phenomenon known as seeing. There are two approaches to prevent this happening. The most obvious is to move the astronomical telescope above the atmosphere, in other words, to put the telescope into space. This approach has been successful, but is not without drawbacks. The most obvious problem is cost; for example, the second servicing mission of HST cost a total of US$448 million for the space shuttle flight alone (Jones and Savage 1997). This was routine maintenance work for an orbital telescope with a 2.4m diameter primary mirror. The total cost for building the two Gemini telescopes, with 8m diameter primary mirrors, is US$184 million (Roche 2000). As can be seen, space-based observatories are an expensive solution to this problem.

The alternative approach is to measure the wavefront distortions introduced by the atmosphere, and to subsequently compensate for the wavefront distortions. Where a wavefront corrector is used to correct the wavefront distortions, this is known as adaptive optics [1]. Active optics is an arbitrarily defined subset of adaptive optics, concentrating on the slowest deformations, and generally only correcting for tip and tilt aberrations. Throughout this thesis, the acronym AO will be used to refer to Active and Adaptive Optics; those parts that relate to only active or only adaptive optics will explicitly state this.

A generic astronomical [2] AO system is depicted in Figure 2.1. The incoming light from both the guide star and the object being studied pass through the turbulent layers of the atmosphere. This light then passes through the optical system of the telescope.

---

[1] Another solution is to only observe when the seeing is at a minimum, by using some system to measure the seeing and only exposing the detector when the seeing is below some threshold value (Platt 1957).

[2] Throughout this thesis, the term 'astronomical AO' will, unless explicitly stated otherwise, refer to non-solar astronomy. For a review of AO for solar astronomy see Rimmele (2000)
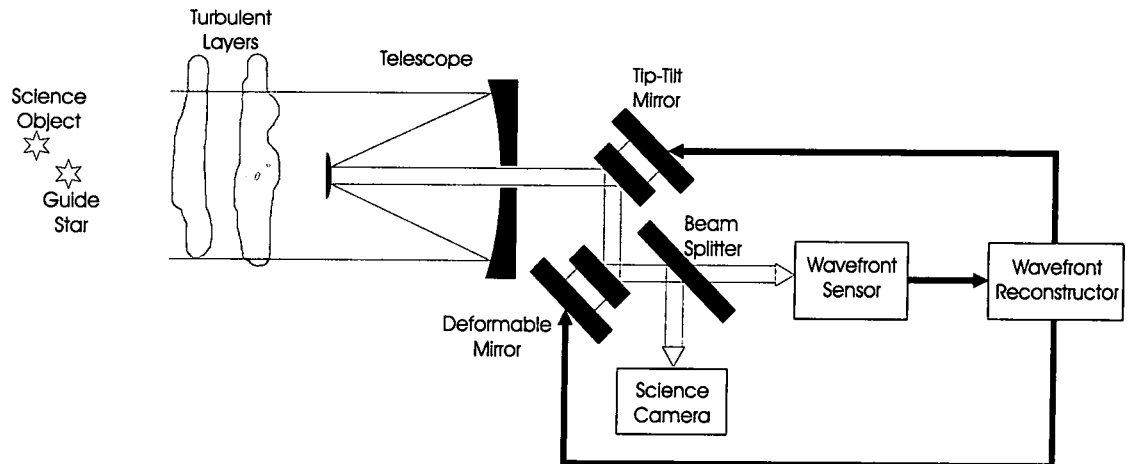
Figure 2.1: A generic astronomical adaptive optics system

The tip-tilt mirror is generally present, but may be ommitted. See text for an explanation of why the tip-tilt correction is usually done by a separate mirror. The beam splitter may be an intensity splitter or a dichroic mirror. Adapted from Hardy (1998)

Conventionally, this is then reflected from a seperate tip-tilt mirror onto a deformable mirror. After the deformable mirror, the beam is split into two parts, one of which goes to the science camera and the other to the wavefront sensor. The science camera image is the one used for the astronomical observation. The wavefront sensor measures some property of the corrected image from which the residual aberrations can be calculated by the wavefront reconstructor. This then determines the control signals appropriate for the deformable and tip-tilt mirrors to minimise the residual aberrations.

Several features are worth commenting on. Firstly, the light from the science object does not pass through exactly the same turbulence as that of the guide star, except in the special case where the science object is sufficiently bright to be used as the guide star. As the angular separation between the guide star and the science object increases, this discrepancy becomes greater, and the quality of correction of the image of the science object deteriorates. The maximum acceptable angular separation between the guide star and the science object is the isoplanatic angle, and the area of sky in which adequate correction is achieved is called the isoplanatic patch. Secondly, the utility of an AO system is limited by the number of guide stars available above the requisite brightness threshold for the system to receive enough photons for the wavefront sensor to operate. This therefore limits the sky coverage to those areas within the isoplanatic angle of a suitably

bright guide star. This has led to one of the two current main areas of development in adaptive optics: the use of laser guide stars (Foy and Labeyrie 1985). Two methods have been proposed, Rayleigh scattering from stratospheric particles, typically at an altitude of 10–20km but up to an altitude of 35km, and sodium resonant backscattering from the sodium layer at an altitude of ~90km(Quirrenbach 2000). The lower altitude Rayleigh scattering approach is simpler to implement but has a drawback in that it leaves any distortions introduced by the atmosphere above the beacon undetected, and hence uncorrected. Both the Rayleigh scattering and the sodium backscatter methods suffer from focal anisoplanatism, also called the cone effect, where the laser guide star is not at an infinite focal distance, so some parts of the atmosphere are not sensed. Obviously, since the sodium layer is 5–10 times higher than the Rayleigh scattering layer, this is more of a problem for the Rayleigh scattering approach. The Rayleigh scattering plume from the laser beacon exciting the sodium layer is brighter than the sodium spot, however the extended plume is not suitable for wavefront sensing (Max 2000). A final drawback for both laser guide star methods is that a natural guide star is still required for tip and tilt measurements, since the laser light experiences equal and opposite overall tip and tilt upon the upward path and the return beam. This guide star can be fainter than for full turbulence correction, so laser guide stars relax the sky coverage constraints for AO systems, rather than remove them completely.

The other major current development for AO is the concept of multi-conjugate adaptive optics (MCAO). In this scheme, the isoplanatic patch size is greatly increased by using multiple deformable mirrors and wavefront sensors, with each deformable mirror conjugate to a different turbulent layer within the atmosphere (Rigaut, Ellerbroek and Flicker 2000). Aside from the inherent complexity of the multiple systems involved, the other major drawback for MCAO is the necessity to have multiple guide stars in order to achieve a three dimensional measurement of the atmospheric turbulence. Due to this, MCAO development is closely tied to the development of laser guide stars.

The final comment about the generic AO system is that the tip-tilt correction and the higher order correction are conventionally done by different devices. This is due to the fact that tip-tilt is the largest component of atmospheric turbulence, and it is difficult to construct a suitable wavefront corrector with the large dynamic range required to correct for tip and tilt, yet still have sufficient dynamic range left over to correct for the higher order aberrations. In a novel twist on this idea, the Canada-France-Hawaii Telescope mounted a deformable mirror directly onto a tip-tilt stage (Roddier 1999). Although

this method is elegant, it does not alter the control loop required to separately drive the deformable mirror and the tip-tilt corrector.

2.1.1   History of Adaptive Optics

Babcock (1953) was the first to propose the concept of adaptive optics. Technological advances yielded the first working astronomical system, "COME-ON", in 1989 (Rousset, Fontanella, Kern, Gigan and Rigaut 1990). Interestingly, multi-conjugate adaptive optics was proposed before adaptive optics systems had been built (Dicke 1975). Susbequently, AO has grown to become essentially a standard component of large telescopes (greater than 5m diameter), as well as being common on smaller telescopes. A summary of operational astronomical AO systems is presented in Table 2.1. Rigaut (1996) reviews the AO systems on medium diameter telescopes, in more depth than is presented here; a survey of equivalent depth is not available for larger telescopes. Two of these medium-telescope projects are worth a particular mention: NAOMI on the WHT which uses a segmented mirror for the wavefront correction, which is unusual in functioning astronomical AO systems and ALFA, on the Calar-Alto telescope in Spain which was the first astronomical AO system with a laser guide-star (Benn 2001, Benn, Longmore, Myers, Gregory and Davenhall 2001, Hippler, Kasper, Feldt, Weiss, Looze, Montoya, Aceituno, Ott and Davies 2000).

Some of the larger telescopes also have systems worth commenting on. The MMT has a scheme where the telescopes secondary mirror is the wavefront corrector (Lloyd-Hart, Wildi, Martin, McGuire, Kenworthy, Johnson, Fitz-Patrick, Angeli, Miller and Angel 2000), a proposal that is also being considered by Lund University for one of the deformable mirrors in their proposed 50m telescope (Andersen, Owner-Petersen and Gontcharov 2001). The Gemini telescopes have short-term plans to implement proven technologies, before trying to push the envelope of AO with second generation projects. Currently, Gemini-North uses Hokupa'a, while development continues on the facility laser guide star AO system, Altair (Graves, Northcott, Roddier, Roddier, Potter, O'Connor, Rigaut and Chun 2000, Roberts, Fitzsimmons, Szeto, Anthony, Siddall, Gaunt, Shott, Sebesta, Taylor and Duncan 2000). A duplicate Hokupa'a system will be utilised at Gemini-South, until the MCAO program bears fruition (Rigaut et al. 2000).

An interesting trend in astronomical instrumentation is that some instruments are now being designed to incorporate embedded AO systems. Examples of this trend include NICI, a near-infrared coronagraphic imager for Gemini (Trueblood 1999), the Mount

Wilson Adaptive Optics Coronagraph (Gao, Ftaclas, Shelton and Turner 2000), and the GI2T interferometer (Hamdani 2001).

System	Telescope Diameter (m)	Wavefront Corrector	Wavefront Sensor	Closed Loop Bandwidth (Hz)
USAF Starfire Optical Range	3.5	941 Actuators DM (Xinetics)	700 subaperture Shack-Hartmann	80
Canada-France-Hawaii Telescope: Hokupa'a	3.6	36 Channel Bimorph (CILAS)	36 Channel Curvature Sensor	120
ESO 3.6m Telescope: ADONIS	3.6	52 Actuator DM (CILAS)	32 Subaperture Shack-Hartmann	33Hz
Calar Alto: ALFA	3.5	97 Actuator DM (Xinetics)	100 subaperture Shack-Hartmann, with Laser Guide Star	15 Modes from 20 subapertures @ 900Hz
Lick Observatory/Lawrence Livermore National Laboratory	3m	127 Actuators, 61 active (LLNL)	37 subaperture Shack-Hartmann, with Laser Guide Star	30Hz
Mt. Palomar	5	349 Actuator DM (Xinetics)	241 subaperture Shack-Hartmann	

System	Telescope Diameter (m)	Wavefront Corrector	Wavefront Sensor	Closed Loop Bandwidth (Hz)
Mt. Wilson: University of Illinois Seeing Improvement System (UnISIS)	2.5	177 Actuator DM (Xinetics)	Shack-Hartmann with Laser Guide Star	
Monolithic Mirror Telescope (MMT)	6.5	300 actuator deformable secondary mirror (Thermotrex)	Shack-Hartmann with Laser Guide Star	
National Solar Observatory	0.76	97 Actuator DM (Xinetics)	Correlating Shack-Hartmann (modified SH, uses arbitrary scenes, like solar granulation, for wavefront sensing)	
W. M. Keck I & II	10	349 Actuator DM (Xinetics)	128×128 subaperture Shack-Hartmann with Laser Guide Star	
Apache Point Observatory: Chicago Adaptive Optics System	3.5	201 Actuator DM (University of Chicago)	15×15 subaperture Shack-Hartmann	

System	Telescope Diameter (m)	Wavefront Corrector	Wavefront Sensor	Closed Loop Bandwidth (Hz)
Gemini-North: Hokupa'a (To be replaced by Altair)	8.1	36 element Bimorph (CILAS)	36 Channel Curvature Sensor	
Subaru	8.3	185 element Bimorph (CILAS)	144 element Curvature Sensor (can be de-tuned to 36 elements for faint guide stars)	
William Herschel Telescope: NAOMI	4.2	76 element Segmented mirror (tip-tilt control for each segment, yielding 228 degrees of freedom, Thermotrex)	8×8 subaperture Shack-Hartmann (can be de-tuned to 4×4 for faint guide stars)	
Yunnan Observatory	1.2	7×7 actuator DM (Institute of Optics and Electronics, Chengdu)	Shack-Hartmann with Laser Guide Star	50Hz
Beijing Observatory	2.16	21 Actuator DM (Institute of Optics and Electronics, Chengdu)	32 Subaperture Shearing Interferometer	25

System	Telescope Diameter (m)	Wavefront Corrector	Wavefront Sensor	Closed Loop Bandwidth (Hz)
Anglo-Australian Telescope	3.9	Tip-Tilt Mirror (19 element Bimorph awaiting deployment)	Avalanche Photodiode Quad Cell (19 element Curvature Sensor awaiting deployment)	100Hz

Table 2.1: Summary of operational astronomical (including Solar Astronomy) AO systems. DM denotes continuous facesheet deformable mirror, with discrete Piezo-electric actuators. For more information on wavefront correctors, see Section 2.1.2.3, and for wavefront sensors see Section 2.1.2.1. Where a manufacturer for a wavefront corrector has been quoted, the name is appended to the description of the device. For all other cases, either the wavefront corrector was made in-house, or no information was given about the origin of the device. Where closed-loop bandwidth frequencies have not been quoted, no data was available. Data updated from Tyson (2000).

2.1.2 Constituent parts of an AO System

A theoretical AO system, as explored above in Section 2.1, consists of three sections, a wavefront sensor (WFS), a control loop and a wavefront corrector (WFC). The role of the WFS is to measure the deviations in the incoming wavefront. The signal from the WFS in then interpreted by the control loop, which drives the wavefront corrector. Conventionally, the wavefront sensor measures the beam after wavefront correction. The reasons for this are that the deformations tend to be smaller, hence the sensor does not need as large a dynamic range. Secondly, any error in the wavefront correction will be measured by the WFS, and subsequently corrected.

2.1.2.1 Wavefront Sensors

The purpose of the wavefront sensor is to measure the phase errors in the incoming beam. Historically, three types of wavefront sensor have been used for astronomy, the lateral shearing interferomer, Shack Hartmann-sensor and the curvature sensor, although there are a large number of alternative techniques. Here, the three main wavefront sensors will be discussed, along with a brief summary of some of the alternatives.

The lateral shearing interferometer was the first wavefront sensor to gain widespread acceptance for adaptive optics, and remains the most commonly used interferometer in non-astronomical AO (Hardy, Lefebvre and Koliopoulos 1977, Greenwood and Primmerman 1992, Sandler, Cuellar, Lefebvre, Barrett, Arnold, Johnson, Rego, Smith, Taylor and Spiv 1994, Roddier 1999). The principle is illustrated in Figure 2.2.
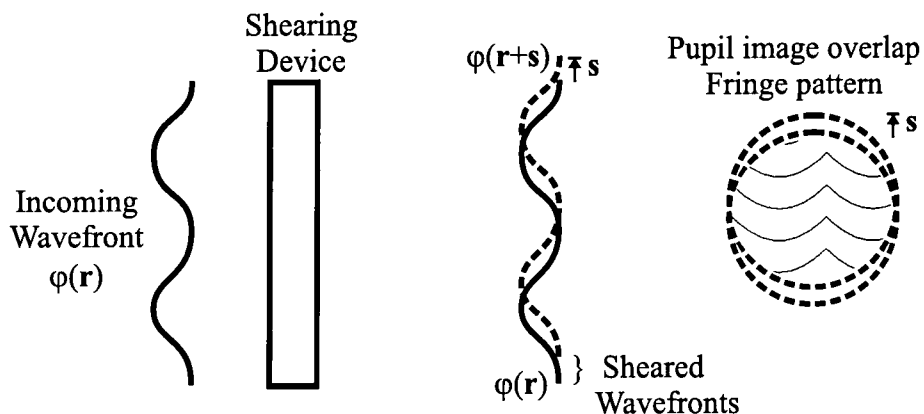
Figure 2.2: Principle of operation of a Lateral Shearing Interferometer
From Roddier (1999).

A shearing device splits the incoming beam into two components and shifts one of

them, by a shear of distance **s**. The beams then interfere in their area of overlap. This interference pattern gives a measurement of the local wavefront slope.

This technique is not common in astronomical AO systems now, since it suffers from several drawbacks. Firstly, two channels are required (one for x-slope measurements, and one for y-slopes), reducing the efficiency of the device and hence the interferometer requires more light which could be used for the science camera, and also reduces the sky coverage if a natural guide star is used. Secondly, being interferometric, it is best suited to monochromatic light; if white light is used, the fringe contrast is reduced. Finally, it tends to have complex hardware requirements, making implementation and maintenance more difficult than for the available alternatives.

The second common wavefront sensor for AO, and the most common for astronomical AO, is the Shack-Hartmann wavefront sensor (Roddier 1999). The most significant advantage over the lateral shearing interferometer is that the Shack-Hartmann sensor can be used with white light. The principle of operation is shown in Figure 2.3.
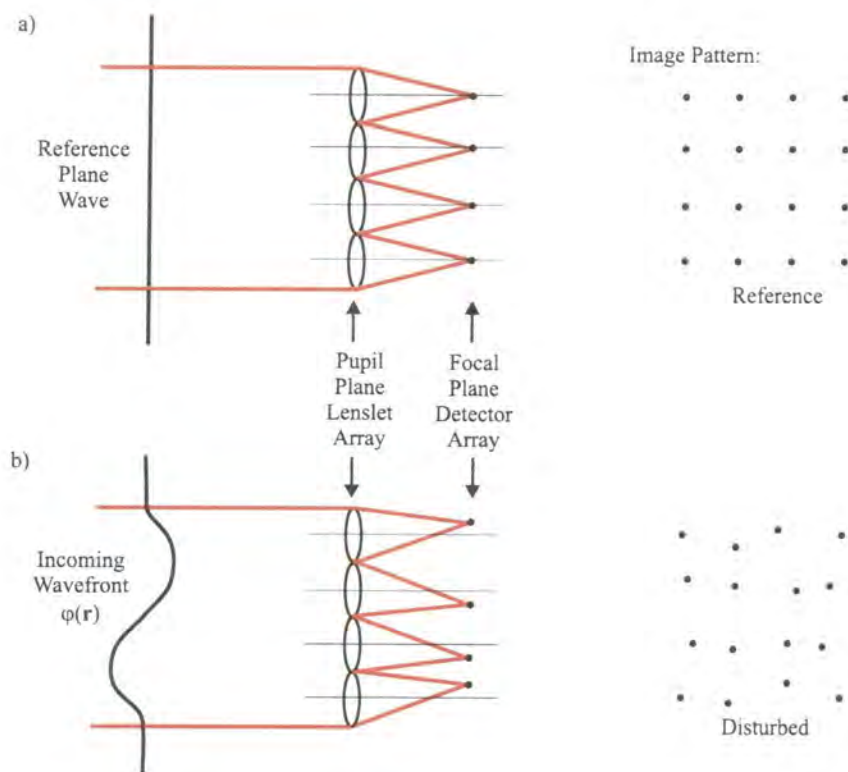
Figure 2.3: Principle of operation of a Shack-Hartmann wavefront sensor Case (a) for a plane wave, (b) for a disturbed wave. From Roddier (1999).

A lenslet array is placed in a conjugate pupil plane. If the incoming wavefront is plane, then each lenslet forms an on-axis image. However, when the wavefront is not plane, the

focused spot from each sub-aperture is displaced. The displacement of this spot is a direct measurement of the local slope in the wavefront sampled by the subaperture. Generally, either a quadrant cell photodetector is used for each lenslet (Schmutz, Bowker, Feinleib, Landon and Tubbs 1980) or a CCD array is used for all of the lenslet spots (Doel, Dunlop, Buscher, Myers, Sharples and Major 2000).

The Shack-Hartmann Wavefront Sensor has many properties that are useful to astronomical AO. These include that it can be applied to extended sources, even up to solar imaging (Rimmele, Radick, Richards and Dunn 1999). Another benefit is the simplicity of the Shack-Hartmann Wavefront Sensor, both in concept and in implementation. The main disadvantage of Shack-Hartmann sensors is that they are blind to certain modes. For example, if the subapertures are arranged in the Fried geometry[3], 'Waffle modes', where the adjacent lenslet spots are alternately out of phase, forming a chess board type pattern, are not detectable, hence this mode must be trapped by the control loop. In general, though, there are no other disadvantages to using a Shack-Hartmann Wavefront Sensor. However, in certain specific cases, as will be seen, a curvature sensor may be more appropriate.

Curvature sensing is a more recent development (Roddier 1988), and fundamentally differs from the Shack-Hartmann sensor and the Lateral Shearing Interferometer in that it measures the Laplacian of the wavefront, rather than the slope. The principle is illustrated in Figure 2.4. In practice, it is conventional to use a single detector array and a vibrating membrane in the optical path to change the focal length of the system, moving the focal plane alternately in front of and behind the detector. Other solutions can potentially be used, such as using a beam splitter and two cameras.

It can be shown that, in the geometrical optics approximation the difference between the two plane irradiance distributions (P_1 and P_2) is a measurement of the local wavefront curvature inside the beam, and of the radial first derivative at the edge of the beam (Roddier 1987). It is then possible to reconstruct the wavefront , by solving the Poisson equation. However, the key advantage of the Curvature Sensor over the Shack-Hartmann sensor is that a membrane or bimorph mirror can be used, in principle, to directly solve the differential equations, due to their mechanical nature (see Section 2.3), hence removing all matrix multiplication from the feedback loop. For this reason, should a membrane or bimorph mirror be used for an AO system, then it is more appropriate to

---

[3]In the Fried geometry, each subaperture is aligned to be at the center of the quare defined by four actuators.
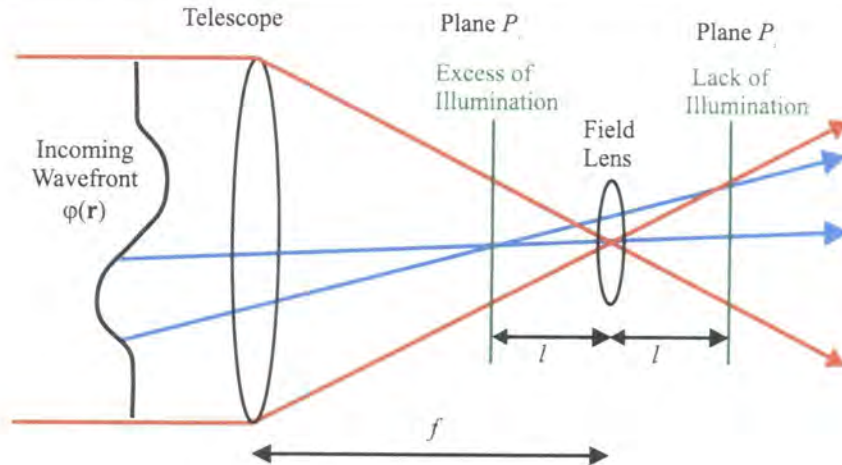
Figure 2.4: Principle of operation of a Curvature sensor

The field lens is required to re-image the pupil plane for symetry. An example section of
the incident wave is traced out with blue lines, giving an excess illumination in detector
plane P_1 and a defecit of illumination in P_2. Adapted from Roddier (1988).

use a curvature sensor system than a Shack-Hartmann sensor system. The curvature sen-
sor is also achromatic and suitable for use with extended sources. One interesting feature
is that it is possible to adjust the sensitivity, by changing the distance l in Figure 2.4,
where a smaller l implies a greater sensitivity but a lesser dynamic range (Roddier 1995).
This means that, before the loop is closed, a large l can be used, due to large wavefront
disturbances. After the loop is closed, however, the distance l can be reduced since the
magnitude of the residual disturbances should be small, increasing the sensitivity of the
sensor. The principal drawback for curvature sensors is that they have not yet been widely
deployed, so experience in their assembly is more scarce than for a Shack-Hartmann sys-
tem. For wavefront correctors where it is necessary to reconstruct the wavefront, in other
words, non-membrane or bimorph correctors, the wavefront reconstruction is also more
complex than for a Shack-Hartmann sensor.

There are alternative wavefront sensors and a brief summary will be presented here,
along with reasons why they are less common for astronomical AO. Firstly, the Gerchberg-
Saxton iterative algorithm is an elegant solution to wavefront sensing, in that it requires
no additional optics (Gonsalves 1976). The phase disturbance is determined by a process
of iterative Fourier and inverse Fourier transforms of the intensity distribution. However,
it is extremely computationally intensive. The Phase Diversity technique (Paxman and
Fienup 1988, Paxman, Schulz and Fienup 1992) is another focal plane technique, but is

not dissimilar to the curvature sensor. However, unlike curvature sensing, it requires the use of a narrow spectral band, and the computing burden is substantial (Kendrick, Acton and Duncan 1994). The pyramid sensor is another pupil plane technique, with a variable sensitivity similar to that of the curvature sensor (Ragazzoni 1996, Ragazzoni, Ghedina, Baruffolo, Marchetti, Farinato, Niero, Crimi and Ghigo 2000). The principle drawback of the pyramid sensor is that it has yet to be widely implemented in real AO systems.

Several interferometric techniques can be used for AO. These include the Smartt point-diffraction interferometer (Underwood, Wyant and Koliopoulos 1983), where the reference is generated from a spatially filtered part of the object beam. This approach has two main disadvantages for astronomical AO; it requires large spatial coherence in the incoming beam, and the intensities of the two interfering beams are not equal, which limits the sensitivity of the method. Similar to the lateral shearing interferometer are the rotational shearing interferometer (Willard 1993), and the radial shearing interferometer (Hariharan 1988). The lateral shearing interferometer has tended to be preferred, due to simplicity, but variations on the rotational shearing interferometer are being considered for the detection of extrasolar planets (Strojnik and Paez 1999). Angel (1994) also proposes the use of a Mach-Zender interferometer wavefront sensor for the same application.

A summary of commercially available off-the-shelf wavefront sensors can be found in Collings (1999).

2.1.2.2   Control Loop

The control loop is the vital part of an AO system that converts the measured wavefront sensor signal into the appropriate signals to drive the wavefront corrector. The goal of the control loop is to minimise the residual phase distortions on the wavefront detected by the wavefront sensor. The discussion here will be limited to the general principles of an AO control loop. These general principles are independent of the type of wavefront sensor or wavefront corrector used, these only become significant in the detail of a specific control loop.

With reference to Figure 2.1, it should be noted that the loop is a feedback loop, where the sensor is measuring the wavefront after correction by the wavefront corrector. There are three reasons for doing this. Firstly, the deviations from a plane wavefront should be minimised. Secondly, imperfections in the wavefront corrector, such as hysteresis or non-linear response, are measured by the sensor and should be corrected upon subsequent
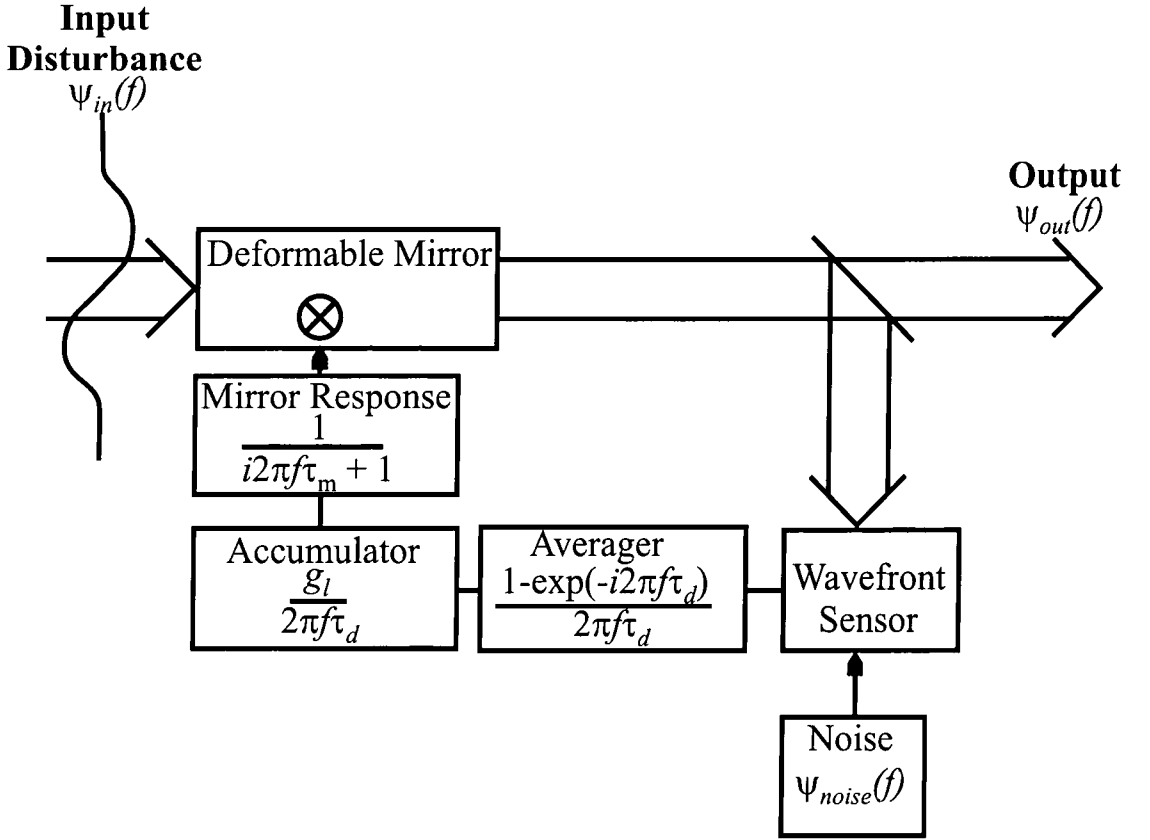
Figure 2.5: Servo model of an AO loop

The error signal at the wavefront sensor is averaged for a period of τ_d. The accumulator drives the wavefront corrector with an impulse drive signal at the end of each integration interval, which is held until the next iteration. From Tyson (2000).

iterations. Finally, the non-common path of the wavefront sensing and science beams are minimised. Hence the distortions measured by the sensor are most likely to be the same as those present at the science camera.

The control loop for an AO system can be represented as in Figure 2.5. φ_{tur} represents the uncompensated wavefront, where $\varphi_{tur}(x, y, t)$ denotes the phase at position (x, y) and time t.

The correction applied to the wavefront is denoted by $\varphi_{corr}(x, y, t)$, yielding a resultant wavefront of $\varphi_{res}(x, y, t)$ from equation 2.1.

$$\varphi_{res}(x, y, t) = \varphi_{tur}(x, y, t) - \varphi_{corr}(x, y, t) \tag{2.1}$$

In the following discussion, $|P\rangle$ represents the m-dimensional vector of the wavefront

measurements of φ_{res}, where m is the number of wavefront measurements. The signal sent to the wavefront corrector is represented by $|V\rangle$, a vector of n-dimensions where n is the number of actuators in the wavefront corrector. Throughout, $|\ \rangle$ will be used to represent a column vector, and $\langle\ |$ a row vector. Also, italicised capitals, such as P, represent matrices.

The determination of the control matrix, D^*, in a closed loop AO system assumes that the AO system is linear. This is generally a valid assumption, since the values of $|P\rangle$ are typically small in closed loop, and wavefront correctors usually have large linear regimes. The behaviour of the AO loop system can be fully described by knowledge of the optical interaction matrix, D (Boyer and Gaffard 1991). This $m \times n$ matrix defines the sensitivity of the the wavefront sensor to the wavefront corrector deformations. The nth column corresponds to the response of the wavefront sensor to a unit voltage applied to the nth actuator, so is a representation of the influence function of the wavefront corrector (see Section 2.1.2.3). The behaviour of the AO system can be described by equation 2.2:

$$|P\rangle = D|V\rangle \qquad (2.2)$$

To create an AO system, it is necessary to determine what actuator signals should be sent for a given detected wavefront, in other words the inverse of equation 2.2, as shown in equation 2.3. :

$$|V\rangle = D^{-1}|P\rangle \qquad (2.3)$$

Hence, it is necessary to determine the matrix D^*. In general matrix D is rectangular, since $n \neq m$. Therefore, a criterion must be defined to compute the pseudo-inverse control matrix, D^*. A common choice for this criterion is that, for a given measurement vector $|P\rangle$, D^* must lead to a control vector $|V\rangle$ minimizing the norm[4] of the the residual measurement vector. The best estimate of $|V\rangle$ is therefore:

---

[4]Where the norm is defined as:

$$\||A\rangle\|^2 = \langle A||A\rangle = \sum_{i=1}^{m} A_i^2$$

$$|V_{best}\rangle = D^*|P\rangle \tag{2.4}$$

and the residual measurement vector is given by:

$$|\varepsilon\rangle = D(|V\rangle - |V_{best}\rangle) = (I - DD^*)|P\rangle \tag{2.5}$$

where I is the identity matrix. The minimization of $\||\varepsilon\rangle\|^2$ with respect to the co-efficients of the control matrix gives a set of linear equations, from which the following solution is obtained (Roddier 1999)

$$D^* = (D^t D)^{-1} D^t \tag{2.6}$$

where ^{t} is the transposition operator. This shows that the control matrix to minimize $\||\varepsilon\rangle\|^2$ only exists if the square matrix $D^t D$ is invertible. This matrix, $D^t D$ characterises the coupling between the wavefront corrector actuators and the wavefront sensor measurements. The diagonalisation of this matrix provides a set of independent modes in the wavefront sensor space, which define an orthonormalised basis for the vector space of the wavefront corrector actuators. Each mode represents a particular shape of the wavefront corrector. There are alternative methods to generate the pseudo-inverse control matrix, D^*; for example, using a singular value decomposition of the matrix D.

This description is for a generalised modal control loop. Where a zonal wavefront corrector is used (see Section 2.1.2.3), it is possible to use a simpler zonal control loop, which is a subset of the modal control system. There are two major advantages to persisting with the full, generalised modal control, however. Firstly, there is the possibility of filtering out modes that are sensitive to measurement noise. In other words, those modes for which the wavefront sensor is less sensitive, can be given less weight than those modes for which the wavefront sensor is most sensitive. Indeed, those modes to which a given wavefront sensor is blind can be ignored completely (for example, piston mode is not detectable by any non-interferometric wavefront sensor).

The second advantage is that it becomes possible to use multiple wavefront correctors within one system, with each corrector dedicated to the correction of certain modes. This is most commonly used to remove tip-tilt correction from the main adaptive optical

element and instead have a dedicated tip-tilt correction mirror, as shown in Figure 2.1. In this scheme, the tip-tilt modes are used to drive the tip-tilt mirror, while the correction of the higher order modes is performed by the deformable mirror. In the case of Dayton, Restaino, Gonglewski, Gallegos, McDermott, Browne, Rogers, Vaidyanathan and Shilko (2000) and the Canada-France-Hawaii Telescope (Roddier 1999), the deformable mirror used was itself mounted onto a tip-tilt stage, resulting in one less reflection in the optical system.

The preceding discussion has also omitted temporal considerations. This will be explored through the use of a servo model, illustrated in Figure 2.5

The input wavefront is modulated by the wavefront corrector, and a fraction of the output is sensed by the wavefront sensor. In addition to measuring the residual phase error in the wavefront, the sensor also generates a noise component. The output from the wavefront sensor is averaged over an integration time τ_d. The averaged wavefront sensor signal is the input into an accumulator, which has an adjustable gain parameter, g_l, used to vary the loop bandwidth. The wavefront corrector response is modeled as having an exponential time constant, τ_{wfc}.

The overall performance of the system can be characterised by the ability of the system to simultaneously suppress both the turbulence-induced and wavefront sensor noise-induced wavefront distortions. The properties of the individual components of the AO control loop can best be expressed by the frequency domain transfer functions, as illustrated in Figure 2.5, which can then be applied to the power spectrum of the turbulent atmosphere. The transfer function from the wavefront corrector is given by:

$$T_t(f) = \left| \frac{1}{1 + H_{av}(f)H_{acc}(f)H_{wfc}(f)} \right|^2 \tag{2.7}$$

while that for the noise is:

$$T_n(f) = \left| \frac{H_{av}(f)H_{acc}(f)H_{wfc}(f)}{1 + H_{av}(f)H_{acc}(f)H_{wfc}(f)} \right|^2 \tag{2.8}$$

where, in both cases, H_{av}, H_{acc} and H_{wfc} correspond to the averager, accumulator and wavefront corrector transfer functions, respectively.

Taking the power spectrum of the turbulence figure (the distorted wavefront omitting tip-tilt), F_{fig}, from Greenwood and Fried (1976), to be:

$$F_{fig}(f) = \begin{cases} 0.132\sec(\zeta)k^2D^4\mu_0^{12/5}\nu_{5/3}^{-7/5}f^{4/3}, & f \le 0.705D^{-1}\mu_0^{-3/5}\mu_{5/3}^{3/5} \\ 0.0326\sec(\zeta)k^2\nu_{5/3}f^{-8/3}, & f \ge 0.705D^{-1}\mu_0^{-3/5}\mu_{5/3}^{3/5} \end{cases} \qquad (2.9)$$

where the terms are defined in Table 2.2.

Term	Definition
ζ	Zenith angle
k	Optical wavenumber ($k = 2\pi/\lambda$)
D	Telescope Diameter
μ_0	Zeroth-order turbulence moment of the atmosphere
$\nu_{5/3}$	5/3 order velocity moment of the atmosphere

Table 2.2: Definitions of terms in Equation 2.9.

A similar expression for the effect of tip and tilt can be found in Tyler (1994). The power spectrum of the residual error is then the sum of the turbulence and noise outputs:

$$F_{error}(f) = T_t(f)F_{fig}(f) + T_n(f)F_{noise}(f) \qquad (2.10)$$

A similar expression is found for the power spectrum of the residual error in the tip-tilt correction loop, using the appropriate tip-tilt corrector parameters in place of the wavefront corrector parameters, and using the expression for the tip-tilt power spectrum from Tyler (1994) in place of equation 2.8.

Only two parameters may be tuned within an existing AO system, the integration time and the loop gain. A shorter integration time, and therefore a higher bandwidth, reduces the number of photons collected each cycle, and hence decreases the wavefront sensor signal to noise ratio. A higher loop gain improves the rejection of low-frequency turbulence. However, the loop gain can not be arbitrarily large, since the high frequency components are amplified, and an instability results.

The other system parameters, such as the wavefront corrector response, are a consequence of the initial system design. Care must be taken to ensure that the AO system is well-suited to the eventual location where it will be deployed. Hence, it is common for the atmospheric profile at telescope sites where AO systems will be deployed to be studied in detail; examples include (Masciadri and Garfias 2001, Giovanelli, Darling, Sarazin, Yu,

Harvey, Henderson, Hoffman, Keller, Barry, Cordes, Eikenberry, Gull, Harrington, Smith, Stacey and Swain 2001a, Giovanelli, Darling, Sarazin, Yu, Harvey, Henderson, Hoffman, Keller, Barry, Cordes, Eikenberry, Gull, Harrington, Smith, Stacey and Swain 2001b, Hidas, Burton, Chamberlain and Storey 2000).

2.1.2.3   Wavefront Correctors

The wavefront corrector is the component of the AO system that modifies the original beam to provide real time compensation for the phase errors in the wavefront. Many devices exist to perform this compensation, a review can be found in Roddier (1999), with less theoretical summaries in Collings (1999) and Tyson (2000). A brief overview of commercially available wavefront correctors will be presented here, along with some comments about general wavefront corrector characteristics, and desired characteristics in a wavefront corrector for cryogenic operation. The discussion will then proceed to consider the Micro-Machined Membrane Deformable Mirror (MMDM) from OKO Technologies [5] in more detail, as that is the wavefront corrector chosen for this project.

A summary of commercially available wavefront correctors is presented in Table 2.3, a subset from Collings (1999), where the values are taken from published literature (Lee, Cowan, Welsh, Bright and Roggemann 1998, Burns, Ionescu, Geneczko, Grasso and Davidson 1997, Love 1997, Oppenheimer, Palmer, Dekany and Sivaramakrishnan 1997, Bifano, Krishnamoorthy Mali, Dorton, Perreault, Vandelli, Horenstein and Castanon 1997, Vdovin 1998).

---

[5]OKO Technologies have recently been renamed as Flexible Optical BV.

Company	Type	N	d(μm)	Layout	Speed (Hz)	Stroke (μm)	Advantage
ThermoTrex	SM	76	10000	Square	5000	0.3	Modular
Wright AFB	DM	128	203	Square		0.3	MEMS
Northrop-Grumman	DM	1024	1000	Square		1	MEMS
Meadowlark	LCD	69	2000	Hexagonal	26	0.633	Low Voltage
Xinetics	DM	349	7000	Square	100	4	Tested
Boston University	DM	9	250	Square	66000	0.4	MEMS
OKO Technologies	DM	37	1750	Hexagonal	500	9	MEMS
Cilas	BM	31	15000	Concentric	1000	15	Tested
Cilas	SAM	185	8000	Square	1000	5	Tested

Table 2.3: Summary of commercially available wavefront correctors
Legend: SM: Segmented Mirror; DM: Deformable Mirror; LCD: Liquid Crystal Device; BM: Bimorph Mirror; SAM: Stacked Actuator Mirror; N: Number of Actuators; d: center to center actuator separation; MEMS: Micro-electro-mechanical system. For original sources of information, see text. Adapted from Collings (1999)

The commercially available wavefront correctors fall into 5 types. The first of these is the segmented mirror, where the reflecting surface is broken into several small, individually actuated segments. Each segment may have piston only control, or piston, tip and tilt control. The actuators are generally piezo-electric materials, controlled by high voltages. Piezo-electric actuators suffer from a phenomenon known as hysteresis; this means that the position of the actuator for a given control signal is not repeatable. The typical material used for piezo-electric actuators, lead zirconium niobate (PZT) has hysteresis in the range of 5–20% (Tyson 2000).

These are zonal correctors, defined as each actuator only affecting the region local to that actuator. Generally, the layout has been shown to have little effect on the atmospheric correction performance for piston only zonal correctors (Loktev, De Lima Monteiro and Vdovin 2001). In the case of pure piston actuators, roughly $4N$–$8N$ actuators are required to get the same fitting error as for a continuous facesheet mirror with N actuators, but for actuators with tip and tilt correction as well as piston, the number of actuators required to get the same performance is $\frac{3N}{2}$ (Roddier 1999).

The second type is the deformable, or continuous facesheet, mirror. In this, the

reflecting surface is completely continuous, but is deformed by discrete actuators. Again, these actuators are generally, but not exclusively, piezo-electric materials. These may be zonal or modal, depending on whether the area of influence for each actuator is localised to that actuator or affects a larger area of the surface, and hence whether the control loop is modal or zonal. Each actuator in a modal corrector has an influence function, which describes how the phase change introduced by a unit control signal to that actuator varies with position across the wavefront corrector surface. It has been shown that, for correcting atmospheric turbulence, modal corrector type and actuator layout have little effect on performance (Loktev et al. 2001).

The third type is a liquid crystal device. This is unique in that it may operate in transmission, as well as reflection. They have been demonstrated to function at low frequencies (Gourlay, Love, Birch, Sharples and Purvis 1998), as well as at more practical speeds (Restaino, Baker, Dayton and Finkner 2000), however some issues remain. In particular, liquid crystal spatial light modulators (SLMs) suffer from being sensitive to polarisation of the incoming beam, and usually have a narrow bandpass, although some work has been done to address these issues (Bold, Barnes, Gourlay, Sharples and Haskell 1998).

The fourth type is the bimorph mirror, which consists of two layers of piezo-electric material bonded together, with a reflective layer applied. By applying voltages across the layers one layer can be expanded while the other is contracted. Actuators are constructed by splitting the piezo layers in appropriate positions. These are again modal devices (Cao and Yang 1997).

The final type is the stacked actuator mirror, which is similar to the conventional piezo-electric actuated deformable mirrors, although the actuators consist of multiple discrete discs, rather than a single larger disc. Whether this constitutes a genuinely distinct fifth type is not clear, although here the classification of Collings (1999) has been followed.

The number of actuators required in a correction element is proportional to $(D/r_0)^2$, where D is the telescope diameter and r_0 is Fried's parameter, defined as the distance over which the rms phase of the atmosphere is 1 rad (Roddier 1999).

The interactuator spacing is not a major issue, since the beam can usually be re-imaged to a diameter to suit the adaptive optical element being used. However, it does indirectly constrain the size of the deformable mirror.

It was established in the 1970s that the layout of the actuators is not significant for 40 actuators or more (Tyson 2000). Recent research has extended this limit down to 37

actuators (Loktev et al. 2001).

The required frequency response of a deformable mirror is defined by the Greenwood frequency (Greenwood 1977):

$$f = \frac{0.4v}{\sqrt{\lambda L}} \tag{2.11}$$

where v is the mean wind velocity in the turbulent layer, λ is the wavelength of the incident beam, and L is the average thickness of the turbulent layer. In practise, for astronomical purposes, the desired bandwidth is typically 200–400Hz, although correction at slower speeds still yields improvements to the astronomical observation.

The required stroke for a given application depends on whether a separate tip-tilt mirror is utilised. Assuming a separate tip-tilt corrector to be present, the required phase correction is the phase error introduced by the atmospheric turbulence, given by Sasiela (1994):

$$\sigma^2_{fig} = 0.134\left(\frac{D}{r_0}\right)^{5/3} \tag{2.12}$$

which corresponds to an rms phase distortion of several wavelengths for a nominal astronomical installation (Tyson 2000).

The advantages column of Table 2.3 should be considered with caution; a characteristic that may be an advantage for one application may be detrimental to an alternative application. Nevertheless, some general advantages will be mentioned here. The ThermoTrex mirror has a substantial advantage in that each segment is completely independent with no cross-talk. The Meadowlark device operates at a much lower voltage than the other forms of wavefront corrector, a big advantage as it simplifies the control electronics. The most significant advantage of the CILAS mirrors and the Xinetics mirror is that they have been deployed in many installations, and hence are a more mature technology than the other devices.

MEMS devices have several advantages over conventional wavefront correctors. Most notably, the small size means that they are simpler to deploy. The small size also alows MEMS devices to be more easily embedded into other systems, raising the prospect of embedding whole AO systems into relevant instruments. In addition, MEMs devices are dramatically cheaper than conventional devices. The OKO Technologies device also

benefits from having been deployed in many systems, including laser beam correction, ophthalmology, intracavity laser control, communications, holographic memory and optical fiber switching (Vdovin 2001d). Since MEMs are both more compact and lower cost than traditional wavefront correctors, they can be used in many more fields, which should lead to rapid development and maturation of these novel technologies.

2.2   Cryogenic Adaptive Optics

There are two major reasons why it would be advantageous to be able to cool an adaptive optics system to cryogenic temperatures. The first, and perhaps most fundamental reason, is for ground based infra-red astronomical observations. The second reason is for satellite observatories, which are frequently passively cooled. Both of these reasons would apply to a space based infra-red observatory, such as the Next Generation Space Telescope (NGST) (NASA 2001).

2.2.1   Infra-red Observations

Historically, astronomical flux measurements at optical wavelengths were separated into three pass bands, U, B and V. The development of infrared detectors with sufficient sensitivity to be used for astronomical purposes in the 1950s led to Johnson (1962) extending this scheme into infra-red astronomy, with the creation of the J, K, L and M bands, defined to fit the transmission bands through the atmosphere. These bands were originally defined as per Table 2.4.

Filter	Short wavelength edge (μm)	Long wavelength edge (μm)
J	1.1	1.4
K	1.9	2.5
L	3.2	4.1
M	4.4	5.5

Table 2.4: Original Definition of IR filters

Transmission is approximately 70% within the pass band, and 0% outside. Data from (Johnson 1962)

Over time, the definitions of these bands has gradually altered, and new bands have been added. A summary is presented in Table 2.5 (Lena, Lebrun and Mignard 1998).

Filter	$\lambda_0 (\mu m)$	$\Delta\lambda_0 \ (\mu m)$
I	0.90	0.24
J	1.25	0.30
H	1.65	0.35
K	2.20	0.40
L	3.40	0.55
M	5.0	0.3
N	10.2	5
Q	21.0	8

Table 2.5: Recent Definition of IR filters

λ_0 is the central transmitted wavelength, $\Delta\lambda_0$ is the width of the pass-band. Adapted from (Lena et al. 1998)

When these pass bands are compared with the black body emissions curve, reproduced in Figure 2.6, it can be seen that the emissions from room temperature objects becomes increasingly significant as the wavelength moves further into the infra-red. As can be seen from the Figure, by reducing the temperature of an object to 78K, it's emissions are dramatically reduced. In particular, the effect in the K-band of cooling is massive.

Infra-red telescopes are designed to minimise the amount of radiation from room temperature emissions observed by the detector. These emissions come from all the elements in the optical path to the detector. Hence, instruments such as spectrographs are frequently cooled. A cryogenically cooled AO system would therefore be advantageous for infra-red astronomy, since at least the beam splitter and wavefront corrector are in the optical path, and hence observed by the detector.

It is interesting to note that the Fried parameter, r_0, varies with $\lambda^{\frac{6}{5}}$, so adaptive optics becomes easier to implement at infra-red wavelengths than at optical wavelengths (Lena et al. 1998).

2.2.2   Satellite Observations

Satellites are frequently cooled to cryogenic temperatures for reasons of practicality. It is simpler to maintain the temperature of a satellite by cooling to the lowest temperature it encounters during an orbit than to keep it heated to the warmest temperature encountered. Cooling is either done passively, by the use of a shield to block solar radiation, or
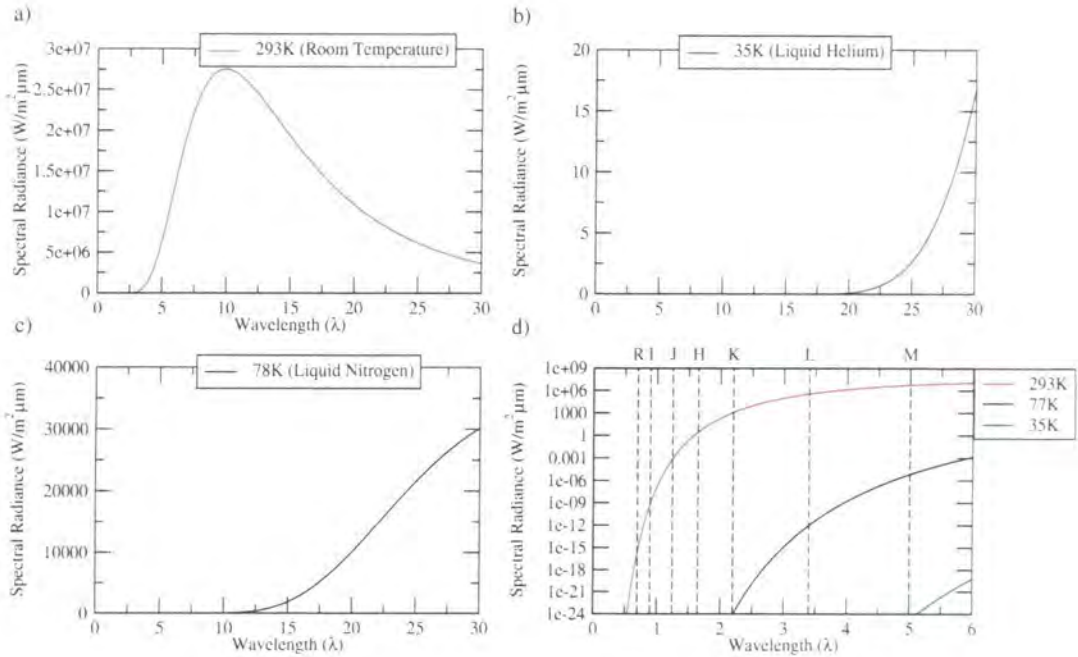
Figure 2.6: Black Body emission curves

Red line is for a temperature of 293K, Black for 78K and Blue for 35 K throughout. Graphs A, B, and C show emissions on a linear scale, each graph is indenpendently scaled. Graph D shows emissions for each case on a logarithmic scale. Letters above graph D denote standard astronomical filters, using the definitions in Table 2.5

actively, using a coolant such as liquid helium. However, since AO systems correct for atmospheric turbulence, why does a satellite observatory require an AO system?

The main driver is that, as space-based telescopes get larger, the density of the primary mirror has to be reduced in order to meet mass constraints. For example, for the 8m NGST, an areal density of less than 10 kg/m^2 is required, which is a factor of 10 less than current lightweight space telescopes (Holota et al. 1999). This will inevitably result in the telescopes being less rigid, and hence introduce optical aberrations. A detailed analysis of the potential aberrations on a space based telescope primary mirror are discussed in Holota et al. (1999). The sources of aberrations identified include manufacturing errors, gravitational release, thermal effects, mounting stresses and alignment errors (longitudinal, lateral and angular). Here, two of those will be discussed, gravitational release and thermal effects. The likely effect of constructing the mirror in the gravitational field on

the surface of the Earth before deployment in a weaker field is a radially symetric deviation in the mirror surface. This deformation will be parabolic, and hence will lead to some defocus in the final optical system.

The aberrations introduced by thermal effects will be as a consequence of variations in the coefficient of thermal expansion of the mirror and support structure. There are two components to the aberrations that this will introduce. Firstly, there will be a static component, representing the aberrations introduced by the cooling from the room temperature construction and polishing of the mirror, down to the cryogenic temperatures of the satellite's operation. Then there will be a time-varying component from variations in the satellite's temperature. The second component can be minimised; however, the first can only be circumvented by polishing the mirror at the operating temperature of the satellite. This solution would be many times more expensive than implementing some form of active optics on the satellite.

Hence, there are compelling reasons for implementing an active optics solution on a large satellite observatory. Other reasons do exist, such as the possibility of using a non-diffraction limited primary mirror and implementing active correction for cost reasons.

More ambitious space observatory proposals have also been suggested. Schemes such as that proposed by Angel, Burge, Hege, Kenworthy and Woolf (2000), which consists of the primary mirror and the secondary mirror being on separate satellites flying in formation, would certainly require some form of AO, be it active or adaptive, to correct for alignment errors.

2.2.3   Infra-red Satellite Observatories

A cryogenically cooled AO system suitable for ground-based infra-red observations and for satellite operation could, of course, be deployed in an infra-red satellite observatory. There is a further advantage to this approach, in addition to those outlined above, in that it becomes possible to conduct infra-red observations at wavelengths where the atmosphere is opaque.

2.2.4   Cryogenic Adaptive Optics requirements

Referring to Figure 2.1, it is clear that the only sections of the AO system that need to be cooled to eliminate room temperature emissions from the detector are the beamsplitter, deformable mirror and the tip-tilt mirror. The control loop is identical irrespective of the temperature of the system. The wavefront sensor may be cooled to reduce thermal noise

on the CCD detector; however, this is a consequence of meeting noise requirements and has no impact on the emissions observed by the detector.

The requirements for the wavefront corrector become more stringent at cryogenic temperatures. The general requirements for a room temperature wavefront corrector, such as frequency response and maximum stroke, still apply to the cryogenically cooled wavefront corrector. Since, for reasons that will be discussed, the performance of a wavefront corrector generally deteriorates as it is cooled, this means that either this deterioration has to be minimised, or the room temperature operation of the wavefront corrector has to be substantially superior to the minimum requirements. Here, the optimum design for a cryogenic wavefront corrector will be discussed. Section 2.4 will evaluate how well MMDMs meet these criteria.

2.2.4.1 Ideal Cryogenic Wavefront Corrector

The first design decision is to decide on the type of actuator that should be used. There are four main types of actuation for a wavefront corrector; piezo-electric stack, bimorph, liquid crystal and electrostatic. Of these, the first three are not suited for cryogenic operation. Piezo-electric stacks have dramatically reduced maximum stroke and hysteresis problems at cryogenic temperatures. Although some work has been done towards reducing these problems, Paik, Park and Shrout (1999) report that the throw of piezo-electrics specifically tuned for cryogenic operation have a maximum stroke 'significantly lower than the room temperature value'. Bimorph mirrors suffer from the same problems as piezo-electric mirrors, although they also have the additional difficulty of bonding dissimilar materials together, which leads to additional stresses on the device at cryogenic temperatures. This will be discussed more fully later in this section. Liquid crystals typically have a working temperature range down to -10°C. Beyond this, the liquid crystal material freezes. This leaves electrostatic actuation as the only actuation technology currently practical at cryogenic temperatures.

The second design choice is whether to have a continuous facesheet or a segmented mirror surface. Due to thermal contraction of the segments, it is likely that a segmented device would have segment alignment issues, as well as a reduced fill-factor. Hence a continuous face sheet mirror is preferable.

The third design choice is the size of the device. Generally, the smaller the device the better. The exception to this rule is when the actuator density is limited, in which case the size of the device is limited by needing to have sufficient surface area to fit the requisite

number of actuators into the device. However, smaller devices are simpler to install, easier and cheaper to cool, generally have lower power consumptions, and can potentially be embedded into other instruments. Therefore, for an ideal cryogenic wavefront corrector, a small device is preferable, although a minimum size wiill be determined by the actuator density and aperture required for the application.

The fourth design choice is to decide from what materials the device should be manufactured. While the specific materials are not important, homogeneity of the device is crucial. Specifically, all materials used should have coefficients of thermal expansion as similar as possible. This reduces the stresses introduced by differential thermal contraction. This is particularly significant for those areas that directly support the optical surface. Any coefficient of thermal expansion mis-match will result in undesirable static deformations of the deformable mirror surface, which will require some of the actuators stroke to correct, and hence leave less stroke available for turbulence correction. Closely related to the homogeneity is the complexity of the final design. In this regard, components that require critical alignment are a liability, since the alignment is unlikely to be maintained from room temperature to cryogenic temperatures. Since there are more applications for room temperature AO than for cryogenic temperature AO, it is reasonable to assume that wavefront correctors will generally be designed for room temperature operation, with only minor optimisations available for cryogenic operation.

The remaining design criteria, such as number of actuators, reflective coating and frequency response, are application specific, and identical to the room temperature requirements.

2.3 Micro-Machined Membrane Deformable Mirrors

Micro-machind membrane deformable mirrors (MMDMs) will be described here, before a discussion of why they are suitable for cryogenic operation in Section 2.4. The MMDMs used in this project were donated by OKO Technologies (Vdovin 2001b). MMDMs are a form of MEMS/MOEMS[6] device, developed by Vdovin and Sarro (1995) for adaptive optics. These devices are constructed as shown in Figure 2.7. The final device consists of two parts; the actuator structure and the deformable membrane. These devices have continuous facesheets and are electrostatically actuated.

The actuator structure is obtained by patterning an aluminium interconnection layer

---

[6]Microelectromechanical/Microoptoelectromechanical
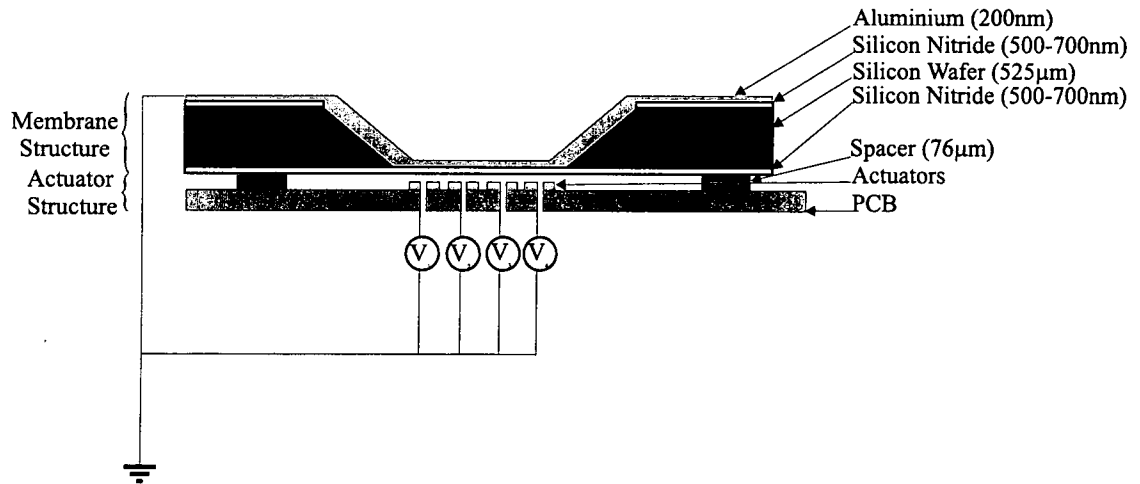
Figure 2.7: MMDM Cross-section

Cross section through an MMDM, illustrating the different materials used in the construction. The distinction between 'Membrane structure' and 'Actuator Structure' is also made. The membrane is formed by etching away the silicon wafer, with the aluminium layer subsequently being deposited over the membrane.

on the surface of a silicon wafer, insulated by a layer of silicon dioxide. The devices studied within this thesis had one of two actuator patterns, illustrated in Figure 2.8. However arbitrary actuator patterns may be produced, to a resolution of 2μm (Vdovin 1996). The actuators are connected to a conducting track on the rear of the PCB by means of metallized holes, called 'vias'. These vias are important to reduce the effect of air damping (Tyson 2000).

The membrane structure is formed by the bulk-micromachining of a silicon wafer. In this process, a silicon wafer is coated on both sides by a thin (500–700nm) layer of silicon nitride. A suitable compensation mask, described in Vdovin (1996), is then cut out of one of the nitride layers. The silicon layer is then anisotropically etched with a water/KOH solution. This solution does not etch the silicon nitride, so the result is an optically smooth silicon nitride membrane suspended by a Silicon wafer. The membrane is approximately circular, with the maximum deviation from a circular contour of 0.2mm (Vdovin 1996). The membrane is then coated with a reflective surface. In the case of the devices studied here, this surface was 200nm of Aluminium, however, other metal or dielectric coatings are available (Vdovin, Sarro and Middelhoek 1999).

The membrane structure is subsequently mounted over the actuator structure, with an air gap between the two structures of 200μm. The membrane is then electrostatically ac-
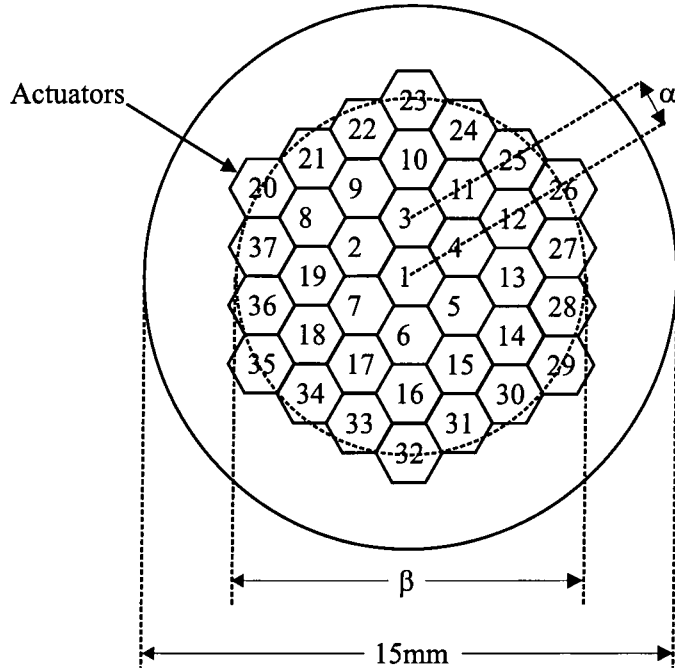
Figure 2.8: Actuator structure of the MMDMs

In the case of MMDM A, dimension α in the diagram corresponds to 1.75mm, hence β is 10.5mm. In the cases of MMDMs B and C, dimension α is 1.25mm, and β is 7.5mm

tuated by keeping the membrane at 0V, and applying voltages to the actuators. Applying the same voltage to all of the actuators causes the membrane to take a parabolic shape. The actuators can only attract the membrane; the membrane cannot be pushed away from the actuator structure. Hence, the membrane is conventionally biased to half of the maximum stroke before use. The maximum stroke of the device is 10μm at the centre of the membrane (Vdovin et al. 1999). The membrane edge is fixed, and hence no correction can be performed at the periphery of the device. Therefore, the optimum beam radius is less than the membrane diameter. Experimentally, the optimum optical pupil diameter has been determined to be about 65% of the membrane diameter (Paterson, Munro and Dainty 2000). The initial surface of the membrane is flat to within 0.5μm peak to valley over the whole surface, and to within 150nm in an rms sense (Vdovin et al. 1999).

It has been shown experimentally that a membrane model can be used for the static description of micro-machined adaptive mirrors (Vdovin 1996). Hence, the membrane deflection $S(x, y)$ can be described by the Poisson equation, given in Equation 2.13, where $P(x, y)$ is the electrostatic pressure at position (x, y), and T is the membrane tension:

$$\Delta S(x, y) = -\frac{P(x, y)}{T} \tag{2.13}$$

In the case of electrostatic actuation, $P(x, y)$ is given by Equation 2.14:

$$P = \frac{\epsilon \epsilon_0 V(x, y)^2}{d(x, y)^2} \tag{2.14}$$

where ϵ is the dielectric constant of air and ϵ_0 is the dielectric constant of free space, $V(x, y)$ is the potential distribution on the actuator structure and $d(x, y)$ is the distance between the membrane and the actuator structure. Equations 2.13 and 2.14 require a set of boundary conditions, describing the shape of the membrane contour $S_c = F(x, y)$ (Vdovin et al. 1999).

MMDMs have been successfully deployed in a test-bed AO system (Paterson et al. 2000), and in a field demonstration (Dayton et al. 2000).

2.4   Are MMDMs ideal cryogenic wavefront correctors?

Referring back to Section 2.2.4.1, we see that there are four requirements for a wavefront corrector to be suitable for cryogenic operation, in addition to those required for room temperature operation. As discussed in Section 2.3, MMDMs have been succesfully used as room temperature wavefront correctors, hence only the cryogenic requirements remain to be fulfilled. These are summarised in Table 2.6.

Condition	Property	Requirement
1	Actuation	Not piezo-electric or liquid crystal
2	Reflecting Surface	Continuous
3	Size	Smaller volume is beneficial
4	Materials	As few interfaces between materials with dissimilar coefficients of thermal expansion as possible

Table 2.6: Summary of the additional requirements for a cryogenically cooled wavefront corrector

It is clear that MMDMs satisfy conditions 1, 2 and 3. Condition 4 is slightly less clear. Figure 2.7 shows a cross section through an MMDM.

There are 4 interfaces of interest, summarised in Table 2.7.

Interface	Upper Material	Lower Material	Upper Material CTE $(10^{-6})/°C$	Lower Material CTE $(10^{-6})/°C$
1	Aluminium	Silicon Nitride (Si_3N_4)	25	0.8
2	Silicon Nitride	Silicon	0.8	2.33
3	Silicon	Silicon Nitride	2.33	0.8
4	Silicon Nitride	Spacer	0.8	Unknown

Table 2.7: Summary of interfaces between dissimilar materials in an MMDM. CTE is the coefficient of thermal expansion. All data from (Tyson 2000).

Note that interfaces below the spacer have been ignored. Any stresses introduced from beyond the spacers are considered to be part of the unknown coefficient of thermal expansion in interface 4. It should be noted that these devices are intended for room temperature operation; future devices may be optimised for cryogenic operation and hence use more homogeneous materials.

However, although there are four interfaces between dissimilar materials in the current design, there are still some fortuitous aspects that should improve the suitability of these devices for cryogenic operation. Firstly, for the optical surface to be used, there is only one interface, between Aluminium and Silicon Nitride. This means that any aberrations introduced by interfaces 2, 3 and 4 would only affect the boundary of the optical surface. Hence, by using a smaller area of the optical surface, these effects can be reduced. Secondly, although the membrane structure is supported in four corners (one corner by the membrane ground connection, the other 3 by spacers), only one of the spacers is glued to the membrane structure. Hence, the membrane structure is fixed in two positions, the membrane ground connection and the opposite spacer. This reduces the effect on the optical surface of the distortions introduced by the actuator structure.

Finally, the silicon nitride (0.5–0.7μm) and aluminium (0.2μm) layers are much shallower than the silicon wafer (525μm) (Vdovin 1996). Hence the stresses introduced by

co-efficient of thermal expansion mis-match should be minimised.

Table 2.8 summarises the suitability of MMDMs for cryogenic wavefront correction.

Condition	Property	Requirement	MMDMs meet requirement?
1	Actuation	Electrostatic	✓
2	Reflecting Surface	Continuous Membrane	✓
3	Size	Small volume	✓
4	Materials	Homogeneous	?

Table 2.8: Summary of the suitability of MMDMs as a cryogenic wavefront corrector

Alternative devices for cryogenic wavefront correction are simply not as suitable. The cryogenic suitability of the devices listed in Table 2.3 in Section 2.1.2.3 are presented in Table 2.9. With the exception of the Northrop-Grumman device, for which full details were unavailable, the only other wavefront corrector that appears to be suitable for cryogenic operation is the Boston MicroMachines device. However, the structure of this device is more complex than that of an OkoTech MMDM, so the MMDM is the most likely candidate for a cryogenic wavefront corrector.

Device	1: Actuation	2: Surface	3: Size	4: Materials
Thermotrex	X	X	X	X
Wright AFB	✓	? [a]	✓	X [b]
Northrop-Grumman	? [c]	✓	✓	? [c]
Meadowlark	X	X	✓	X^d
Xinetics	X	✓	X	X
Boston MicroMachines	✓	✓ [e]	✓	? [f]
Cilas (Bimorph)	X	✓	? [g]	X [h]
Cilas (Piezo)	X	X	X	X

[a]Although the optical surface is segmented, a lenslet array is used to increase the fill-factor. This may eliminate the problems associated with a segmented surface

[b]The mirror is a stacked polysilicon membrane, supported by complex flexures

[c]unknown

[d]Although the materials are homogeneous, they are also unsuitable for operation at cryogenic temperatures

[e]May be segmented or continuous

[f]The mirror is a stacked polysilicon membrane, supported by posts mounted upon another polysilicon membrane, in turn supported over electrodes.

[g]Marginal

[h]The reflecting surface is bonded to the two layers of piezo-electric

Table 2.9: Summary of the suitability of MMDMs as a cryogenic wavefront corrector Sources: (Collings 1999, Lee et al. 1998, Bifano, Perreault, Krishnamoorthy Mali and Horenstein 1999, Roddier 1999)

2.5 Conclusions

This chapter has summarised the development of adaptive optics systems, and analysed the constituent parts of such a system. The motives for cooling an AO system to cryogenic temperatures were then discussed. The two prinicple applications are ground-based IR observations and satellite observatories. The need for a cryogenic AO system for both these applications was discussed, along with the requirements for an ideal cryogenic wavefront corrector. It was established that cryogenically cooling an AO system did not have any implications for the wavefront sensor or the control loop. MMDMs were then discussed, and compared with the ideal cryogenic wavefront corrector. The suitability of other wavefront correctors was also examined. It was determined that MMDMs were not ideal wavefront correctors, but were the closest currently available device to the ideal wavefront corrector. The only improvement that could improve MMDMs cryogenic characteristics is to construct them from more homogeneous materials. The remainder of this thesis explores the properties of MMDMs when cooled to cryogenic temperatures (78K).

Chapter 3

Cryogenic Cooling of Micro-Machined Membrane Deformable Mirrors

3.1 Introduction

This chapter introduces the previous work undertaken on the cryogenic cooling of Micro-Machined Deformable Mirrors (MMDMs) by Bonicel (1999). The mechanical mounting method of the earlier work is then discussed and analysed, with particular emphasis placed on the efficiency of the design for the purpose of cryogenic cooling. A model is then introduced to assess the theoretical limits of this mechanical mount. From this model, it is shown that it was necessary to construct a new mounting method to achieve the targets of this thesis. A new design for the mechanical mounting is then described, having been developed through the use of the model. Experimental verification of a new method for measuring the MMDM temperature is also demonstrated. Finally, the experimental results from this new mounting are presented.

3.2 Original Mechanical Mount

Preliminary work on this project had been undertaken by Sebastian Bonicel. A brief summary of the initial system will be given here, for more detail see Bonicel (1999). The aim of the preliminary work was to characterise 19 channel MMDMs of 10mm diameter, as described in Vdovin, Middelhoek and Sarro (1997), down to 126K. The three main sections of their system, and indeed, the system described elsewhere in this thesis, were the control software, control electronics and mechanical mounting. A discussion of the

re-design of the mechanical mounting will be presented here. Changes to the control software will be discussed in sections 4.3 and 5.3 and the electronics will be discussed in section 5.2.1.

3.2.1 Mechanical Mounting
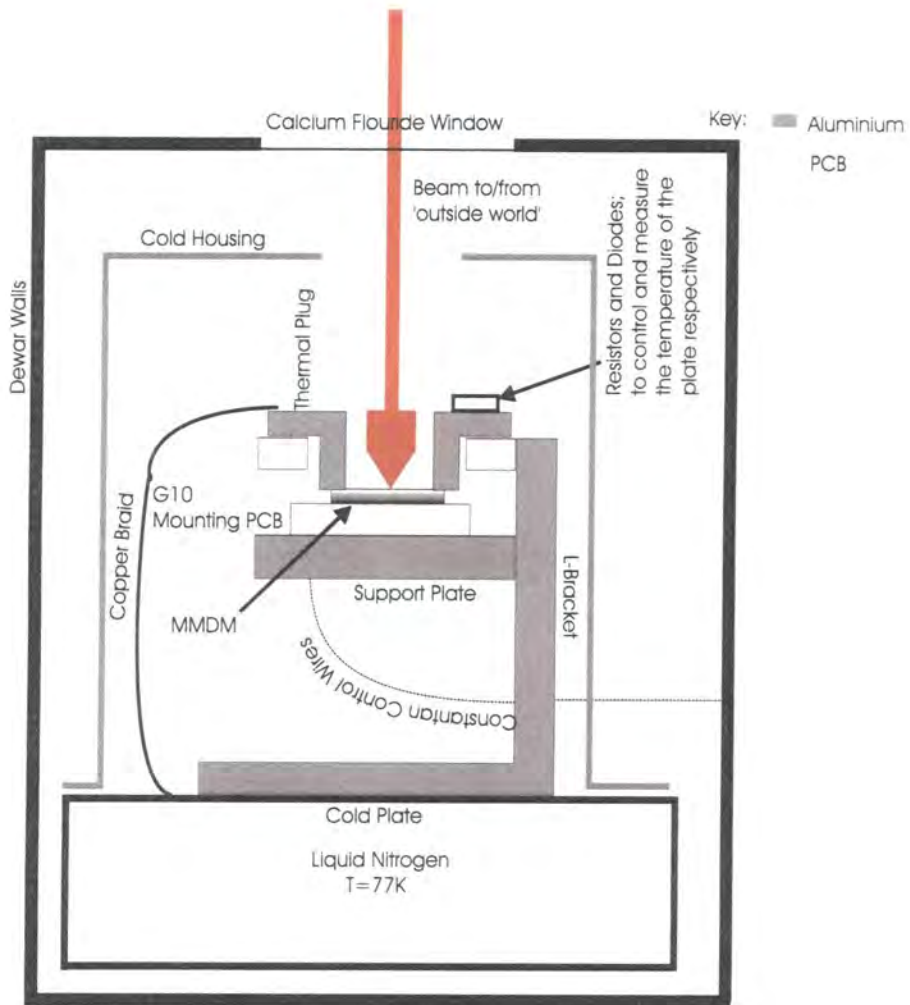
Figure 3.1: Original Micro-Machined Deformable Mirror Mechanical Mounting Dewar walls are at room temperature, and the interior of the dewar is evacuated to $\sim 10^{-4}$mbar.

The dewar was a commercial model from Oxford Instruments (Oxford Instruments 2002). The initial set-up within the dewar was designed for mounting a 19-channel MMDM. which was provided mounted on a G-10 printed circuit board with trailing leads for the control signals (see fiigure 3.1). This was supported by an aluminium support plate and L-bracket, which were in turn attached to the cold plate. However, in this arrangement,

the membrane of the MMDM is not in thermal contact with the cold plate, since the layer of G-10 is a good thermal insulator (Marquardt, Le and Radebaugh 2000). To remedy this, and facilitate a good thermal contact between the MMDM and the cold plate, an aluminium thermal plug was used, which was attached to a further G-10 support in such a way that it just made contact with the front of the membrane. This thermal plug was then attached to the cold plate using a copper braid. Also mounted on the thermal plug were a pair of diodes for temperature measurements and a pair of resistors for heating, to raise the equilibrium temperature of the MMDM to a controllable value. The wires within the system, for the MMDM control signals, the diodes and the resistors were enamelled constantan wire. Constantan was chosen due to having high electrical conductivity coupled with low thermal conductivity.

The cold housing shown in Figure 3.1 was only present for some of the tests. The purpose of this housing was to reduce the radiative emissions from the dewar walls onto the thermal plug. The reason it was only present on some of the tests was that it was necessary to evaluate whether it made any improvement to the system.

3.3   Cooling the Original System

3.3.1   Diodes as Thermometers

A fundamental problem that had been addressed prior to the start of this project, was that of how to measure the temperature of the MMDM? The solution implemented consisted of measuring the forward voltage across a diode which was mounted onto the thermal plug. Since this thermal plug was in turn in thermal contact with the mirror, the diode should be at the same temperature as the MMDM. The technique of using the variation in forward voltage across a diode as a thermometer is well established (Szmyrka-Grzebyk and Lipinski 1995). Certain caveats apply, however. Notably, since the exact composition of each diode is unique, each diode must be individually calibrated. Secondly, an error may be introduced due to the change in current flowing through the diode, depending on the exact design of the circuit used (Bresee 1999).

3.3.2   A Model for Evaluating the Thermal Properties of the Mechanical Mount

A fundamental part of this project was to successfully cool the MMDM to under 80K in order to characterise it's suitability for practical cryogenic instruments. However, using

the original system, the MMDM temperature could be routinely cooled to 126K, and occasionally cooled to as low as 115K. To assess why the MMDM was not achieving a temperature of under 80K, an audit was undertaken of the the thermal inflows and outflows to the MMDM within the dewar. Since the diode thermometers were attached to the thermal plug, it was the termal plug temperature, rather than MMDM temperature that was being measured. It was assumed that the MMDM was at the same temperature, since the plug was in thermal contact with the membrane of the MMDM.

3.3.2.1   Convective Inflows

Thermal transfer by convection can be immediately eliminated, since the dewar is typically evacuated to 10^{-4} mbar before cooling.

3.3.2.2   Conductive Inflows

The constantan wire connecting the resistors and the diodes to the external power supply and multimeter, respectively, were the potential source of conductive inflow. The power input for a given MMDM temperature can be calculated from equation 3.1, using the values from Table 3.1

$$P = kA\frac{T_H - T_C}{L} \tag{3.1}$$

Symbol	Value	Description
k	43.1W/m·K	Coefficient of thermal conduction (value from Weast (1975-1976))
A	$2.29\times10^{-9}\text{m}^2$	Area of cross-section, from diameter measured with a micrometer
T_H	293K	Temperature of "Outside World", measured with a diode thermometer
T_C		Temperature of MMDM
L	180mm	Length of constantan wires (measured)

Table 3.1: Values used to calculate power into system from conduction

3.3.2.3   Radiative Inflows

The radiative inflow was calculated from Stefan-Boltzmann's law, given in equation (3.2).

$$P = \varepsilon A \sigma T^4 \qquad (3.2)$$

Using the values from Table 3.2, a radiative power input from the outside world could be obtained. The area used for determining the radiative inflow was the that of the front and side surfaces of the thermal plug, since these were the only areas exposed to radiative emissions from room temperature sources; in the case of the side surfaces, it was assumed that the dewar walls were at room temperature (see Figure 3.1). The emissivity of the aluminium-coated membrane will be negligible, since the reflectivity is ~ 1.

Symbol	Value	Description
ε	0.5	Assumed (see text)
A	3.37×10^{-4}m	Absorbing area
σ	5.67×10^{-8}W/m^2·K^4	Stefan-Boltzmann's constant
T	293K	Room temperature

Table 3.2: Values used to calculate power into system from radiative inflow

It should be noted that the emissivity of the thermal plug, ε, was assumed to be 0.5, considered to be a reasonable upper limit value for the roughened aluminium used to construct the thermal plug.

The copper braid used to connect the MMDM to the cold plate also has a finite surface area. This area was dependent on the specific braid used (several were used for the initial tests), and varied from 4.32×10^{-4}m^2 up to 5.35×10^{-4}m^2; values which are notable for being larger than the absorbing area of the plate. Hence, the absorption of the wire was not negligible. An emissivity, ϵ, of 0.5 was also assumed for the copper. The temperature used to evaluate the power radiating onto the copper braid was the cold housing temperature, for those simulations including the cold housing, or room temperature radiation from the dewar walls otherwise.

The cold housing also had a diode thermometer attached so that the temperature of the housing was known. The contribution of the housing, when installed, to the total radiative inflow could then be calculated from the experimentally measured temperature of housing.

It is assumed that the radiative emissions from the cold plate of the dewar are negligible; an assumption which should be considered to be sound due to the T^4 term in the Stefan-Boltzmann equation.

3.3.2.4   Convective Outflows

Convection can again be ignored, for the same reason as for power inflows.

3.3.2.5   Conductive Outflows

The conductive outflow from the MMDM is given by equation 3.1. In this case k is the thermal conductivity of the copper, T_H is the MMDM temperature and T_C is the cold plate temperature, A is the cross-sectional area of the copper braid, and L is the length of the braid, with values from Table 3.3.

Symbol	Value	Description
k	401W/m·K	From (Weast 1975-1976)
A	$2.69 \times 10^{-6} \text{m}^2$	From diameter measured with a micrometer
T_H		Temperature of MMDM
T_C	77K	Temperature of Cold Plate
L	100mm	Length of copper braids (measured)

Table 3.3: Values used to calculate power out of system from conduction

3.3.2.6   Radiative Outflows

Radiative output from the thermal plug is also governed by the Stefan-Boltzmann equation (equation 3.2), although the area involved is now the entire surface area of the thermal plug. Also, the temperature involved will vary in emission, dependent on the temperature of the thermal plug rather than the atmosphere, see Table 3.4.

Symbol	Value	Description
ε	0.5	Assumed (see text)
A	$2.06 \times 10^{-3} \text{m}$	Emitting area
σ	$5.67 \times 10^{-8} \text{W/m}^2 \cdot \text{K}^4$	Stefan-Boltzmann's constant
T		Thermal Plug Temperature

Table 3.4: Values used to calculate power out of system from radiative outflow

3.3.2.7   Equilibrium

Having established the equations governing the power into and out of the thermal plug, these could then be balanced to determine the temperature of the thermal plug at equilibrium. These equations were evaluated numerically.

There were two principal reasons for solving the above equations numerically rather than analytically. Firstly, it was hoped that more insight into the cooling process could be gained by this approach. Secondly, solving the equations analytically would not be simple [1]. Therefore, a computer model was constructed to iteratively solve the equations. The model assumed a value of thermal plug temperature, and calculated the net power flow. If the net power was positive, a higher temperature was used. Similarly, if the net power was negative, a lower temperature was attempted. This process was repeated until the net power was under a pre-defined threshold value, typically 1μW.

3.3.3   Evaluation

This model provided several key insights. The first result obtained was that the temperature of the cold housing was not significant, once the housing was appreciably colder than the ambient room temperature. This was to be expected due to the T^4 term in equation 3.2. However, the reduction in the area of the thermal plug exposed to the ambient temperature was significant (the outer wall of the dewar is considered to be at room temperature). In particular, the copper braid was no longer exposed to the walls

---

[1]Attempting to solve analytically for the case without the cold housing yields

$$\epsilon A_E \sigma T_{TP}{}^4 + \left(\frac{k_1 A_{x_1}}{L_1} - \frac{k_2 A_{x_2}}{L_2}\right)T_{TP} = \frac{k_2 A_{x_2} T_{bckgd}}{L_2} - \frac{k_1 A_{x_1} T_C}{L_1} + \epsilon A_A \sigma T_{bckgd}{}^4 \qquad (3.3)$$

where the nomenclature is defined as:

Subscript:	Indicates a property of:
1	Copper braid
2	Constantan wire
x	Cross-section (all other areas are surface areas)
E	Emission
A	Absorption
TP	Thermal Plug
bckgd	Ambient temperature outside dewar
C	Cold plate temperature

This reduces to

$$X \cdot T_H{}^4 + Y \cdot T_H = Z \qquad (3.4)$$

where X, Y and Z are constants. The case including the cold housing is similar.

of the dewar, but instead to the lower temperature of the cold housing. Hence all further analysis was undertaken comparing the experiments and modelled results with the cold housing installed, since the cold housing had been demonstrated to be essential to achieving low temperatures.

The main result to emerge from the modelling was the role of radiation in the temperature of the thermal plug, and by extension, the MMDM. The calculated radiation input was 73.1mW (assuming room temperature of 293K, as measured with a diode thermometer); which is independent of the thermal plug temperature. Assuming a thermal plug temperature of 80K, and hence maximising the power into the system from thermal conduction (equation 3.1), yields a total conducted power in of just 5mW, and an absorbed power in from the copper braid of 0.5mW. This means that over 93% of the incoming power came from radiation onto the thermal plug. It was clear that this had to be reduced in order to achieve a lower MMDM temperature.

The model suggested that the thermal plug should be substantially cooler than 115K, the lowest temperature experimentally obtained with the original system; equilibrium was achieved at a temperature of 82K in the modelled system. The principal source of the power outflow was conduction through the copper braid, which was the reason for the copper braid initially being installed. There were several potential reasons for the discrepancy. Firstly, the copper wire used may have been a copper alloy, which would consequently have had a different coefficient of thermal conduction.

Secondly, a major assumption in the model is that the aluminium housing is completely opaque at infrared wavelengths. The modelled housing eliminates all radiation from the room temperature dewar walls.

Thirdly, the assumed value of the emissivity (0.5) may also have been wrong. However, this does not result in a sufficiently large change in the ultimate equilibrium temperature, resulting in a modelled equilibrium temperature of 86K, for a perfect black body with emissivity of 1.

Finally, all thermal interfaces were assumed to be perfect. The problem of the difference in temperature between two dissimilar materials in contact is non-trivial, and literature only has values for certain specific combinations. Unfortunately, the situation described here was relatively complex; there were interfaces between the copper of the cold plate and the alloy solder tag, the solder tag to the copper wire, a similar connection at the other end of the copper wire, and the final interface between this alloy solder tag and the aluminium thermal plug. To improve some of these contacts, a layer of indium

foil was inserted at the interfaces of solder tag with cold plate, and solder tag with thermal plug. As an aside, a layer of indium foil was also inserted between the thermal plug and the MMDM membrane when the MMDM was in use. Indium is a very soft metal, so the foil increases the effective surface contact area by filling in the minute ridges and valleys in the materials at either side of the boundary.

The model was most useful in directing attention towards the areas which had the largest potential improvement, notably the radiative inflow into the thermal plug.

3.4   The Motivation for a Re-design

Having established the limitations of the mechanical mounting, devloped by Bonicel (1999), attention was focused on the requirements for a re-designed mounting. The first requirement was that the new mounting had to be compatible with the 37 channel MMDM from Okotech(Vdovin 2001b). The 19-channel MMDM was supplied mounted directly onto a PCB. The 37-channel MMDM, on the other hand, was mounted onto a standard 11x11 PGA connector. This in turn mounted onto a PCB with two IDC connectors for the control voltages. This packaging method increased the vertical extent of the mirror package, and necessitated at least modification to the MMDM mechanical mounting, to prevent the front surface of the package contacting the cold housing.

The second motive for a re-design was that it was clear that some method would have to be found to reduce the radiative load onto the MMDM. This would entail the mounting of either re-imaging optics to reduce the field of view onto the MMDM, or the use of suitable filters.

A third motive was that it was desirable to remove the thermal plug from the system completely. Having calculated the power radiated from the mirror at 80K, it was known that if the radiative load onto the MMDM could be reduced to a similar level, a temperature of 80K should be acheivable without recourse to conducting heat away from the MMDM. The reason why it would be beneficial to remove the thermal plug was that it would help to preserve the fragile membrane of the MMDM. These membranes are $< 1\mu$m thick, and under high tension, so they rupture easily. Once the membrane has been punctured, the MMDM becomes useless. Therefore it was desirable to reduce the risk of damaging the membrane. In addition, there were concerns that differential thermal contraction of the indium, aluminium and slicon-nitride membrane may have introduced further aberrations upon cooling the MMDM set up.

3.5   Re-design

The model described in Section 3.3.2 was directly applicable to evaluating the validity of the re-design, and estimating how well a given design would meet the requirements outlined in Section 3.4.

The space within the dewar is limited, particularly in the vertical direction (defined as the direction from the cold plate to the dewar window). Due to this, it was decided to mount the MMDM as close to the cold plate as possible, so the aluminium L-bracket was shortened for the new design. This was purely for practical reasons, and had no direct effect on the temperature attained by the MMDM within the dewar.

It was decided to continue with the cold housing, albeit constructing a new one from copper, with a larger contact area with the cold plate. This should result in the cold housing attaining a lower temperature than for the earlier cold housing design. Although the radiative load from the cold housing was not a significant factor in the model of the original system, it was hoped to reduce other radiative inputs to such a degree that the magnitude of the emissions from the cold housing would be of a comparable level. Hence, reducing the cold housing emissions was both advantageous and achievable. There was another addition to the cold housing, in that it was coated in several layers of aluminised mylar foil. This foil is highly reflective at infra-red wavelengths and so should reduce the radiative thermal load on the MMDM further. This would make the experimental system more similar to the modelled system, in that it would ensure that the cold housing was indeed opaque at infrared wavelengths. The mylar foil itself has a low thermal conductivity, so energy absorbed by the outer layers is not conducted through to the cold housing. An aperture was cut through the foil and cold housing to allow the MMDM to be observed from outside the dewar.

The most radical change from the original design was a change in emphasis. The original design was motivated by the desire to remove power from the MMDM, by conduction. The new design was intended to prevent the radiative load reaching the MMDM in the first place. Consequently, the copper wire to the cold plate was removed, along with the thermal plug; and a filter was added over the aperture of the cold housing. This filter was a simple short pass filter (Schott classification KG4), which absorbed wavelengths above 4μm. Hence, the majority of the room temperature emissions (at 10μm, from Wien's displacement law) are blocked. The equation for the radiative power into the MMDM became

$$P = \frac{2}{3} \times A\epsilon \times \int_0^\infty \frac{2\pi c^2 h}{\lambda^5} \frac{1}{e^{\frac{hc}{\lambda k T}} - 1} \tau(\lambda) d\lambda \qquad (3.5)$$

where the factor of $\frac{2}{3}$ is from the thickness of the filter being 3mm, compared to the thickness of the filter used to produce the transmission curve being 2mm. $\tau(\lambda)$ is the transmission of the filter at a given wavelength, λ. T represents the temperature of the outside environment, in other words, room temperature. This had to be integrated numerically, by the trapezium rule, due to only having empirical data for the transmission curve (Schott Glass Technologies, Inc. 1998). The model indicated that, with the filter installed, the MMDM temperature should be essentially the same as that of the cold housing and filter. The radiative power in from the environment was cut to 8.3μW, a dramatic improvement over the 73.1mW of radiated power without the filter. It should be noted that, for a practical cryogenic AO system for infra-red astronomy, a more complex filter would be required that had a narrow band-pass in the region of interest.

Now that the thermal plug had been removed, it became necessary to find an alternative mounting point for the diode thermometers. An additional plate of almuminium, of the same front surface area as the MMDM was mounted within the dewar and the diodes epoxied to this plate. Several tests were conducted to ensure the validity of this remote temperature sensing approach, by mounting multiple plates within the re-designed cold housing and measuring the temperatures of each plate. Locations used for these tests included mounting plates alongside the MMDM socket and on an extension above the L-bracket, as well as each test having a plate mounted in the MMDM socket for reference. Even using dissimilar metals, the largest measured temperature difference for plates of the same surface area was 2$\pm$0.5K. Similarly, when the surface area was different, the largest temperature difference at equilibrium was also 2$\pm$0.5K, however the surface area was significant in the non-equilibrium temperatures, leading to temperature differences of up to 21$\pm$0.5K. Note that the possibility of attaching the diodes directly to the front surface of the silicon wafer surrounding the MMDM membrane was considered, but was deemed to be impractical. The temperature variations were independent of the location of the temperature-sensing diode within the cold housing. This meant that the entire volume within the cold housing could be considered to be at the same temperature. The final mounting point chosen for the thermal sensor plate was above the L-bracket, as this allowed the trailing wires from the diode to be permanently attached to the L-bracket, and hence prevented the risk of these wires obscuring areas of the MMDM surface.

The conducted power into the system from the constantan wire to the diodes was reduced by connecting the wires to the cold plate between the connector and the diodes. This effectively changed the conduction system from being

$$T_{diode} \longmapsto T_{bckgd}$$

to being

$$T_{diode} \longmapsto T_{coldplate} \longmapsto T_{bckgd}$$

with the power transfer in each case being governed by equation 3.1. This prevented the power coming in through the connector from being conducted to the diodes, as the cold plate was colder than the diodes. Hence the power load onto the diodes was reduced. This does not directly affect the MMDM temperature, since the diodes are no longer in direct contact with the MMDM, but it does affect the measured temperature.
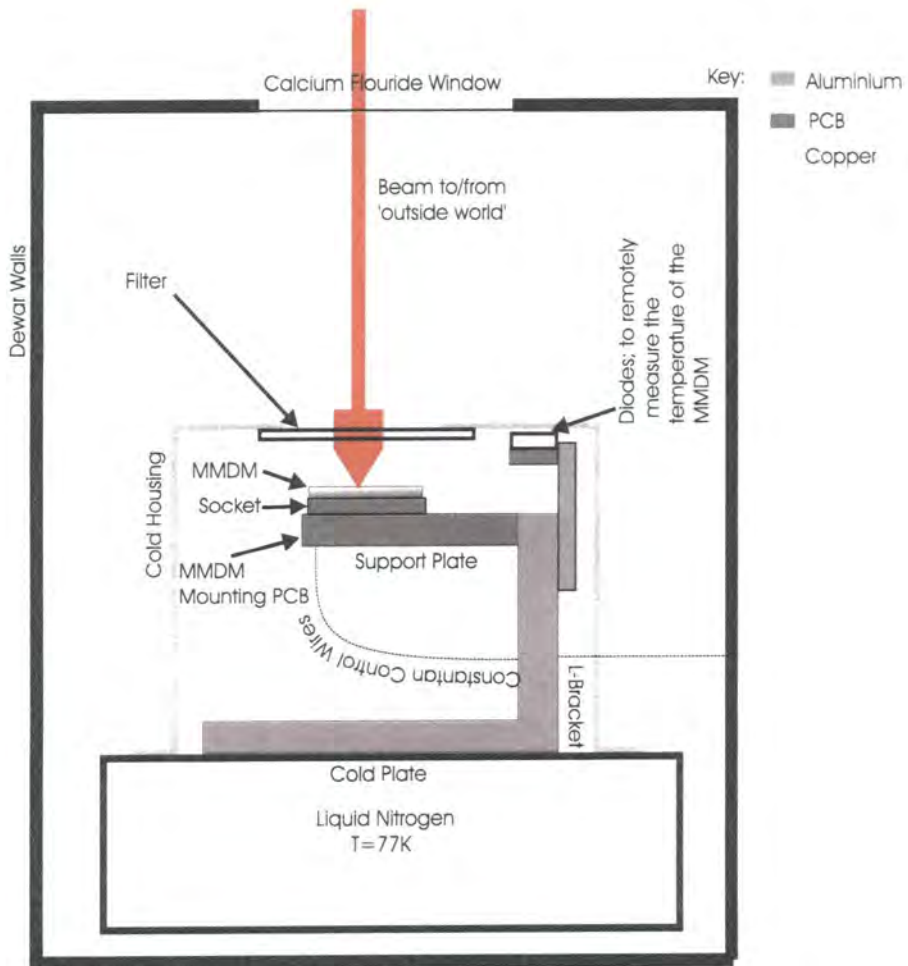
The re-designed mount is shown in Figure 3.2:

Figure 3.2: Micro-Machined Deformable Mirror Re-designed Mechanical Mounting

3.6 Experimental Verification of New Design Improvements

Having installed the re-designed mechanical mounting within the dewar, it was necessary to verify that lower temperatures were indeed being attained. In the course of evaluating the validity of having the diode thermometer remote from the MMDM, a diode was attached to the cold plate. Hence, the capability to measure the cold plate temperature was gained. In the first test run after installing the re-designed mount, a cold plate temperature of 79±0.5K was measured, with a MMDM temperature of 80±0.5K. In subsequent operation of the re-designed mounting, temperature of 77±0.5K for the cold plate and 78±0.5K for the MMDM have been measured. Therefore, the re-design achieved it's objective, and tests towards characterising the MMDM at temperatures under 80K could begin.

3.7 Conclusion

In this chapter, the initial mechanical mounting of the MMDM has been introduced. This mounting was determined experimentally to be suitable for cooling MMDMs to 126K, however, the target temperature for this work was 80K. These experiments introduced the use of diodes as thermometers. A model was constructed to evaluate the power balance within the system at equilibrium to investigate why the initial mechanical mounting did not cool an MMDM to 80K. From this model, it was determined that the most significant factor in raising the MMDM temperature was the radiation inflow from outside the dewar, which contributed to over 93% of the power into the MMDM. Hence, a new mechanical mounting was designed. This new design involved a fundamental change in the cooling mechanism for the MMDMs: instead of drawing power away from the MMDM through thermal conduction, a filter was introduced to prevent the radiated power from reaching the MMDM. The model predicted that the power absorbed by the MMDM would be reduced by 10^4, from 73.1mW, to 0.008mW. A remote sensing approach to measuring the temperature of the MMDM is outlined, along with experimental verification of this technique. It is then shown by experiment that this new mount cools MMDMs to 78K. Hence, this new mount design is suitable for the characterisation of the MMDM properties at cryogenic temperatures.

Chapter 4

Static Characterisation of Micro-Machined Membrane Deformable Mirrors

4.1 Introduction

The static characterisation of the MMDM at cryogenic temperatures is vital to the applicability of MMDMs as a solution to the problem of wavefront correction at cryogenic temperatures. If the shape of the membrane cannot be controlled at 78K, then it cannot be used as a wavefront corrector at this temperature. To this end, it was necessary to study the static properties of the MMDM at cryogenic temperatures, and, for comparison, at room temperature. In this chapter, a method to accurately measure the surface figure of a deformable optical element is described. This method is then applied to a sample of three MMDMs. From this, the effect on the initial surface figure of an MMDM of cooling the MMDM to 78K is shown, both qualitatively through false coloured phase maps, and quantitatively in terms of Seidel aberrations. Subsequently, the effect on the influence functions of cooling the MMDM to 78K is shown. It should be noted that the literature already contains room temperature actuator influence functions for MMDMs (Dayton et al. 2000), however, the properties of a given MMDM may vary from one batch to another, so it was deemed prudent to examine these properties again. Some of the work within this chapter has previously been published (Dyson, Sharples, Dipper and Vdovin 2001).

4.2   Surface Measurements

4.2.1   Optical Arrangement

There are two static mechanical properties of the membrane of interest; the initial surface
figure, and the influence function for a given actuator. Both of these measurements
essentially break down into a measurement of the membrane surface. Hence, for this
project, a Zygo PTI interferometer was used 4.2.2. The set-up is illustrated in Figure 4.1.
For clarity, the beam expander and collimator are shown as a single lens.
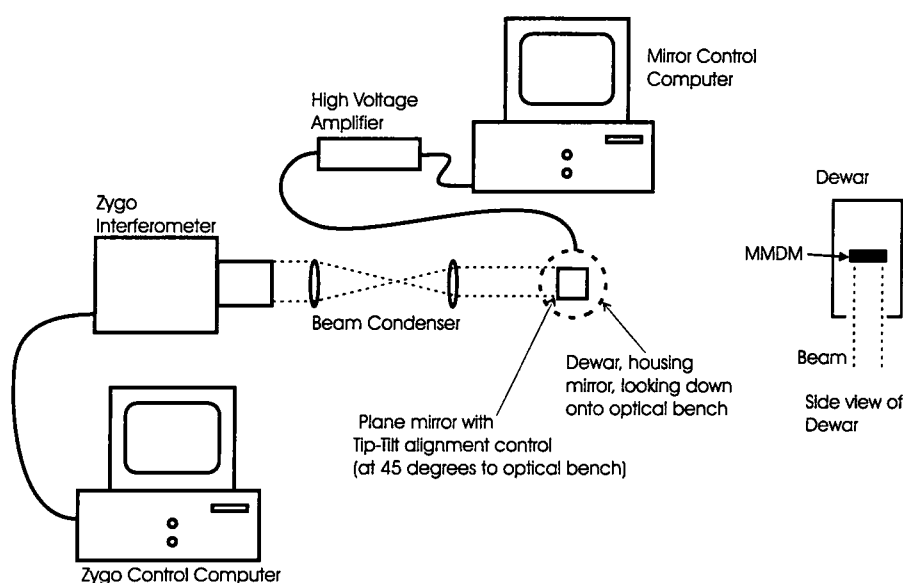
Figure 4.1: The bench set-up for the static characterisation measurements

Some points are worth remarking on; firstly, the laser used in the Zygo is a Helium-
Neon laser of wavelength λ=633.9nm. The beam condenser was used since the smallest
beam diameter of the Zygo was 33mm, which would mean that only a quarter of the beam
was being utilised when studying a 15mm diameter mirror. Hence a beam condenser
was utilised to match the beam size to the MMDM size and make optimum use of the
resolution of the CCD camera within the Zygo. The beam condenser was the cause of
some aberrations in the measurements. The impact was assessed and minimised by the
use of a flat mirror to reflect the beam back to the Zygo, and quantifying the alignment
with the Zygo software.

The dewar (see Section 3.2) containing the MMDM (see Section 2) had to be mounted
vertically, with the mirror pointing downwards, in order to prevent the liquid Nitrogen
from pouring out. Hence the need for the fold mirror. This was also the reason why the

interferometer was used in a horizontal configuration, rather than a vertical configuration. Had the dewar been mounted vertically with the Zygo pointing downwards from above the dewar, it would have been impractical to cool the dewar. However, if the dewar were above the Zygo, the turbulent affect of the liquid nitrogen vapours would have been a problem; and the effects of the condensation on the Zygo and reference flat may have been problematic.

4.2.2 Principle of operation of the Zygo PTI Interferometer

The principle of the Zygo PTI interferometer is in essence similar to the Fizeau interferometer, as illustrated in Figure 4.2. In this configuration, the interference fringes are generated by the path length difference between the beams reflected off the test surface and reference flat respectively. Two features of the Fizeau interferometer are worth commenting on. Firstly, it is heavily reliant on the use of a laser, since a coherent light source is required due to the unequal path configuration. Secondly, the Fizeau interferometer has a huge advantage over most other interferometer designs in that the wavefront degradation due to the expanding optics and beam splitter before the reference flat is eliminated since the reference and measurement beams both travel through the same optical system.
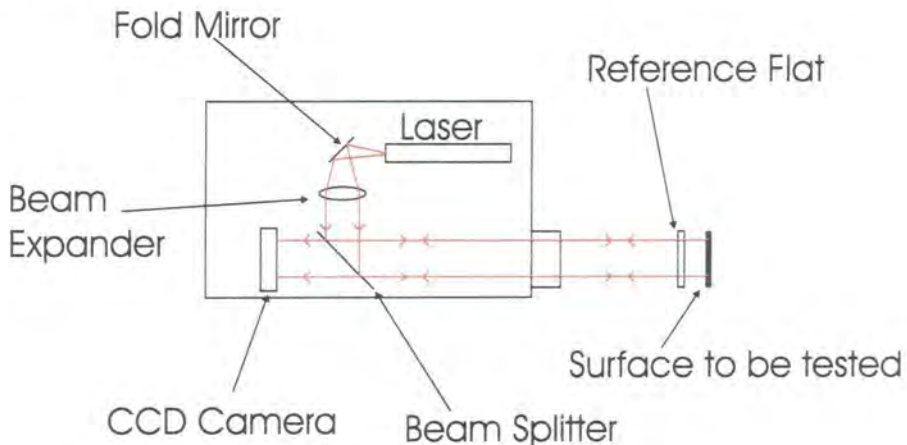
Figure 4.2: Principle of operation of a Fizeau interferometer

The Zygo PTI interferometer adapts this arrangement as shown in Figure 4.3. There are two major differences. Firstly, a piezo-electric transducer is added between the collimator and the reference flat. This translates a control voltage to a displacement and moves the reference flat, hence changing the optical path difference between the reference surface and the surface to be measured (Soobitsky 1985).
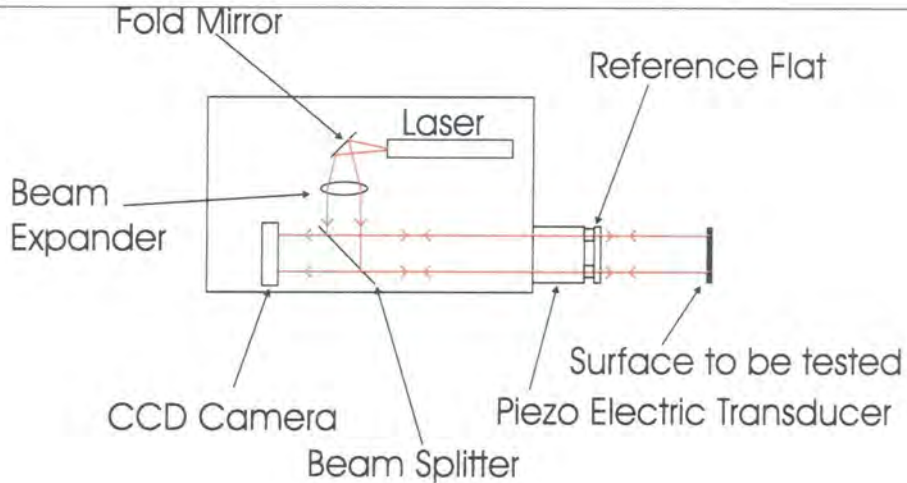
Figure 4.3: Principle of operation of the Zygo PTI interferometer

The second difference is the addition of an alignment arm (not shown) which simplifies the alignment of the optical system. This is a huge practical advantage, although it is not a fundamental design difference (Domenicali and Hunter 1980).

Three images are captured by the hardware, with different phase shifts applied. A surface map is then constructed by the ZyMOD software (Zygo Corporation 1992). There are numerous advantages associated with the phase-shifting interferograms, compared to conventional Fizeau interferograms, some of which will be highlighted here. The first advantage is that, since the phase is being modulated in a known way, the polarity of the wavefront can be definitively measured. For example, it can be determined whether a surface being measured is concave or convex.

Phase-shifting also yields two significant advantages with respect to the intensity of the measurement beam. Firstly, the measurements are intensity independent. This was critical to this project, due to the number of surfaces between the interferometer and the MMDM[1]. Secondly, measurements can still be taken with low contrast fringes.

The single most significant advantage of phase-shifting is, however, precision. The phase measurement error is limited solely by the detector noise. This enables very accurate measurements to be taken under normal circumstances[2].

---

[1] There are 9 surfaces between the reference flat and the MMDM, as can be seen in Figures 4.1 and 3.2, each leading to some light loss through reflection

[2] quoted accuracy is better than $\lambda/50$ peak to valley

4.2.3 ZyMOD Software

Having understood the physical aspects of the Zygo PTI interferometer, it is necessary to examine the ZyMOD software that drives the hardware and translates the three images into a surface map. The software has to drive the phase-shifting PZT as well as collecting the data from the interferometer. After collecting the images to be analysed, the software, knowing the phase shifts that have been introduced through the PZT, can reconstruct the surface to great accuracy. The details of the various options to tweak the configuration are not important; however some of the features of the software are significant. The software is capable of determining the aperture within which measurements are required without user intervention. This is due to the fact that the areas outwith this aperture do not reflect, and hence the signal detected by the CCD camera will not vary with changing voltage to the PZT.

The surface map is saved in a proprietary data format. This can be converted to more portable formats, as the data format is well-documented (Zygo Corporation 1992). The surface map can be decomposed into the coefficients of up to 36 Zernike polynomials[3], with some loss of accuracy. The software also describes the wavefront by the five 3rd order Seidel coefficients, again with some loss of accuracy[4]

One other feature of the software that was invaluable to this project was the ability to subtract one wavefront from another. In this way, small deviations from the initial surface could be measured by subtracting the initial surface from a new result. It will be seen how useful this was in Section 4.4.4.

4.3 Additional Software

The control of the Zygo is only one of three areas where software was important for the static testing of the MMDM. There was also extensive work done on the MMDM control software, and on data analysis scripts. It was necessary to re-write the MMDM control software since the original software was of limited functionality, for a specific task; while for this project a more general approach was considered important. The need for script-based image analysis is clear once the number of files concerned is understood. Assuming a bare minimum of one image for each of the three MMDMs unpowered, and one for

---

[3]Defined as per the University of Arizona's FRINGE program (Zygo Corporation 1992).

[4]The Seidel coefficients are chosen to minimise the RMS wavefront fitting error, rather than to follow the strict definition of the Seidel aberrations, see (Zygo Corporation 1992).

each of the 37 actuators at a given voltage, in the two minimum environments[5] a total of 228 raw images had to be processed. Each of these had to be converted into a more portable format than the proprietary Zygo format, cropped to a reasonable size and then false-coloured. In addition, there is the necessity for repeated measurements, and other environments; such as comparing room temperature results with and without the vacuum, or examining intermediate temperatures. Some form of automation is obviously required.

4.3.1 Static MMDM Control Software

The original software to control the MMDM consisted of two programs written in C, each of which was based on the software provided with the MMDMs. Both programs ran under MS-DOS. These programs were written by Sebastian Bonicel (Bonicel 1999), having been based on the programs supplied with the MMDMs by OKO Technologies. The static control software allowed the user to select an actuator with the cursor keys, and then to change the voltage applied to that actuator in 5V increments. This software was adequate for the characterisation of the 19 channel MMDMs static properties.

It was decided to completely re-write the MMDM control software, rather than attempt to modify the existing software. This was partly motivated by a desire to use more modern tools, since the original software ran under MS-DOS. Once the decision was made to switch to Windows NT 4, it became necessary to choose a programming language. For simplicity, the original C was dropped in favour of National Instruments' LabVIEW, a much higher level programming language. This was in order to achieve a more rapid development cycle, particularly with regard to re-designing the interface. A further reason for re-writing the software was the need to drive 37 MMDM channels, through two 20 channel digital to analogue converter (DAC) cards, rather than the 19 channels through one card, driven by the original software. The software was completely re-written for two reasons; firstly, it was necessary to use a more sophisticated user interface for the control of the 37 channels. Secondly, it was decided that re-writing the software would probably take less time than modifying the original software to control the 37 channels.

The requirements for the control software were straightforward. The algorithm for the software was:

Initially, the re-written program for static testing was intended to be a separate entity from the dynamic testing software (see Section 5.3). However, the two developments merged, since the requirements for the static testing software are a subset of those for the

---

[5]At temperatures of 77K and ambient

Set all MMDM channels to 0V (Note: upon computer switch-on, the DAC
channels are set to random voltages)

Provide user with a reminder of the safe switch on procedure for the MMDM
power supplies

LOOP

    Read front panel controls for desired actuator voltages

    Check which actuators have been altered from previous iteration

    FOR each changed actuator

       IF actuator signal outside safe range, coerce into safe range

       Apply each new actuator voltage

    NEXT actuator

UNTIL user stops program

Provide user with a reminder of the safe switch off procedure for the MMDM
power supplies

Table 4.1: Pseudo-code algorithm for the static control software of the MMDMs.

dynamic testing software. Hence, maintaining two sets of software was unnecessary.

4.3.2 Data Analysis Software

The analysis of the initial surface figure data from the Zygo PTI interferometer consisted
of three steps.

The first step was to convert the images from the proprietary image map format output
from the ZyMOD software into something more portable. This was achieved using the
map2pgm program previously installed on the Zygo control PC. A bash shell script was
set up to run this conversion program on all of the data files.

The second step was to re-scale each image so that comparisons between different
experimental results could be made. This was necessary since the ZyMOD software
automatically scales the output data to fill the 8-bit intensity range available. Therefore,
to compare two different results, it was necessary to scale the one with the smaller peak
to valley deviation by the ratio of the peak to valley deviations, and hence reduce the
intensity range used by this image.

The final step was to false colour the images to highlight the detail within them.

The problem of analysing the influence function data was slightly more complicated, but can be delineated into four steps.

The first step was again to convert the images a portable image format.

The second step was to subtract the relevant initial surface figure from the influence function. This was necessary since the initial surface figures were substantially larger than the influence functions in some cases, so the detail of the influence function was lost. It also allowed more meaningful comparisons to be drawn between different results. This was done using the Image Magick suite of image processing tools (Image Magick Studio 2001). Due to noise effects caused by diffraction at the edges of the images, a median filter was also applied to remove single pixel features.

The third step was to normalise each image to fill the intensity range available to highlight detail.

The final step was to false colour the images. Cross sections through the final images were taken using a perl script, which were then re-scaled to match the measured peak to valley values.

4.4   Results

The static testing results are broken up into two sections, initial surface figures and influence functions. The initial surface figure is a map of the surface of the membrane without applying any control voltages. The results in this section were obtained by re-mounting the MMDM in such a way that only one pin was in the mounting socket. The purpose of this single point mount was to ensure that mounting stresses did not contribute to the initial aberrations, in order to isolate the deformations inherent to the device; in other words, to measure the optimum initial surface figure for each MMDM. These results will be presented in the quantified form of the Seidel aberrations for each measurement, and the qualitative surface map image.

The influence functions are a map of the deviations from the initial surface figure caused by poking each individual actuator. Hence, each MMDM has 37 influence functions, one for each actuator. These are shown after having had the appropriate initial surface figure removed in each case. Cross sections through a sample of the influence functions will also be included to facilitate better comparisons between the results.

4.4.1   Initial Surface Figures

The cooling process introduces aberrations to the membrane surface due to differential thermal contraction between the dissimilar materials in the MMDM construction. The initial figures are shown here as false coloured contour plots of the membrane surface. The surface figures were taken under a variety of circumstances. The first two sets are at room temperature; one at atmospheric pressure and one evacuated. Then results were taken at 78K, again evacuated. Finally, results were taken at intermediate temperatures with the dewar evacuated. The reason for taking so many results was that it was hoped that the effects of evacuating the dewar could be discriminated from the effects of the cooling process itself.

Before presenting the experimental data, there are a few points to note. Firstly, the image rotations from one result to the next are not necessarily the same. Secondly, only one result for each case is presented. Many more were taken, but, for reasons of brevity, are not included here. The presented result is a *typical* result for each case. Finally, all of the presented images are false coloured to the same scale. This has been done to aid comparison between one result and another; however, the consequence is that there is not much detail to be observed in the warm results.

4.4.2   Seidel Aberrations

Plots are presented below of the variation of the major Seidel aberrations with the temperature of each MMDM, with the differences between the MMDMs having been defined in Figure 2.8. The data are presented with the tip/tilt on the MMDM having been subtracted in software. In addition, the diameter of the image that is analysed is about 95% of the diameter of the measured image. This is due to the Zygo's limited handling of diffraction effects from the edges of the membrane surface. It should be noted that the set-up prevents the MMDM being at an equilibrium temperature between 78K and room temperature; it is always either cooling down or warming up.

Since the MMDM cannot be held at an equilibrium temperature other than at room temperature or 78K, the absolute errors in the recorded aberrations have been taken to be constant with temperature, and the measured errors from the cold measurements have been applied to each data point. It is obvious from the plots (Figures 4.5, 4.6) that the scatter on the measurements is much greater for larger aberrations. This is not an effect of the low temperatures involved, as can be seen by examining the plot for MMDM A

(Figure 4.4). Despite similar temperatures, the scatter is much smaller. Therefore, it is assumed that the Zygo interferometer becomes less accurate for large aberrations, that is, aberrations leading to a peak to valley displacement of the membrane surface greater than about 8λ. The peak-to-valley (P-V) values recorded incorporate higher order terms than the individual Seidel aberrations presented, and so are not a simple sum of the other presented aberrations.
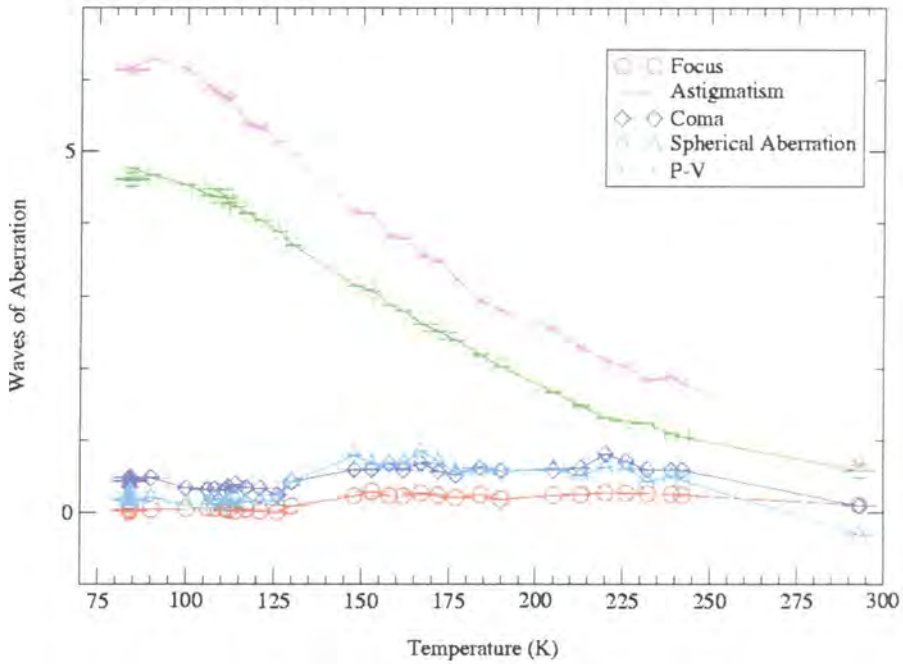

Figure 4.4: Variation of Zygo-measured aberrations with temperature for MMDM A

The results for MMDM A (Figure 4.4) show that a substantial fraction of the MMDM's dynamic range ($\approx 11\mu m \approx 18\lambda$) remains after correction for static aberrations at cryogenic temperatures. It should be noted that, were it possible to remove the astigmatism, the MMDM would scarcely be affected by the cooling process.

The results for MMDM B (Figure 4.5) show very different behaviour from the first MMDM. Cooling this MMDM results in a P-V membrane displacement of $9.78 \pm 0.09\lambda$. The predominant contribution to this behaviour is again astigmatism. However, with this MMDM, the other aberrations are also on a significant scale, particularly Coma and Defocus. These results clearly indicate that this MMDM possesses considerably greater aberrations at cryogenic temperatures than the first MMDM.
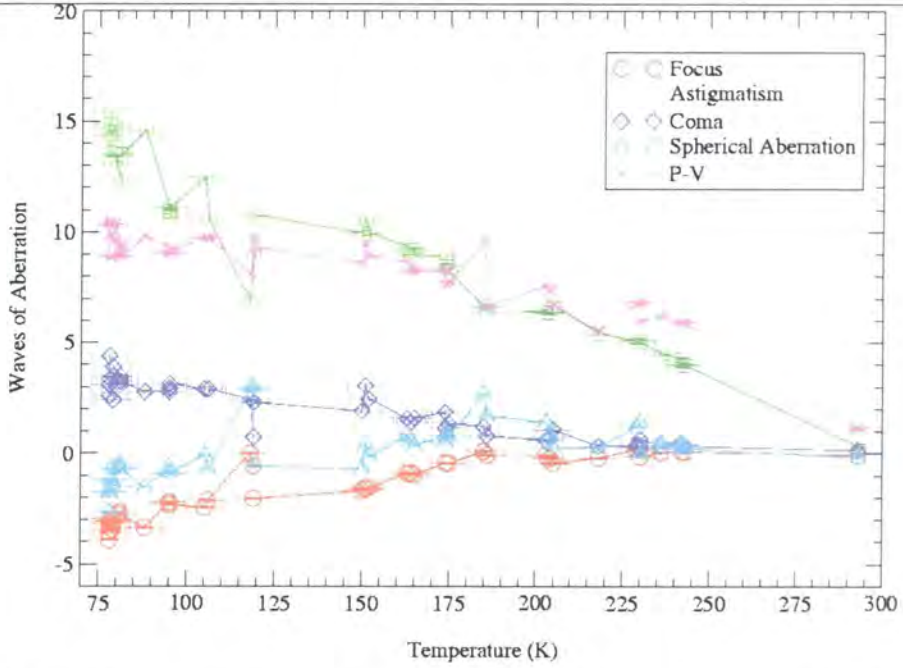
Figure 4.5: Variation of Zygo-measured aberrations with temperature for MMDM B

The results for the final MMDM (MMDM C, Figure 4.6) are distinctly different from MMDM B and are even further from the MMDM A results. The P-V MMDM displacement here is 10.14±0.06 λ, which is only marginally greater than for the second MMDM. However, the contributions from the various individual aberrations are different to those for MMDM B. In particular, both Spherical Aberration and Defocus are larger in magnitude.
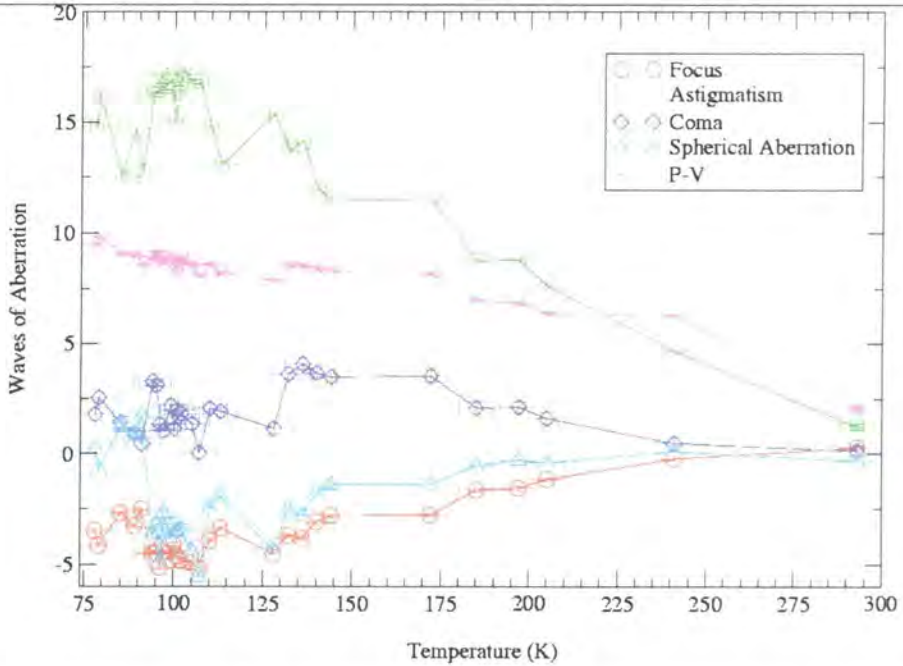
Figure 4.6: Variation of Zygo-measured aberrations with temperature for MMDM C

4.4.2.1 Discussion of Seidel Aberrations

Perhaps the most striking aspect of the preceding initial surface figure Seidel aberration results is that astigmatism is consistently much greater than any of the other aberrations. This could be due to two effects. The initial surface figure of the MMDMs also has astigmatism as the most significant aberration, so the cooling process could simply be amplifying the aberrations already present in the system. The second, and more intriguing, possibility is that the astigmatism is caused by the contraction of the rectangular wafer. A future experiment of some interest would be to study the initial aberrations of a MMDM on a circular mount. This would hopefully lead to the major aberration becoming defocus or spherical aberration, which are simpler to correct with fore-optics.

4.4.3 Phase Maps

The change in the MMDMs caused by cooling to 78K can perhaps be best illustrated through the use of phase maps of the MMDM's surface, measured using the Zygo PTI interferometer (Zygo Corporation 1992). These maps have been false-coloured to indicate regions of constant phase. In each case, one image is presented from the cold measurements, at a temperature of 78K, and one from the room temperature measurements. Note that the image rotations are not necessarily the same between the cold images and the warm images.

The images for MMDM A (Figure 4.7) show the increase in astigmatism caused by cooling. Note that the false-colour map used has been scaled for a total P-V displacement of 10λ to better illustrate the maps for the cold MMDMs. Hence there is very little detail visible in the warm maps.
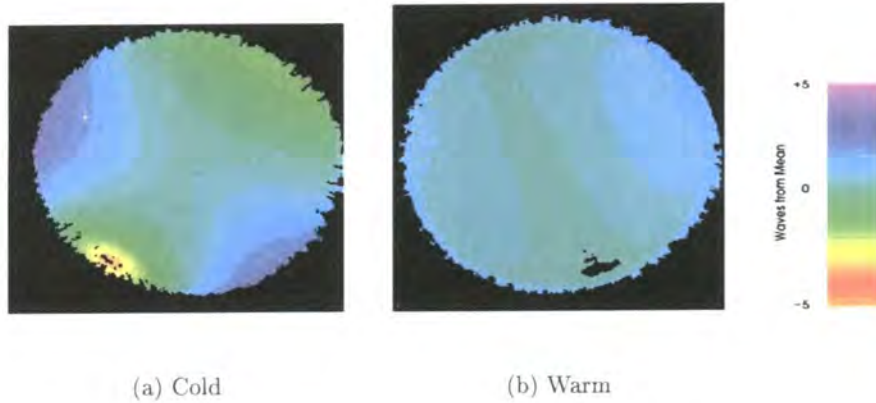

(a) Cold   (b) Warm

Figure 4.7: Initial surface figures for MMDM A.

The phase maps for MMDM B (Figure 4.8) illustrate the scale of the effect on the revised MMDMs of cryogenic cooling. The void at the lower-left hand corner of the image was due to the aberrations caused by cooling the MMDM, which meant that the reflected light did not return to the Zygo camera.

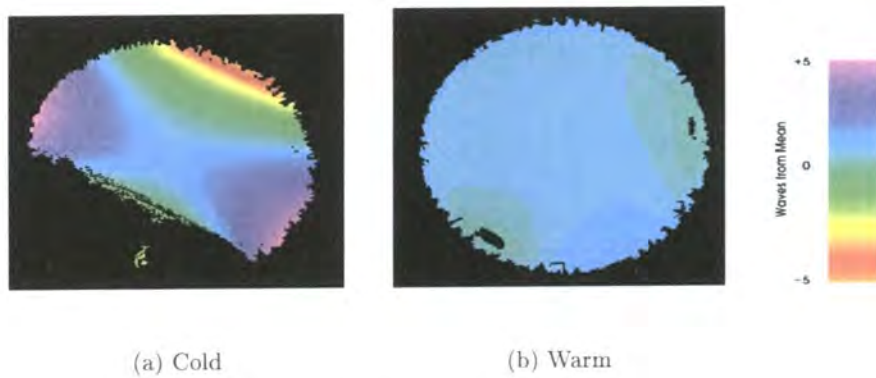
(a) Cold   (b) Warm

Figure 4.8: Initial surface figures for MMDM B

The image presented for MMDM C is shown in Figure 4.9 Again, the void at the lower left of the image was due to the aberrations on the MMDM. This was verified through the use of a beam-splitter and a screen at a similar optical path length from the MMDM as that from the MMDM to the Zygo. This image clearly shows that the MMDM surface is heavily deformed by the cooling process.
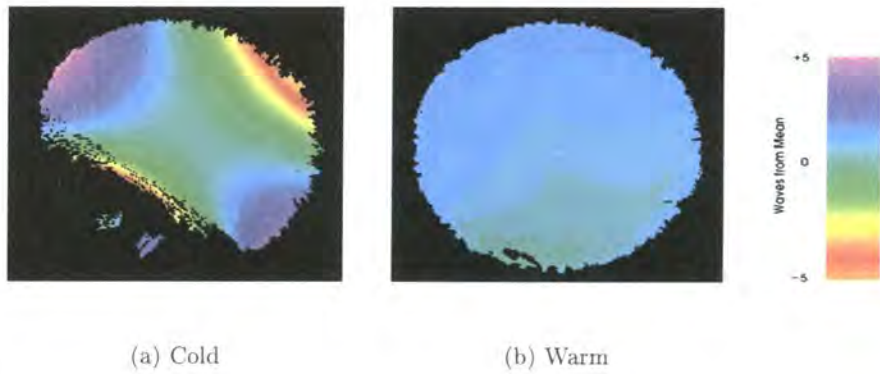
(a) Cold   (b) Warm

Figure 4.9: Initial surface figures for MMDM C

These results indicate that there is a large variation in the initial surface figure of a cryogenically cooled MMDM depending on the specific MMDM used. For these experiments, MMDM A came from an earlier batch than MMDMs B and C. Indeed, MMDMs B and C are quite likely to have come from the same batch. It is clear that MMDM A is less affected by being cooled to 78K. Potential causes for this have been discussed in a private communication from Gleb Vdovin (Vdovin 2001a). Four parameters are varied from one batch of MMDMs to another. These are:

1. membrane thickness (composite, Al + nitride)

2. ratio of nitride thickness to aluminum thickness

3. tension of nitride

4. tension of aluminum

Unfortunately, the values for these parameters for the MMDMs tested here are not known. However, given the differences in the coefficients of thermal expansion for the dissimilar materials used in the MMDM construction, summarised in Table 4.2, it seems likely that the crucial factor for cryogenic operation is the ratio of nitride thickness to aluminium thickness. For infrared operation, a gold coated membrane would be used rather than aluminium, for better infra-red reflectivity. The coefficient of thermal expansion of gold is closer than aluminium to that of silicon, so a gold coated membrane may cope better with the stress of cryogenic cooling.

4.4.4 Influence Functions

The influence function of each actuator in a modal wavefront corrector is simply the phase change introduced to a wavefront for a given signal to that actuator. This is equivalent to

Material	Coefficient of thermal expansion at 25°C (K^{-1})	Source
Aluminium	25×10^{-6}	(Weast 1975-1976)
Silicon	3×10^{-6}	(Weast 1975-1976)
Gold	16×10^{-6}	(Weast 1975-1976)
Silicon Nitride, Alpha	2.90×10^{-6}	(Shackleford 1997)
Silicon Nitride, Beta	2.25×10^{-6}	(Shackleford 1997)

Table 4.2: Coefficients of thermal expansion for MMDM materials. Note that Silicon nitride forms one of two crystal structures, denoted by alpha or beta.

the change in the MMDM's surface map caused by applying a voltage to a given actuator in this case (although the phase change is actually twice the membranes displacement at a given point due to the reflection of the wavefront).

For the results presented here at 78K, the influence functions were swamped by the initial surface figure deformations of the membrane outlined above (see Section 4.4.1). Consequently, it was necessary to do some image processing to the surface maps obtained for the influence function data. Due to the number of influence functions involved (37 for each of 3 MMDMs in 3 sets of environmental conditions), this process was automated, through a mixture of bash shell scripts, perl, C and some tools from the Image Magick toolkit (Image Magick Studio 2001). For more detail of the image processing done, see Section 4.3.2.

4.4.5   Influence Function Phase Maps: MMDM A

The actuator numbering scheme utilised here is as given in Figure 2.8 in Section 2.3, although the results are mirror-imaged and rotated relative to the numbering scheme. The actuators are described in terms of zones, where the actuators within each zone are defined by Table 4.3. The false colour maps run from black, meaning no change at all from the reference image, through green indicating a small change, yellow, red blue and white, indicating the region with the greatest deviation from the reference.

The final false coloured phase maps are presented here. Figure 4.10 and Figure 4.11 shows the influence functions for MMDM A at room temperature and at 78K respectively. This device has a 1.75mm center to center spacing between actuators, hence the edge

Zone	Actuators
0	1
1	2-7
2	8-19
3	20-27

Table 4.3: Definition of actuator zones

actuators in zone 3 are very close to the the fixed membrane boundary, with the gap from the edge of the aperture to the center of the outermost actuators being 1.375mm 2.8.

In general, the room temperature results and the cold results for MMDM A are similar. This will be further illustrated in Section 4.4.9, where selected cross sections will be presented. It should be noted that all of the results presented here are individually normalised, to exploit the full range available from the false colour map in order to enhance the detail in the structure. This does mean that no valid comparisons between the magnitude of different results can be made here; however, this will be explored by examining the cross sections through the influence functions in Section 4.4.9.

In zones 0 and 1, the room temperature result gives a clearly defined influence function. These functions are roughly circularly symetric, although some hexagonal structure is visible in the zone 0 result. This is due to the actuators being hexagonal. The 78K results for zones 0 and 1 are similar to the room temperature results, albeit noisier. Some errors in the subtraction of the reference flat can be seen, particularly in the cases of actuators 2, 4 and 5. In the case of actuator 4, this error appears to be symmetric, across the diagonal from the lower left corner to the upper right. This would be indicative of an astigmatic residual, which would be expected since the predominant aberration in the reference image is astigmatism.

The case of zone 2 is similar to that for zones 0 and 1. In the room temperature results, the most noticeable feature is that the images for zone 2 are noisier. This is due to the reduction in the membrane throw for actuators closer to the edge of the membrane, which means that the signal to noise ratio is lower. Hence, when the signal is amplified to use the full range of the false colour map, more noise becomes visible. This phenomenon is equally prevalent in the 78K results. Note that the predominant residual artefact is again astigmatic, as can be seen in the results for actuators 14, 15 and 16. In the specific case of actuator 10, the residual appears to be predominantly circularly symmetric, indicative

of a focus error or spherical aberration. This is almost certainly due to an error in the reference flat subtraction.

The final set of actuators, zone 3, is perhaps the most interesting set in this data. For all of these actuators, it is apparent that the signal is further reduced from the case for zone 2, hence the residual error from the image manipulation stage is even more prominent. However, the results are still useful. Since the six corner actuators (20, 23, 26, 29, 32 and 35) should be closest to the boundary, they should also have the weakest signals. While this is true for most of the corner actuators, both actuators 20 and 35 have strong signals. This leads to the hypothesis that the actuator pad is actually offset marginally from the membrane, in the direction from actuators 20 and 35 towards actuators 26 and 29, resulting in actuators 26 and 29 being closest to a membrane edge, while 20 and 35 are the furthest corner actuators from the edge. It should be noted that the residual errors after subtracting the reference will probably be greatest for the zone 3 actuators due to the initial reference flat being taken before the results, with the results proceeding in order of actuator number. Hence, any deviation in the optical alignment, through for example, thermal contraction or expansion of the mountings holding the beam condenser, will result in the reference flat being less accurate for the later results. In the case, the results were taken in the order of the actuator numbering scheme, so the reference flat will be most accurate for actuator 1 and least accurate for actuator 37.

The 78K results for zone 3 are again similar to the warm results, although there is a greater random noise component and less reference subtraction error. Again, actuators 20 and 35 have the strongest signal of the six corner actuators. A point to note about actuators 23, 24, 26, 29 and 32 of the 78K results, and 23, 25, 26, 27, 28, 29 and 32 of the room temperature results, is that the false colouring scale picks out the largest variation from the reference as white, and in these cases this is not at the actuator itself. Some of these results, for example, actuator 27 of the warm results, have the highest points at an edge of the aperture. This is due to the presence of diffraction effects at the edge of the MMDM aperture. The Zygo PTI does not handle these diffraction effects well. Consequently, in the image processing phase, a median filter of radius 1 pixel, was applied to all of the images. This removed the worst of the diffraction effects in most cases, however some residual effect remained. A larger radius of filter was attempted, but removed some detail from the images.

Due to the fixed boundary edge, and the limited scale of motion available to the perimeter actuators, OKO technologies revised the actuator pattern by packing the ac-

tuators closer together, resulting in a 1.25mm center to center actuator spacing, see Figure 2.7. This meant that the outer actuators were now centered 2.25mm from the membrane edge. MMDM A was of the first type, with 1.75mm center to center actuator spacing, while MMDMs B and C were of the revised type. Note that there were no other changes to the design.
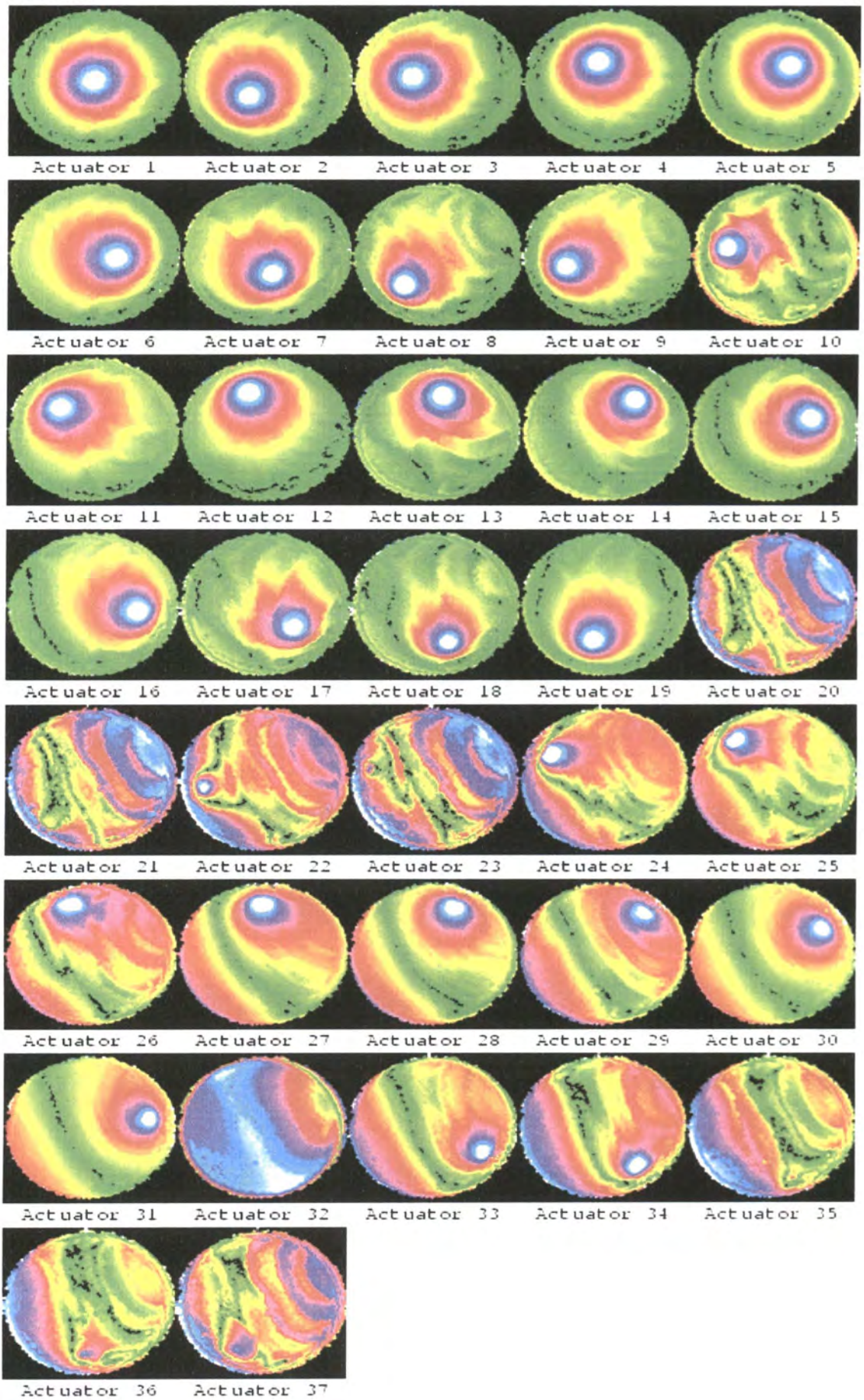
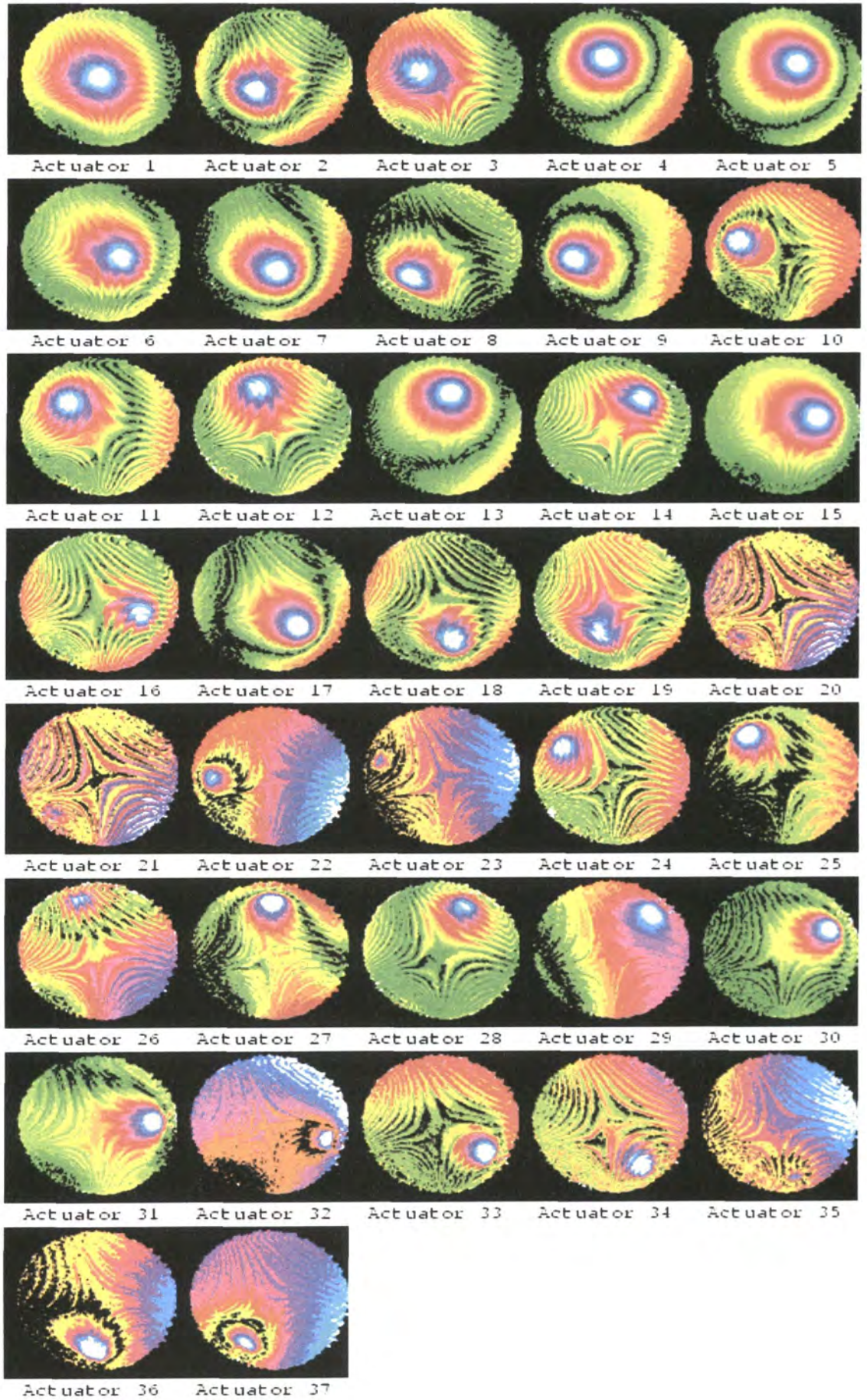Figure 4.10: Room temperature influence functions for MMDM A

Figure 4.11: Cryogenic temperature influence functions for MMDM A

4.4.6 Influence Function Phase Maps: MMDM B

The room temperature results for MMDM B (Figure 4.12) show a dramatic improvement in the signal to noise ratio compared to the results for MMDM A (Figure 4.10. This is entirely due to the actuators being further from the fixed membrane boundaries, and hence causing a larger displacement in the membrane position.

The 78K results for MMDM B (Figure 4.13) have a void towards the lower left, due to the void being present in both the data map and the reference map. This void is due to the aberrations introduced onto the MMDM surface by the cooling process, as explained in Section 4.4.3. In a substantial fraction of cases, the largest deviation from the reference surface is along the edge of this void, affecting the false colouring of the rest of the image surface. It was decided not to apply a larger median filter, or to randomly crop out this data, for two reasons. Firstly, it was felt that it was important to be consistent between the data sets for each MMDM in each environment. This was particularly significant with regard to the median filtering option, since it may have obscured genuine data and made the maps look less noisy than the maps for the other MMDMs. Secondly, information would have been lost from the influence functions of actuators 11-14 and 24-29 should any process be used to consistently remove this edge. Consequently, some loss of detail on some surface maps has to be tolerated.

It is worth noting that some of the void region could be restored by applying a voltage to the relevant actuators, as shown by the results for actuators 25-29. This indicates that the membrane must have been sloping upwards, relative to the actuator pad, from the center to the boundary, as the image was restored by pulling the membrane towards the relevant actuator.
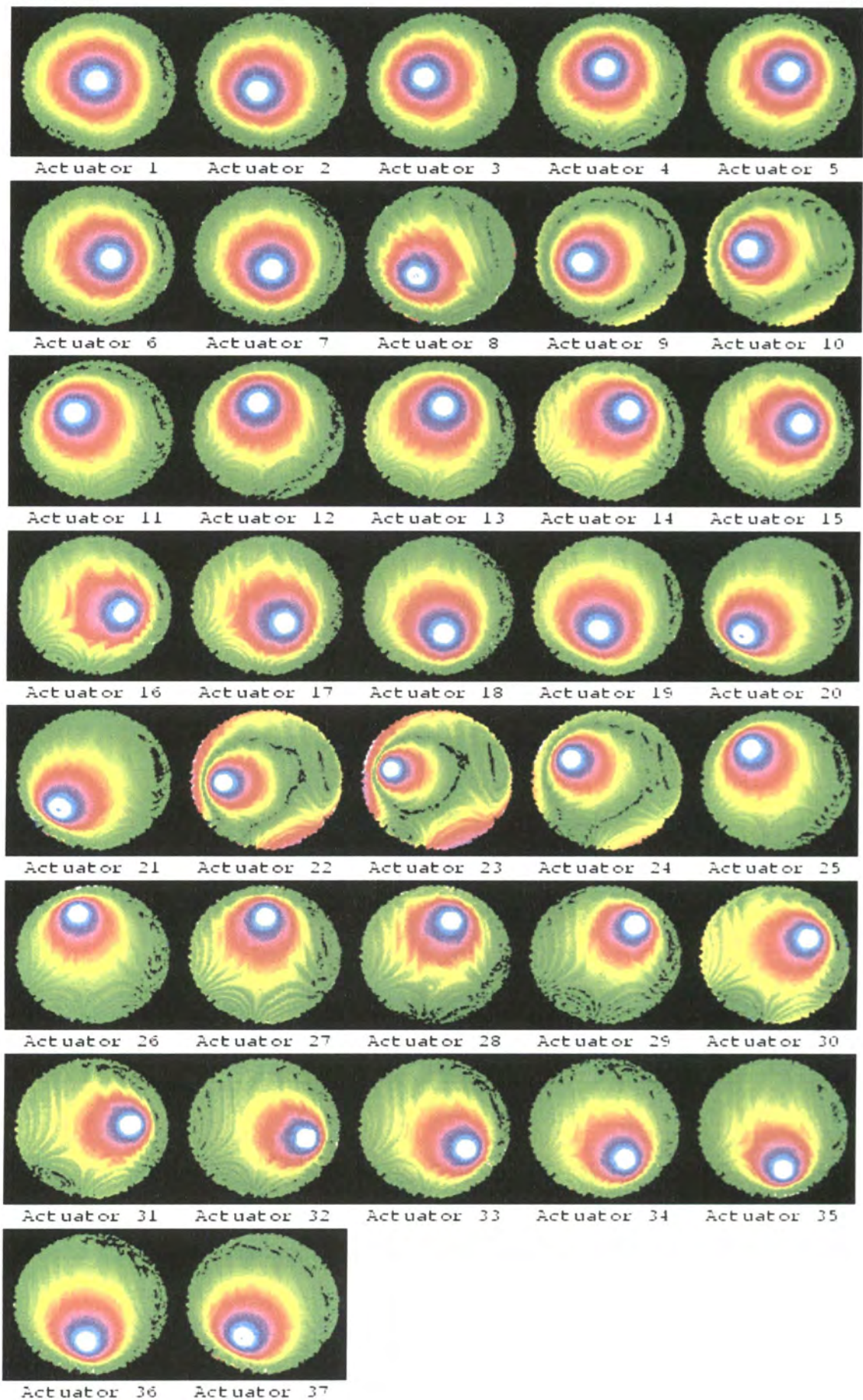
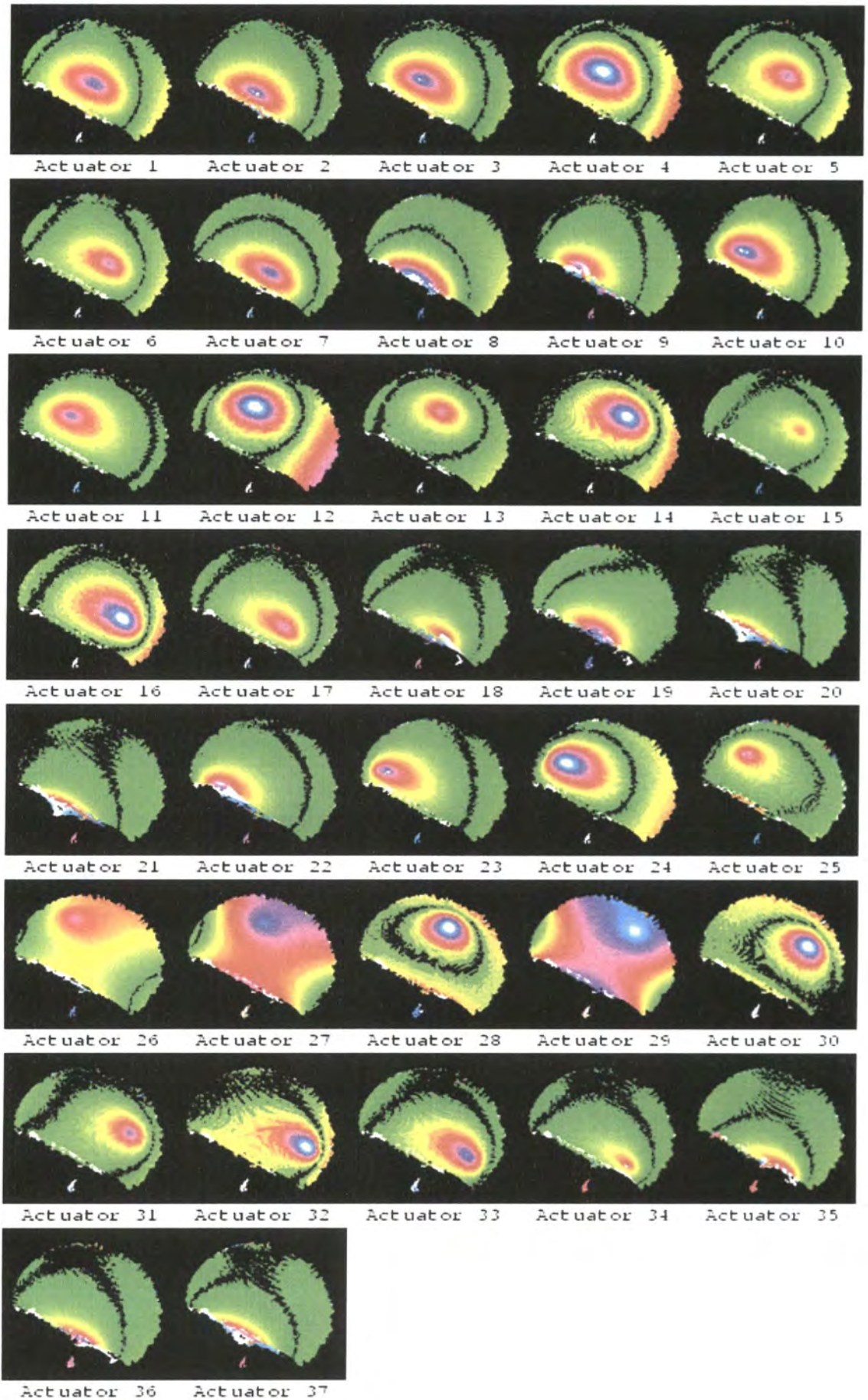Figure 4.12: Room temperature influence functions for MMDM B

Figure 4.13: Cryogenic temperature influence functions for MMDM B

4.4.7   Influence Function Phase Maps: MMDM C

MMDM C may be from the same manufacturing batch as MMDM B; it possesses the same actuator spacing, was part of the same delivery and has very similar experimental properties. The room temperature influence functions (Figure 4.14) do appear to have a systematic error in the reference subtraction, resulting in a residual tilt growing in magnitude from the left hand side up towards the right hand side. Otherwise, the maps look similar to those for MMDM B. The cold results (Figure 4.15) suffer from a similar false colour scaling problem as for the results for MMDM B (Section 4.4.6). Again, the void at the lower left is present. These results, though, appear to have a discontinuity near the edge of the membrane close to the void in some of the results, for example, for actuator 4. This has to be a measurement artefact of some sort, since the membrane was still intact upon subsequently warming the device up, and appeared to be intact to a visual inspection while cold and within the dewar.

For several surface maps, a large reference subtraction error is apparent. However, the remaining surface maps compare well with those for MMDM B. Two small patches can be seen in the void. A similar patch was also observed in the results for MMDM B. It is conjectured that these patches are simply reflections from dust particles on the membrane.
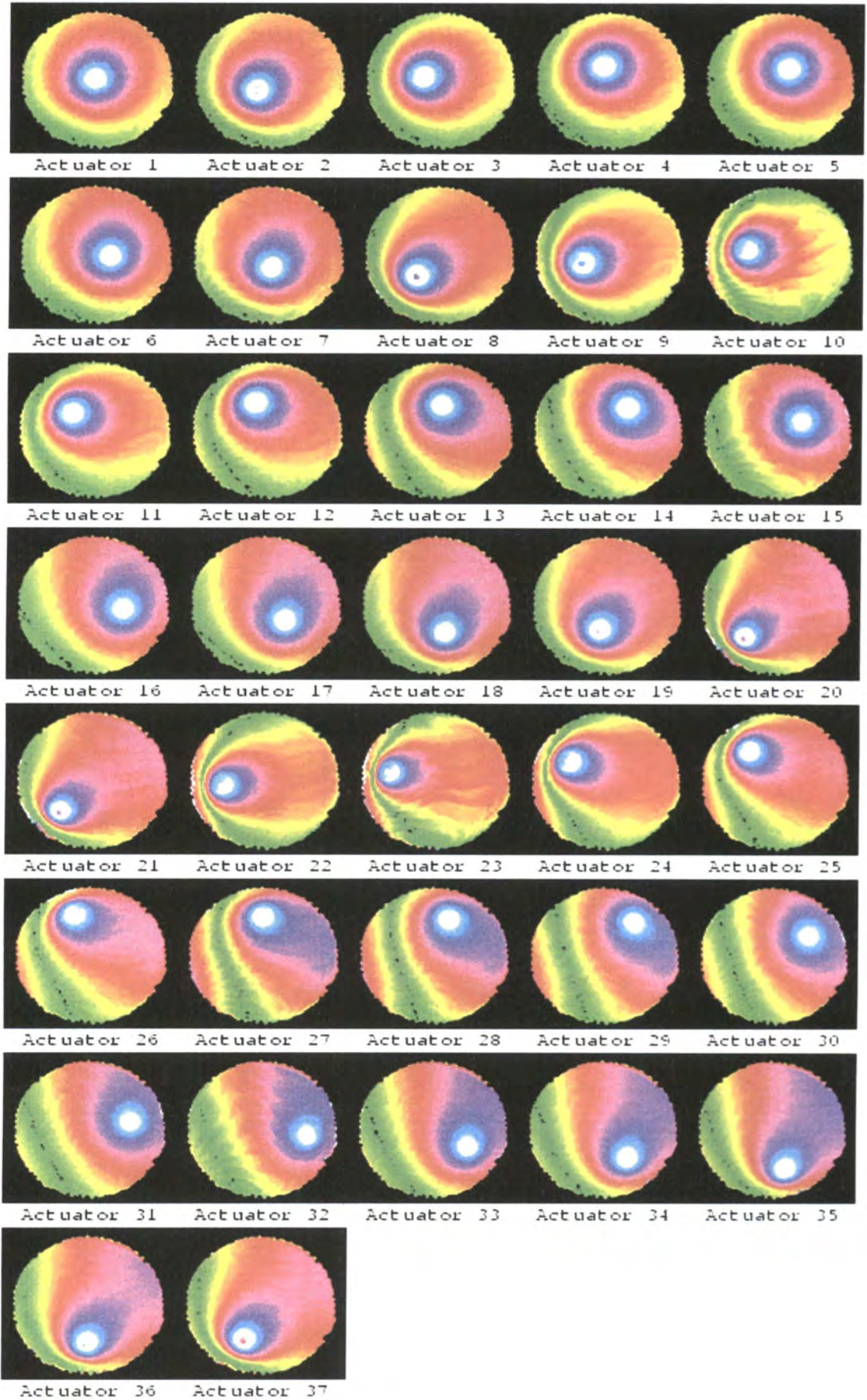
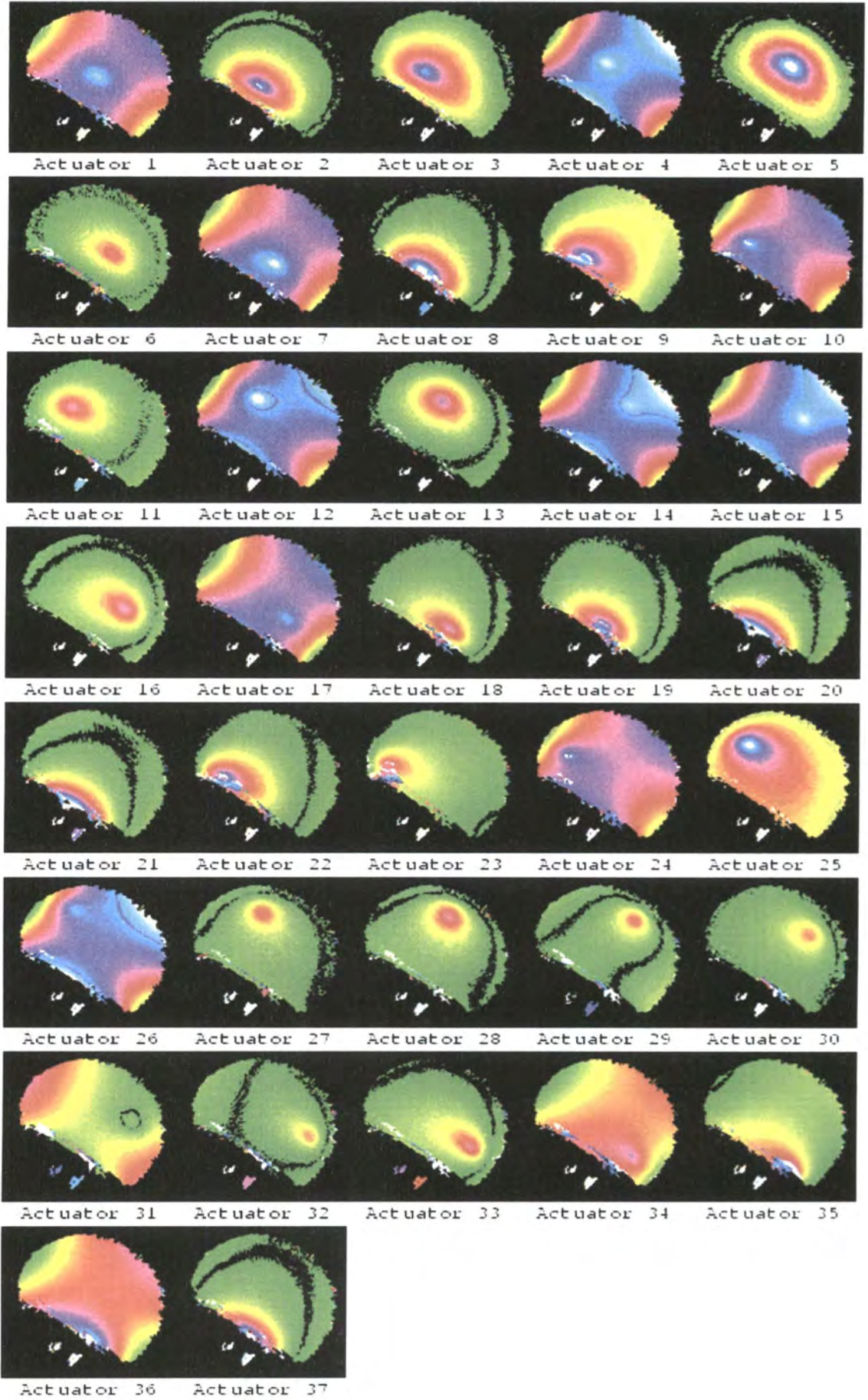Figure 4.14: Room temperature influence functions for MMDM C

Figure 4.15: Cryogenic temperature influence functions for MMDM C

4.4.8 Influence Function Phase Maps: Summary

Before examining the cross sections of the influence functions, the phase map results will be summarised. Several important points have been discussed. Firstly, there are two models of MMDM being tested. The first version had actuators with a center to center spacing of 1.75mm (MMDM A), while the second version had an actuator center to center spacing of 1.25mm. This revision resulted in a substantial improvement in the consistency of the influence functions in a given device from one actuator to the next at room temperature, particularly for the outermost actuators.

Secondly, MMDM A appears to have the closest match between the cold and warm influence functions. This is to be expected, since the initial surface figure is the least distorted of the three MMDMs (see Section 4.4.3.

A final point worth noting is that these influence functions represent the first adaptive optical element technology to have been demonstrated to work at temperatures down to 78K. Furthermore, these devices have been designed for room temperature operation, and therefore there is scope for optimisation of the design and manufacturing process for cryogenic operation.

4.4.9 Influence Function Cross-Sections

Having examined the MMDMs influence functions in a qualitative way, by examining the false coloured surface map plots, it is now necessary to study some quantifiable results from the influence functions. To do this, each image was rotated so that the intensity peak lay along a horizontal line through the center of the image. This line was then extracted and plotted. This did mean that, in some cases, the actuator was missed, due to the peak intensity being a diffraction effect and hence remote from the actuator position. In these cases, the image was rotated interactively to ensure that the actuator was in the correct position.

The cross sections were then scaled so that the peak was in accordance with the peak to valley displacement measured by the Zygo. Finally, the position co-ordinate was scaled to a percentage of the membrane radius. The membrane edge was clearly identifiable within the images, hence was a natural reference for the scaling.

The cross sections were used to answer several specific questions. Firstly, it will be shown that the actuators' influence functions were dependent only on the distance from the center of the membrance, and not on the actuators angular position within the zone

(Section 4.4.9.1). This means that only a triangle of 7 actuators (for example, 1, 2, 8, 9, 20, 21 and 22 from Figure 2.8) would have to be studied to obtain a complete set of influence functions. For clarity, in later sections this has been further trimmed down to a line with one actuator in each zone. Secondly, it was necessary to determine whether evacuating the dewar had any effect on either the shape or the magnitude of the influence functions. This leads to isolating what effect cooling the MMDM had on the actuators' influence functions.

4.4.9.1   Influence Function Cross-Sections: Zones

In the specific case of MMDM A, it has already been established in Section 4.4.5 that the influence functions are not independent of the angular position around the zone for actuators in zone 3, the outermost actuators. In the case of all MMDMs, it is clear that zone 0 can be ignored since it only consists of one actuator.

Hence, one result from each MMDM will be presented to illustrate that the influence functions are indeed independent of angular position around the membrane. One result will be shown from a revised MMDM (MMDM B) for Zone 1, the zone closest to the center of the membrane. A result will also be shown for Zone 2 of the original MMDM design (MMDM A), the furthest out zone for the original type of MMDM where the distance between the edge of the membrane and the actuators is sufficiently great that the variations in this distance for different actuators is negligible. Hence, this zone is the furthest from the center for the original MMDM design for which the angular position is being claimed to be irrelevant. Finally, a result will be shown from Zone 3 of the other revised MMDM (MMDM C). This zone is the furthest from the center for the revised MMDMs, hence the argument for inclusion is the same as that for the MMDM A.

The influence functions of Zone 1 of MMDM B are shown in Figure 4.16. Two graphs are shown, the first (Figure 4.16a) shows the absolute values for the magnitude of the MMDM displacement introduced by applying 250V to the appropriate actuator. In this case, it can be seen that there is some variation in the magnitude of this displacement. There are three potential causes for this variation. The first is that the Silicon wafer supporting the membrane and the PCB supporting the actuators are not parallel, so the distance between the membrane and the actuators is not constant over the entire membrane. The second is that there may be some sort of electrical variation, from one actuator to another, for example, since each actuator has a separate amplifier, there may be some variation in the gains of each amplifier. Finally, it is possible that the electrode
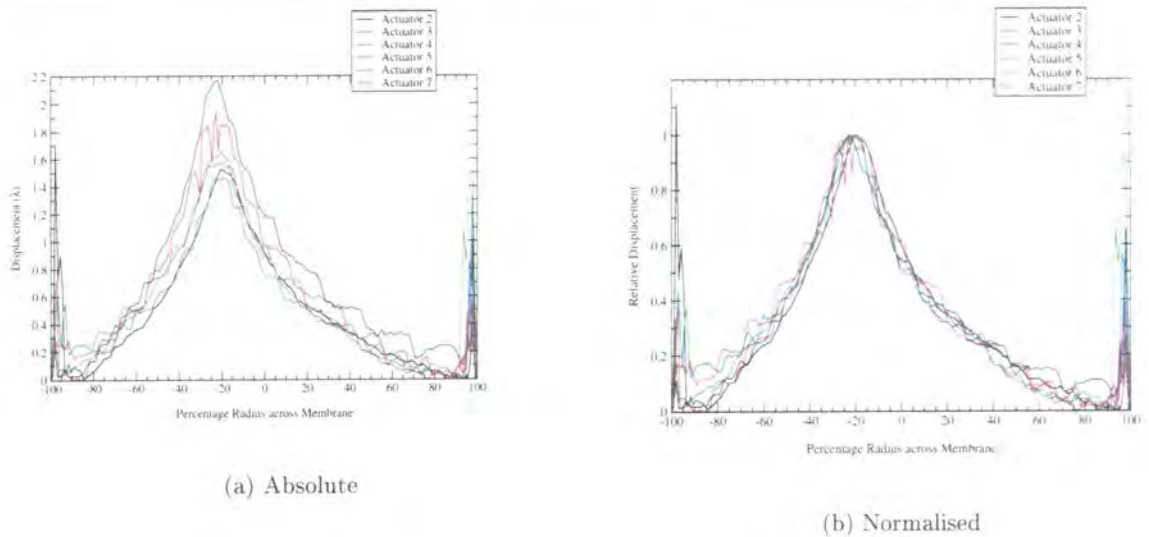
(a) Absolute

(b) Normalised

Figure 4.16: Cross section through Zone 1 actuators of MMDM B

actuators are not uniform area. These are all practical issues, so the influence functions were normalised for better comparison of the ideal performance (Figure 4.16b). As can be seen, there is an excellent agreement in the shapes of all 6 influence functions. There does appear to be a slight residual tilt in actuators 6 and 7 relative to the other actuators. This is almost certainly a slight discrepancy due to the subtraction of the reference flat.

(a) Absolute
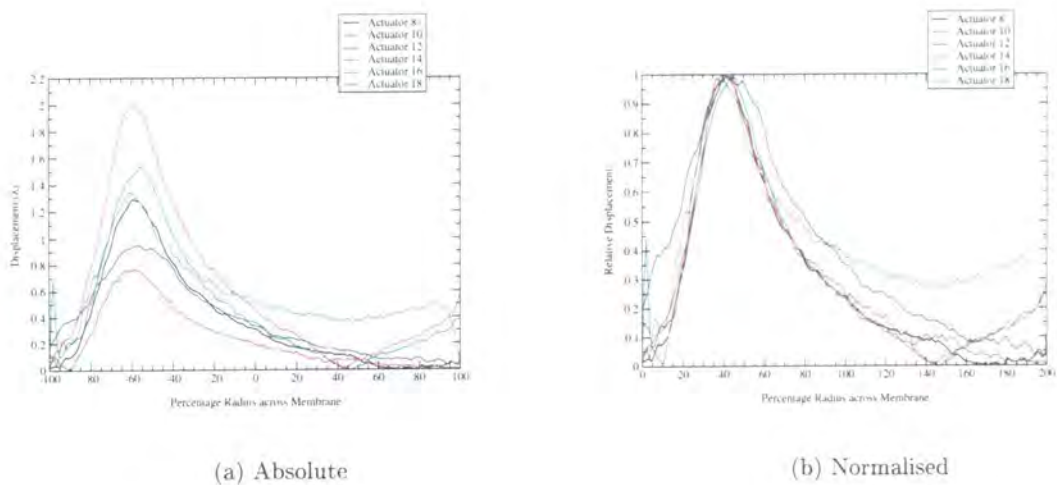
(b) Normalised

Figure 4.17: Cross section through Zone 2 actuators of MMDM A

Zone 2 of MMDM A is shown in Figure 4.17. Again, Figure 4.17a is the absolute values while Figure 4.17b is the normalised values. The variation in the MMDM displacements is greater than for Zone 1 of MMDM B. Of particular note, actuator 18 has a displacement that heads to zero at half radius in the positive direction, before increasing again. This

is due to the method of subtracting the reference, where it is the absolute difference between the reference and the data that is plotted, so it can not go negative. However, the actuators cannot push the membrane away from the unpowered membrane position, so this limit is physically realistic. In this case, it means that there must have been some error in the subtraction of the reference flat; for example, some wavefront deformations may have been introduced in the beam condenser due to thermal expansion or contraction of the mounts.

The larger variation in the magnitude of the influence functions is presumably caused by the same mechanisms as for MMDM B above. However, since MMDM A is from an earlier batch, it is likely that the manufacturing tolerances were less strict and so any tilt will be greater, as will any variation in the actuator areas. The fact that the two largest displacements occur for the two actuators opposite the two with the smallest displacements lends credence to the argument that the variation is caused by a tilt between the membrane and the actuators. Again, these are practical issues, so the normalised influence functions are also shown. Here, it can be seen that there is once again excellent agreement between the individual influence functions.

(a) Absolute

(b) Normalised
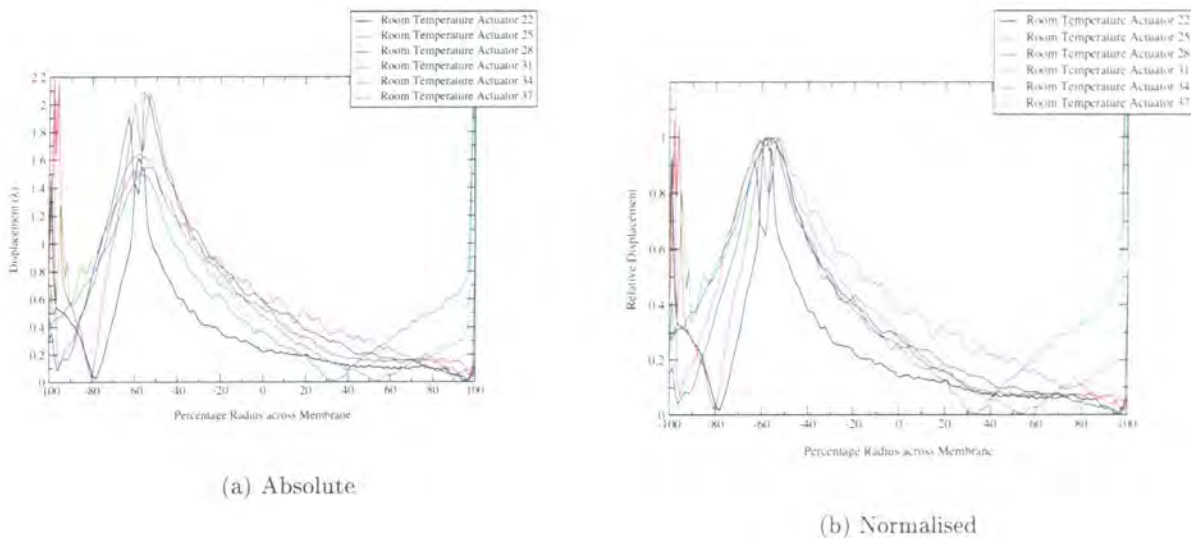
Figure 4.18: Cross section through Zone 3 actuators of MMDM C

The final set of results confirming that the rotational position of an actuator does not affect the influence function is given in Figure 4.18. These results are very similar to those given for MMDM B, even down to the range of displacements observed being similar. Another similarity is that 2 actuators have a substantially stronger signal than the remainder. However, one of the actuators involved is different. The variation in

magnitudes is again ascribed to tilt between the membrane and the actuators; again, the two actuators with the largest throw are adjacent.

The normalised results (Figure 4.18b) do show an interesting variation from the results for the other MMDMs. There appears to be a residual tilt between the influence function data and the reference data. This is shown clearly by actuator 34. Between the peak of the influence function and the membrane edge at -100% radius, this influence function is consistently higher than the other five functions. However, between the peak of the influence function and the +100% membrane edge, this influence function is consistently below the rest of the influence functions. Similar variations can be observed in the other influence functions. This can be explained by further errors in subtracting the reference data in this case. The principle justification for this explanation is that only one influence function (actuator 20) tends to zero at both boundaries. Since, physically, it is known that the membrane edge is fixed, there cannot be a variation between the reference and the influence function data at the periphery of the image.

To summarise, the angular position of an actuator around a zone does not have any significant effect on the shape of the influence funciton. However, the amplitude of the influence function does vary on a per-actuator basis. This could be due to several factors, such as the membrane being tilted relative to the actuator pad, non-uniformity of membrane thickness or non-uniform actuator area. A variation in the magnitude of the influence functions is not critical to the development of MMDMs for adaptive optics, it is easily compensated for within the control loop. Since the shapes of the functions are similar, it raises the possibility of storing four influence functions (one for each zone) and a scalar (to represent magnitude) for each actuator on the control computer, as opposed to 37 unique influence functions. This would both be simpler and lead to simpler calibration when an MMDM was replaced.

4.4.9.2 Influence Function Cross-Sections: Evacuation

There was no realistic reason to expect any significant change to the influence functions of an MMDM after evacuating the dewar. The results obtained for MMDM A are shown in Figure 4.19. As can be seen, evacuating the dewar has no affect on the influence function. Any variation between the results is clearly within the range of variation introduced by subtracting the reference data.

MMDM A has an unusual variation in the magnitude of the displacement for a given actuator voltage. Each influence function obtained for Figure 4.19 corresponds to an

actuator signal of 250V. It was expected that the zone 0 actuator would have the greatest throw, followed by zones 1, 2 and 3 in that order. This was indeed the case for MMDMs B and C. As can be seen, this trend does not hold true for MMDM A. This has to be due to some factor intrinsic to this specific device, as all other equipment used for both driving and measuring the MMDM was identical for the three MMDMs. Potential causes for this variation include a variation in the thickness of the membrane or the aluminium layer. If this is the case, then the fact that MMDM A came from a much earlier batch may be significant, particularly as MMDMs B and C did not exhibit this behaviour.

(a) Absolute

(b) Normalised
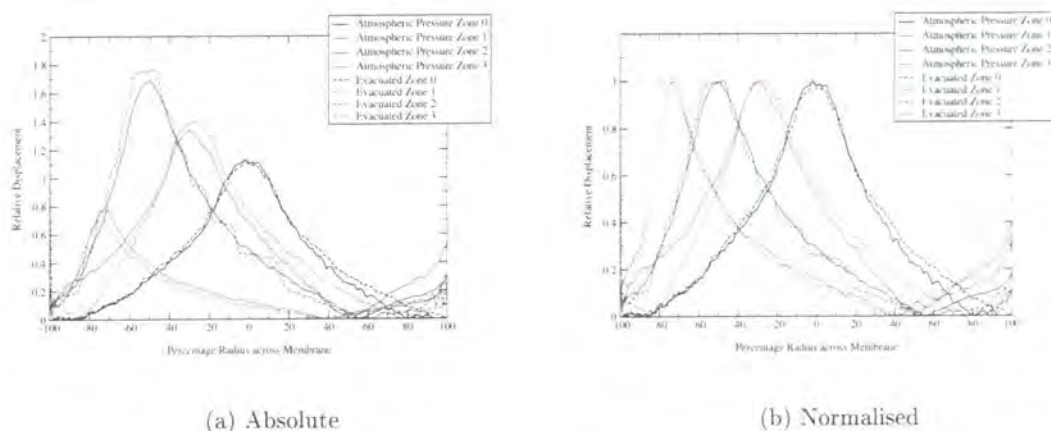
Figure 4.19: Cross section through selected influence functions at atmospheric pressure and evacuated for MMDM A at room temperature.

4.4.9.3 Influence Function Cross-Sections: Cryogenic Cooling

Having determined that the evacuation of the dewar does not affect the influence functions of an MMDM, it is necessary to determine the effect of cooling the dewar on the influence functions. Results will be presented for all 3 MMDMs.

The influence functions at room temperature and at 78K for MMDM A are shown in Figure 4.20. Given the caveats for this MMDM discussed in Section 4.4.9.2, it is necessary to be cautious about drawing conclusions from the results obtained from this MMDM. Nevertheless, it is interesting to note that the shapes of the influence functions remain very similar upon cooling, as shown by Figure 4.20b. The magnitude of the displacements is dramatically increased for actuator 35. This could be a consequence of a lateral shift between the membrane and the actuators induced by differential thermal contraction upon cooling, resulting in the actuator being further from the edge of the

membrane at 78K than at room temperature. However, this hypothesis does not explain why the displacement is increased for Zone 0 and Zone 1 actuators. It is possible that the discrepancy is due to an error in the reference file subtraction. This hypothesis is strengthened by the residual having a zero point at a radius of +20%, with a rising curve to each side. This is indicative of a negative residual being coerced into a positive signal by the algorithm used to determine the difference between the data and the reference images.

The displacement for the Zone 2 actuator, on the other hand, is reduced. A reduction in the displacement for an influence function is consistent with the results that will be shown for MMDMs B and C. To summarise the results for MMDM A, these results do not allow any clear conclusions to be drawn.

(a) Absolute   (b) Normalised
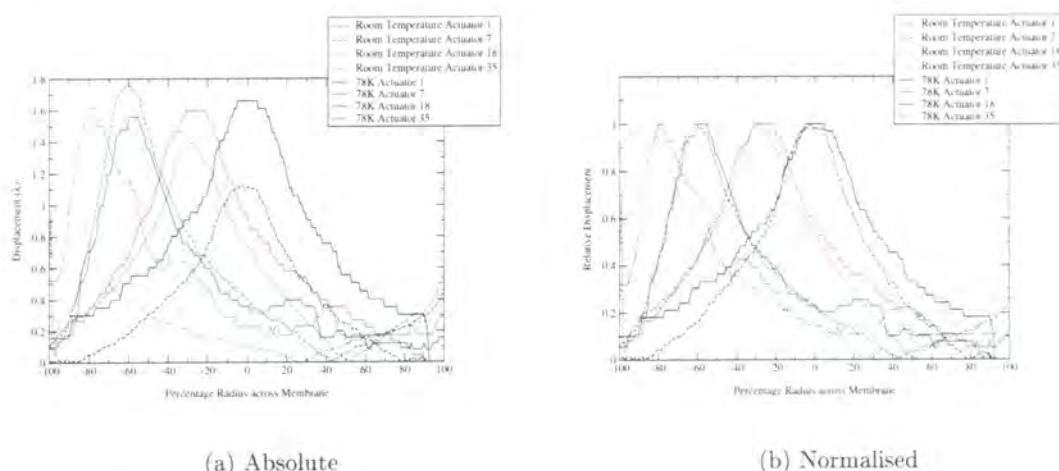
Figure 4.20: Cross section through selected influence functions at room temperature and 78K for MMDM A

The result of cooling MMDM B is shown in Figure 4.21. The apparent translation in the position of the influence function is due to either the deformations introduced to the membrane surface by cooling, or by the methods used to undo these deformations to enable comparisons to be done with the room temperature results. This may also be an explanation for the apparent narrowing of the influence functions. In this case, however, there is a clear trend with regard to the magnitude of the influence functions. The cold influence functions are consistently reduced in comparison with the room temperature influence functions. The exception is for the outermost actuator, 35, which appears to have a plateau artefact from a poor reference subtraction. The scale of the magnitude reductions is given in Table 4.4, and indicate a reduction in the throw for a given actuator of approximately 15%.
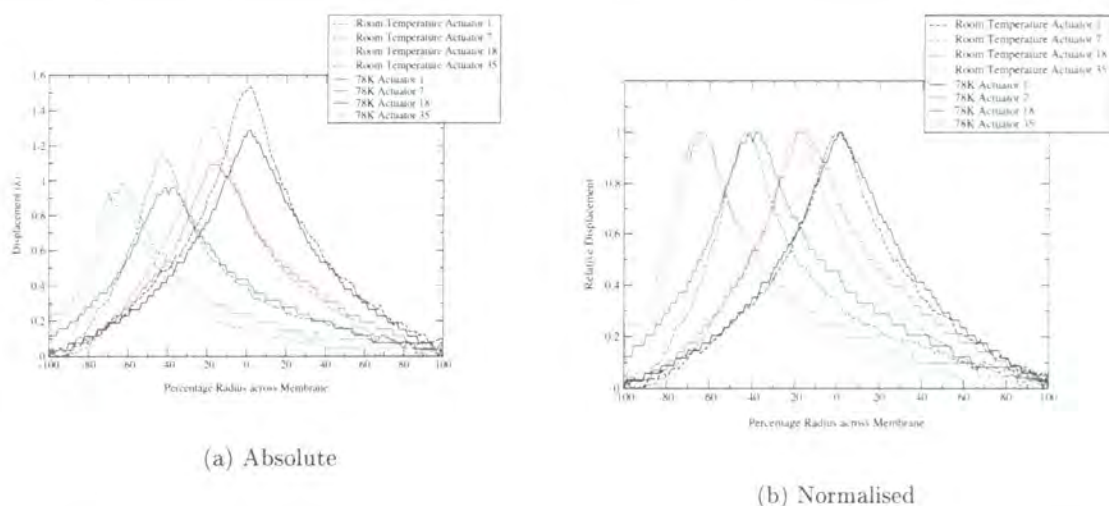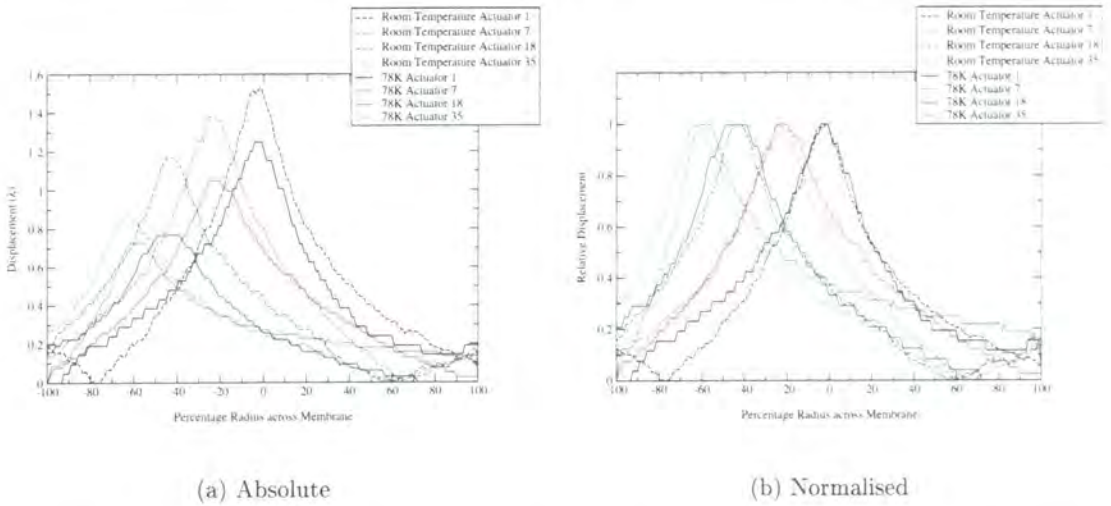
(a) Absolute

(b) Normalised

Figure 4.21: Cross section through selected influence functions at room temperature and
78K for MMDM B

Actuator	295K P-V displacement (λ)	78K P-V displacement (λ)	78K displacement relative to 295K displacement
1	1.53	1.29	84%
7	1.31	1.09	83%
18	1.14	0.96	84%
35	0.87	0.98	112%

Table 4.4: Peak to Valley displacements for selected actuators of MMDM B

Similar results are found for MMDM C, as shown in Figure 4.22. Again, the peak to
valley displacements are tabulated, in Table 4.5. This time, though, there is more of a
scatter in the change in displacements, resulting in an average reduction of $23 \pm 3.5\%$.
The main difference between the results for MMDM C and MMDM B is that there is
much less translation between the room temperature and the 78K results in the case of
MMDM C. The large spikes in both sets of results are a consequence of diffraction effects.

To summarise the cold results, two MMDMs (B and C) have been shown to have
influence functions at 78K which are similar to those at room temperatures, albeit reduced
in magnitude by approximately 20%. For the MMDM A, the results are less consistent.
Again, the influence functions have a good shape agreement with the room temperature
results, but the magnitude of the functions is less certain.

(a) Absolute   (b) Normalised

Figure 4.22: Cross section through selected influence functions at room temperature and 78K for MMDM C

Actuator	295K P-V displacement (λ)	78K P-V displacement (λ)	78K displacement relative to 295K displacement
1	1.53	1.25	82%
7	1.39	1.05	76%
18	1.17	0.77	66%
35	0.87	0.73	84%

Table 4.5: Peak to Valley displacements for selected actuators of MMDM C

4.4.10 Conclusions

In this chapter, a method to measure the static properties of a deformable optical element using a Zygo PTI interferometer has been described. This method has then been applied to a sample of three MMDMs at room temperature and at 78K. The analysis method for these results has been described. The results have been presented in several ways. Initial surface deformations have been quantified in terms of Seidel aberrations and presented as false colour phase maps. The influence functions have then been analysed. The influence function for each actuator is shown as a false coloured phase map at room temperature and at 78K. Finally, some cross-sections through these influence functions were presented.

Cooling the MMDMs has been shown to introduce large initial surface deformations, of about 10λ for MMDMs B and C, and 6λ for the remaining MMDM, A. MMDM A was from

a separate batch to MMDMs B and C, which opens up the possibility of manufacturing parameters for the MMDMs, such as membrane thickness, to be optimised for cryogenic operation. All of the MMDMs used in this project were intended for room temperature operation, and were therefore optimised for such operation. In the case of MMDM A, the initial surface deformations are sufficiently small to leave a substantial fraction of the 18 λ dynamic range free for wavefront correction. The exact dynamic range available for correction is dependent on the diameter of the beam being used. It has also been shown that two of the MMDMs, B and C, have influence functions at 78K that are very similar to those at room temperature, although the influence functions are reduced in scale by about 20%. MMDM A has influence functions at 78K which are very similar in shape to those at room temperature, but the change in magnitude is unpredictable.

These results are the first experimental evidence for an adaptive optical element that functions at cryogenic temperatures.

Chapter 5

Dynamic Characterisation of Micro-Machined Membrane Deformable Mirrors

5.1 Introduction

In this chapter, the dynamic properties of three MMDMs are examined at room temperature and at 78K. This evaluation is necessary to determine where MMDMs may be deployed as wavefront correctors at cryogenic temperatures. In particular, it will be shown that the MMDMs operate at sufficiently high frequencies to be suitable for both active and adaptive optics. Specifically, the operating bandwidth of the MMDMs will be compared to that required for atmospheric correction (Greenwood 1977). Further, the quoted maximum frequency of operation of 1kHz will be indirectly investigated (Vdovin and Sarro 1995).

The set up used was similar to that used for the static measurements (Chapter 4), with minimal alterations. A beam splitter was utilised to pick off part of the reflected beam which was re-directed to a photodiode (see Figure 5.1). The first tests to be conducted determined the effect on the MMDMs dynamic characteristics of evacuating the dewar. This effect is characterised in three ways: by presenting a plot of photodiode response against time for a subset of the results; by examining the statistics of the signal; and finally by examining the power spectra of the photodiode signal. A similar scheme is then implemented to examine the effects on the MMDM of cooling the dewar. Finally, a brief discussion is undertaken outlining a potential methodology for improving the MMDMs

dynamic performance at 78K.

5.2   Set-up

The set up for measuring the dynamic properties of the MMDMs was necessarily different from the set up for the static testing. Every effort was made to ensure that as much of the set up as possible was common between the two sets of experiments. The optical arrangement was as shown in Figure 5.1
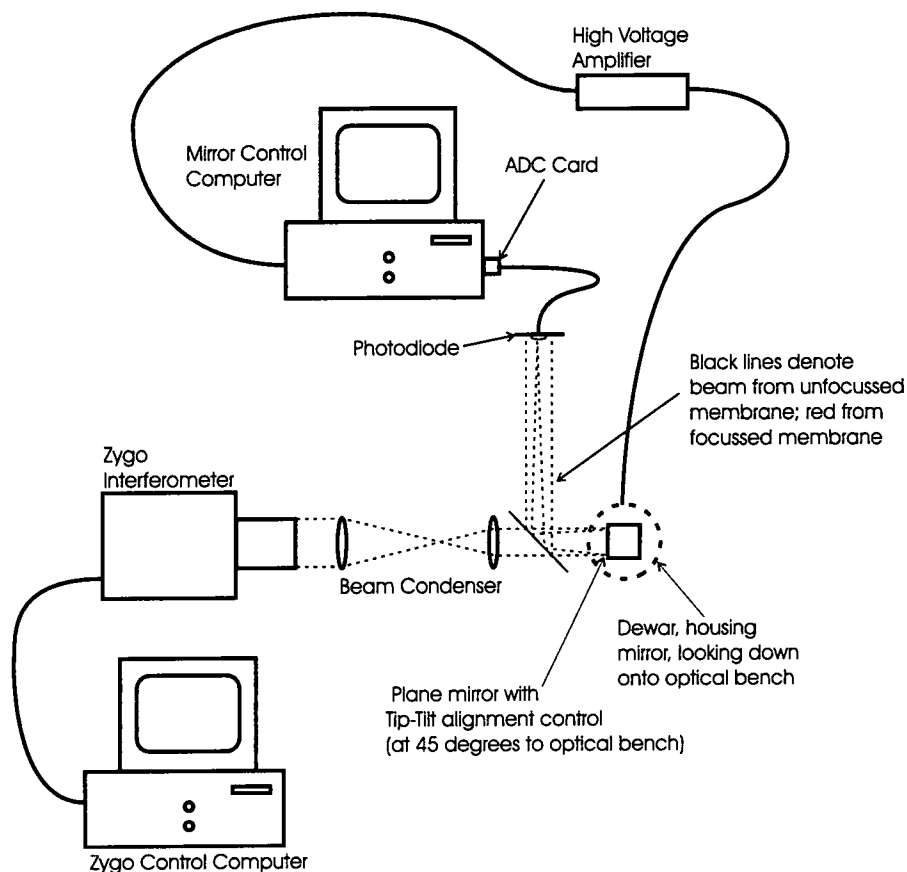
Figure 5.1: The bench set-up for the dynamic charecterisation measurements
The control signal is a square wave of the frequency being examined. This drives the membrane surface to oscillate at the same frequency. The reflected beam is thus focussed to two different positions, changing the photodiode signal with time.

Although the Zygo PTI interferometer is again installed in this set-up, the anticipated dynamic response times of the MMDM were too fast to be captured by the camera within the Zygo. Hence, the Zygo PTI was being used in this phase of the experiments purely as a light source. The beam reflected from the MMDM surface was re-directed towards

a photodiode by use of a beam splitter. The photodiode was positioned near the focus of the MMDM when 180V was applied to all actuators. Hence, by switching between two different voltages, the membrane surface could be moved, changing the focal distance of the MMDM. Therefore, the amount of light intercepted by the photodiode could be changed, and a time-varying signal could be obtained. The IPL10530DAW photodiode had a frequency response of 65kHz, while the Computer Boards PCI-DAS08Jr ADC card in the computer had a quoted maximum frequency of 20kHz (*Farnell Catalogue* 1999, ComputerBoards Inc. 1999). In practise, 20kHz was found to be unreliable, so the card was run at a more reliable 10kHz. Hence, the Nyquist frequency was 5kHz, and this rapid response time was the reason for utilising the photodiode rather than a camera for the dynamic testing measurements.

5.2.1   Electronics

The electronics used to power the MMDMs in the original set up were essentially as supplied with the MMDMs. Digital to analogue converters installed within the PC controlled a 20-channel amplifier board with a signal of 0-5V. The gain of the amplifier was 53, so the output from the amplifier was in the range of 0-265V. 19 channels from the amplifier were then connected to the MMDM actuators. This electronics set-up has remained fundamentally unchanged for the duration of this project; the only major alterations prior to the initiation of the dynamic testing were to duplicate the system to drive the extra channels in the 37 channel MMDM; and the installation of a high voltage monitor to allow the temporal behaviour of the electronics to be assessed.

One further alteration was made for the purposes of the dynamic testing. In these experiments, the specific dynamic response of interest was not that of the electronics but of the membrane. After all, were the electronics to be the limiting factor in the reaction time of the membrane, they could always be upgraded. Hence, it was decided to modify the electronics so that a single channel from the digital to analogue converter card was connected to the first 19 amplifier channels. In this way, the delay introduced by setting these channels sequentially was eliminated. A sufficient signal was obtained from driving the 19 central actuators that it was deemed to be unnecessary to drive the zone 3 actuators for these experiments.

The high voltage amplifiers were provided by OKO technologies with the MMDMs, and remained unaltered for the duration of this work (Vdovin 2001b). There were 20 amplifiers on each card, with a jumper on each card to short one of the channels to

Earth. This was done in the case of the first card to ground the membrane channel. This left 19 channels on the first card, which were used to drive actuators 1 to 19; 20 to 37 were driven from the second card with two amplifier channels spare. The dynamic performance of the electronics was also an issue. Presented in Figure 5.2 is the signal measured after the high voltage amplifiers for a voltage change of 0V to 180V and back. It should be noted that the rise time is voltage dependent, while the fall time is not.
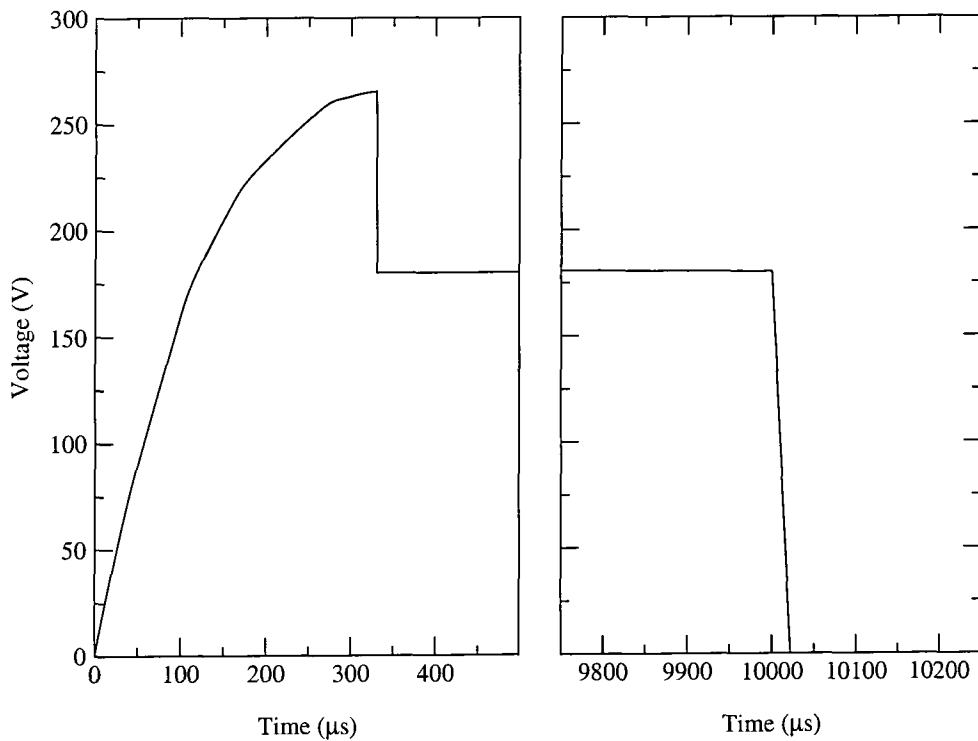
Figure 5.2: Dynamic response of the electronics

The voltage overshoot present in the rising signal is a consequence of the design of the electronic circuit. As will be seen in the dynamic testing results, this overshoot is present in the membrane motion (see Section 5.4).

5.3   Software

The requirements for the MMDM control software for the dynamic testing were very similar to that for the static testing. The differences have been highlighted in the psuedo-

```
Set all MMDM channels to 0V

Remind user of the safe switch on procedure for the MMDM power supplies

LOOP

    Read controls for actuator start and finish voltages and number of iterations

    Check which actuators have either voltage altered from previous end voltage

        FOR number of iterations

        IF actuator start signal outside safe range, coerce into safe range

        Apply each new actuator start voltage

        Wait for delay

        IF actuator end signal outside safe range, coerce into safe range

        Apply each new actuator end voltage

        Wait for delay

    NEXT iteration

UNTIL user stops program

Remind user of the safe switch off procedure for the MMDM power supplies
```

Table 5.1: Pseudo-code Algorithm for MMDM control software for dynamic testing.

code algorithm in Table 5.1 with italics:

As can be seen, if the delay is set to zero and only the end voltages are altered, this software is functionally identical to the static control software. Hence, the dynamic control software was used for both tasks.

A limitation of this software, and indeed of LabVIEW, is that the delay has to be an integer number of milliseconds. Therefore, only certain signal frequencies could be studied, for example, 500Hz when delay was set to 1ms. After a given run, these samples were then saved to disc.

5.4   Results

The dynamic testing undertaken was intended to answer specific questions, in a similar manner to the static testing results. The first aspect to be investigated was the effect of evacuating the dewar on the response time of the membrane. Unlike the case for the static testing, it was anticipated that there would be some change in the dynamic response due

to evacuation, since it is accepted that the response time is limited by air damping of the membrane in conventional operation of the MMDM. Secondly, the effect of cooling the MMDMs on the dynamic response of the membrane will be investigated.

The results are presented in two forms. First, graphs will be shown of a small subset of each 1 second long measurement, showing about two complete cycles of the signal. After this has been done for each question being examined, statistics and power spectra over the whole measurement will be presented.

5.4.1 Evacuation

5.4.1.1 Photodiode Response
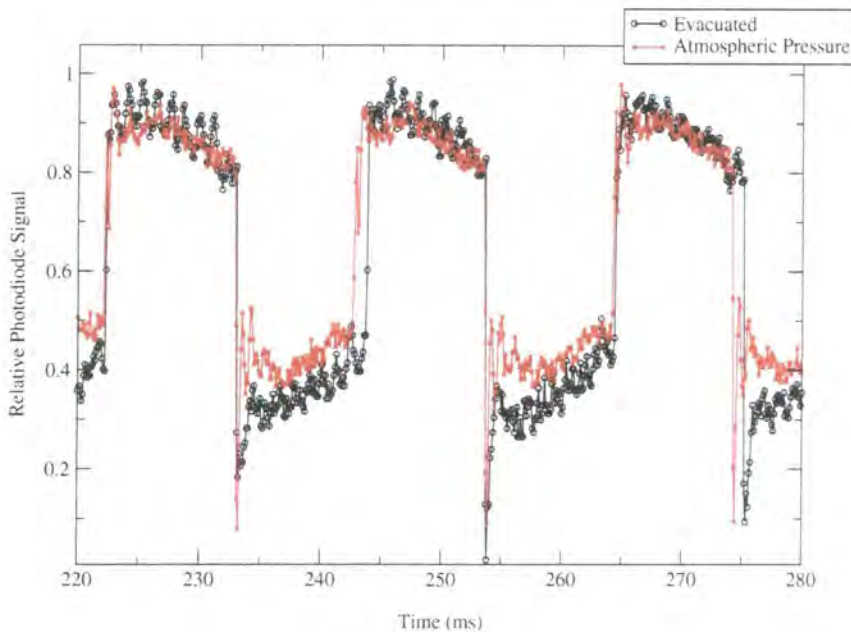
Figure 5.3: Comparison of evacuated and atmospheric pressure MMDM dynamic responses for MMDM A driven at 50Hz

Figure 5.3 shows the measured photodiode signal from driving MMDM A from 0V to 180V at 50Hz for the MMDM at atmospheric pressure and evacuated to 1×10^{-4}mbar. It was expected that the membrane would behave differently at lower pressures, since the membrane is subject to air damping from the air gap beween the membrane and the actuator pad, see Figure 2.7 (Vdovin and Sarro 1995). However, it is clear that there is little effect from evacuating the dewar in the measured dynamic response. Since the

sample time is at least comparable to the rise time, it is possible that the evacuation is having an effect on a shorter timescale.

The reason for plotting the relative Photodiode signal, rather than the absolute signal, is that the Zygo laser is not intensity stabilised (since the Zygo PTI is a phase-shifting interferometer, it is intensity independent, hence the laser does not need to be intensity stabilised for normal operation). Therefore, each set of data has been translated so that the minimum signal is at 0, and scaled so that the maximum is at 1. It is clear from the graph that there is an overshoot when the control signal goes from 180V to 0V. This causes the re-scaling to introduce a slight DC offset in the photodiode signal for the 0V control signal, for example, between 254ms and 265ms. One further point to note is that the duty cycle is clearly not 50%, as evidenced by the synchronicity of the falls of the two signals at 233ms and the subsequent asynchronicity in the corresponding rises at 245ms. There are subsequent variations at 275ms. Other data also shows similar patterns. This is a consequence of the use of MS Windows 95 as an operating system, rather than using a real time operating system. The dynamic testing was conducted under Windows 95 rather than NT for speed reasons; however, NT is also not a real-time operating system, so the same problem would have occurred. The main reason for not using a real-time operating system was the additional complexity inherent in such a system, to solve a relatively minor problem. It will be see in the power spectra (see Section 5.4.1.3) that the effect of these slight timing errors are not significant.

Examining the results for MMDM B, see Figure 5.4, again shows little difference between the atmospheric pressure and evacuated results. These results were taken for a driving frequency of 100Hz. There appears to be a little more noise in the measurements for the evacuated results than for the atmospheric pressure results. This is due to the results having been taken when the Zygo laser was less intense, and so the signal was a factor of 4 weaker than for the atmospheric pressure results. Hence, when the results are re-scaled, the noise is also amplified, so the signal to noise ratio is lower. An intensity stabilised laser was not considered for two reasons; firstly, it would have required more substantial alterations to the optical set-up, and secondly, the cost of an intensity stabilisied laser was a substantial deterrent. Nevertheless, the signal is still much stronger than the noise, so the results are still significant, in other words, the signal to noise level was still acceptable. Again the rise and fall times are comparable or less than the sample time.

Driving MMDM C at 250Hz produces the results shown in Figure 5.5. Here, the effect
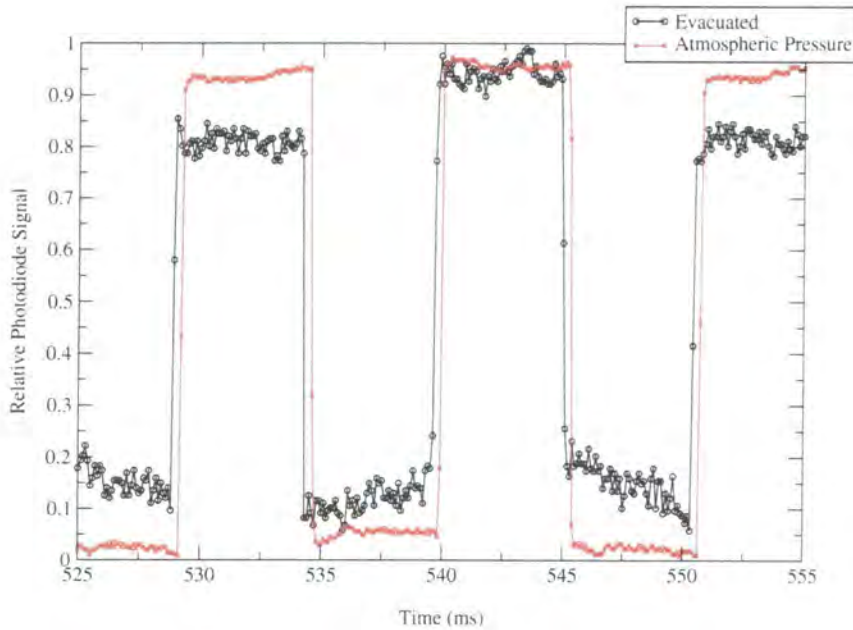
Figure 5.4: Comparison of evacuated and atmospheric pressure MMDM dynamic responses for MMDM B driven at 100Hz

of not having a duty cycle of 50% is again apparent. However, what is more interesting is that the MMDM appears to act as a damped simple harmonic oscillator after each change in position. Figure 5.6 shows the detail of the previous results, on the same scale as Figure 5.5. Here, it can be seen that the damped oscillations also appear to occur for MMDM A, but not for MMDM B. In the case of the signal for MMDM B at atmospheric pressure, the absolute photodiode signal was close to the largest measurable signal, but saturation does not account for the lack of oscillations, as can be seen by the absence of oscillations in the 'off' signal. It would appear that either MMDM B does not exhibit the same oscillations as A and C, or that the oscillations were too rapid for the photodiode to detect. However, Figure 5.7 shows a detail from the results obtained at 50Hz for MMDM B, and shows the membrane overshooting, with oscillations for at least the evacuated case. However, the oscillations are more rapid. This suggests that the oscillations may still be present in the other results, but are just too rapid to be detected by the experimental set up.

In the case of MMDM C, the evacuated results indicate that the oscillations are more rapid and decay quicker than for the atmospheric results. This is unexpected, since the absence of air from both sides of the membrane should result in a smaller, rather than
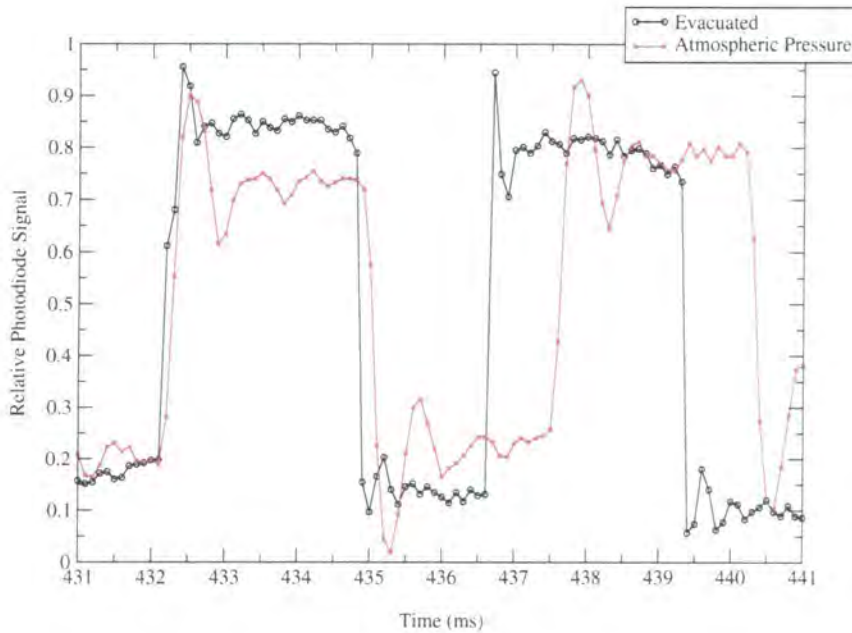
Figure 5.5: Comparison of evacuated and atmospheric pressure MMDM dynamic responses for MMDM C driven at 250Hz

larger, damping force. Every effort was made to ensure that the circumstances for the two measurements were identical. Despite this, the dewar had to be removed from the system to be evacuated, before the system was re-aligned. However, everything else within experimental control was kept constant, for example, the MMDM was simply left in the socket from the atmospheric measurement to the evacuated measurement. A potential explanation could be a slight temperature variation between the two measurements, causing a change in the membrane tension.

A final set of results examining the effect of evacuating the dewar is shown in Figure 5.8. These results were again taken with MMDM A, but this time at 500Hz. No speeds between 500Hz and 250Hz were available due to the limitation of having an integer number of milliseconds between control signal changes. These results are much noisier than the previous results. This would be indicative of the membrane never achieving a stable position, but for the signal to change before it has reached equilibrium, hence resulting in a smaller signal, and therefore a lower signal to noise ratio. It is also clear that the duty cycle is straying further from 50%, hence suggesting that the computer is being worked harder to drive the contol electronics at these speeds. This suggests that, rather than the membrane not reaching equilibrium in each cycle, it may be that the computer
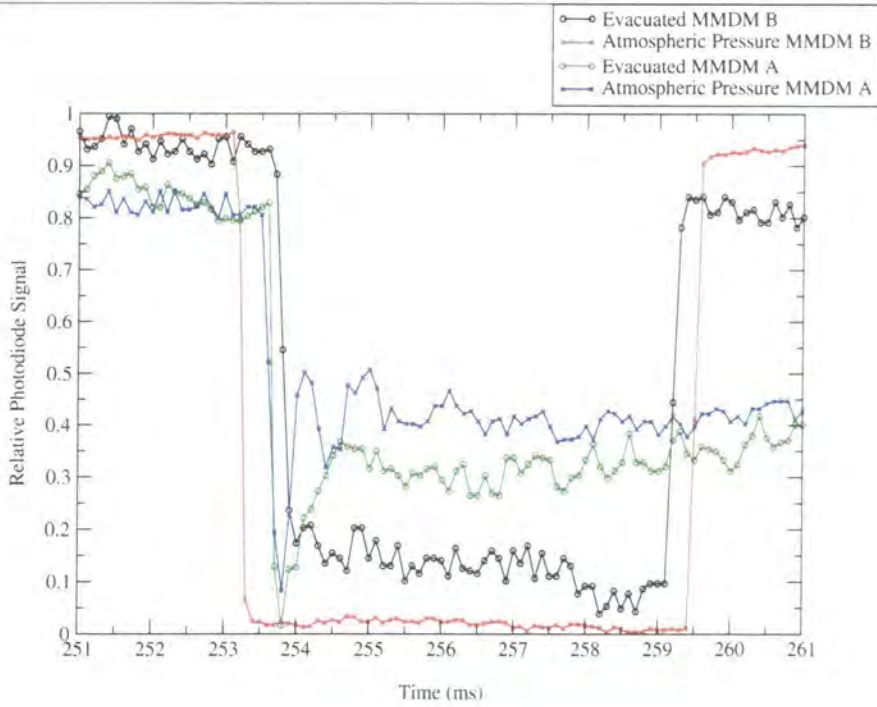
Figure 5.6: Comparison of evacuated and atmospheric pressure MMDM dynamic responses: detail of figures 5.3 and 5.4

is limiting the performance of the MMDM in this case. It also may be possible that the electronics may be responsible. This will be discussed further after examining the power spectra in Section 5.4.1.3.
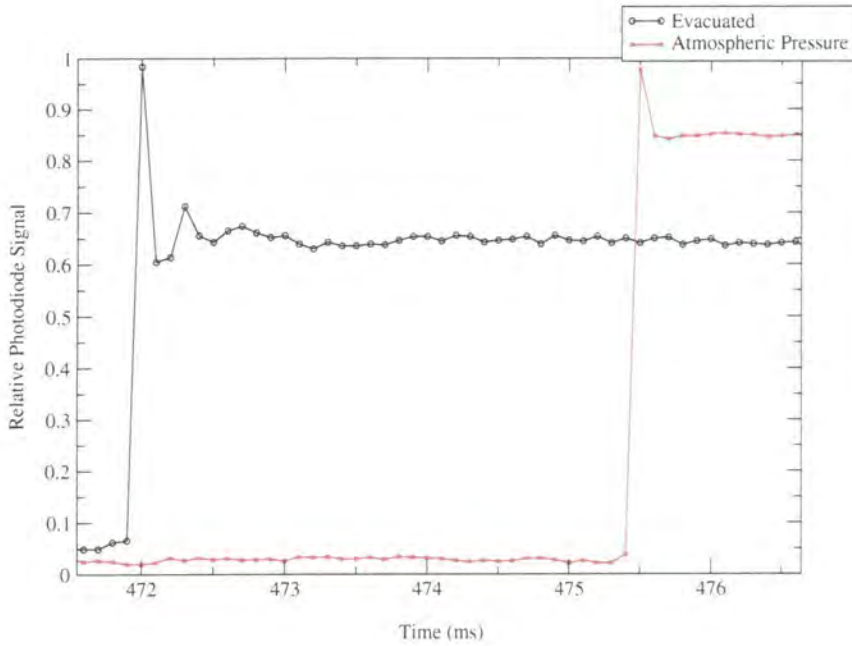
Figure 5.7: Comparison of evacuated and atmospheric pressure MMDM dynamic responses: detail of overshoot for MMDM B
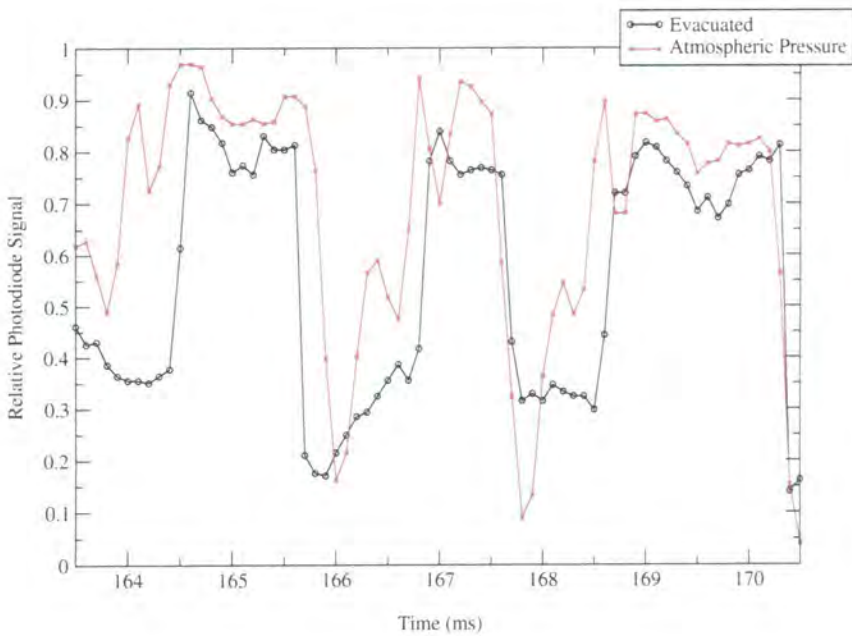
Figure 5.8: Comparison of evacuated and atmospheric pressure MMDM dynamic responses for MMDM A driven at 500Hz

5.4.1.2 Statistics

It is interesting to examine a few statistics of the preceding results. For the purposes of the following statistics, each graph was split into two section, one of all the data points above the average relative photodiode signal (the Upper population), and the other of the remaining data points below this average (the Lower population). Statistical summaries of these two populations are provided in Table 5.2. In the case of the two revised MMDMs, B and C, it is clear that the standard deviation, and hence the random noise, is similar for both the upper and the lower populations. It is equally clear that this is also the case for the original MMDM, A, but only at 50Hz. Where this MMDM is being driven at 500Hz, a discrepancy arises between the noise present in the upper population and the lower population, with the upper population having a standard deviation about half of that for the lower population. This is a consequence of the large overshoot present each time that the membrane goes from the upper population to the lower population.

Evacuating the dewar does not have an appreciable affect on the standard deviation of the two populations. This means that the damping force in the system is significantly less than the restoring force from the membrane tension. Elsewhere, it has been hypothesised that air damping is the limiting factor in the dynamic response of MMDMs (see, for example, (Vdovin and Sarro 1995)). This may be the case for frequencies higher than those being examined here, but is not the case for frequencies up to 500Hz.

MMDM	Environment	Driving Frequency (Hz)	Population	N	Mean	Standard Deviation	Figure
A	Evacuated	500	Upper	4944	0.856	0.0676	
A	Evacuated	500	Lower	5056	0.379	0.105	5.8
A	Atmosphere	500	Upper	4966	0.840	0.0775	
A	Atmosphere	500	Lower	5034	0.464	0.172	
C	Evacuated	250	Upper	4963	0.783	0.0944	
C	Evacuated	250	Lower	5037	0.130	0.0743	5.5
C	Atmosphere	250	Upper	5020	0.772	0.0821	
C	Atmosphere	250	Lower	4980	0.238	0.0844	
B	Evacuated	100	Upper	4927	0.870	0.0627	
B	Evacuated	100	Lower	5074	0.140	0.0624	5.4
B	Atmosphere	100	Upper	4986	0.950	0.0378	
B	Atmosphere	100	Lower	5015	0.0351	0.0419	
A	Evacuated	50	Upper	5108	0.786	0.0608	
A	Evacuated	50	Lower	4892	0.335	0.0748	5.3
A	Atmosphere	50	Upper	5311	0.814	0.0838	
A	Atmosphere	50	Lower	4689	0.403	0.0857	

Table 5.2: Evaluation of MMDM dynamic response: evacuated and atmospheric pressure
Evaluation of MMDM dynamic response: evacuated and atmospheric pressure. 'Upper'
population is defined as all data points above the mean of the 10,000 points in each total
sample, 'Lower' population is the remaining points. N denotes the number of data points
in the sample.

5.4.1.3 Power Spectra

The power spectra for both the preceding MMDM measurements and other MMDM mea-
surements are presented here. These were obtained by subtracting the average photodiode
response from each data point and applying a fourier transform to the resultant. These
fourier transforms were then normalised so that the largest peak has a value of 1. Since
the laser intensity did vary with time, there was no absolute power information contained
within the data; everything was relative. Hence, nothing was lost by scaling the fourier

transforms. Instead, the distribution of the power to the different frequencies was of interest.
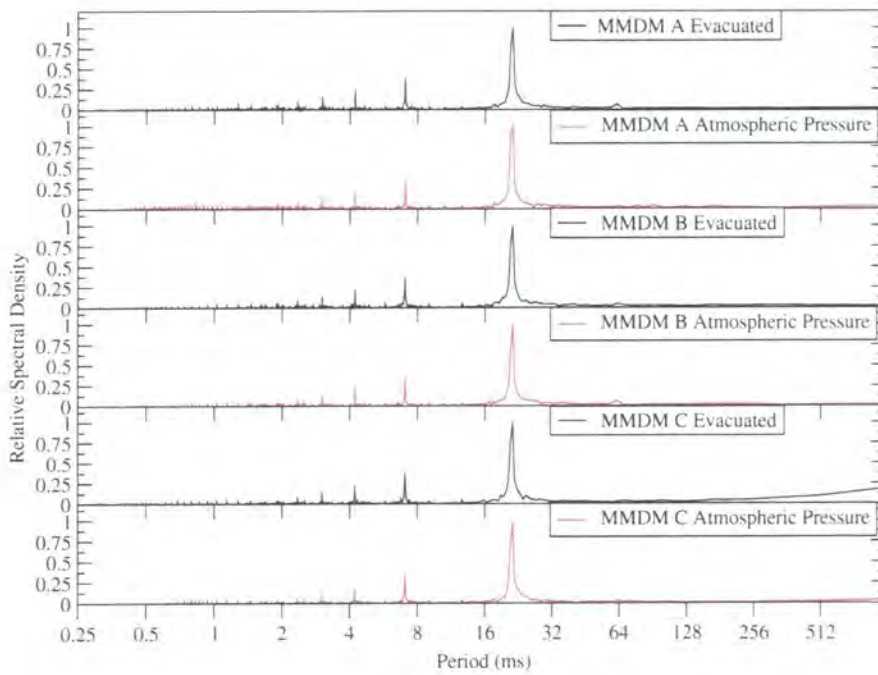
Figure 5.9: Power spectra for driving each MMDM at 50Hz

Figure 5.9 shows the power spectra obtained for each MMDM when driven at 50Hz. corresponding to a period of 20ms. The first thing to notice is that there is no noticeable difference between the results obtained with or without evacuating the dewar. This similarity was the reason for presenting each case as a separate graph; presenting both the evacuated and atmospheric pressure results in the same graph led to one set of data being obscured by the other. It is also apparent that there is little variation from one MMDM to another. Since it is known that MMDM A is from a different batch to the other MMDMs, and that there is sufficient difference between A and the other MMDMs to cause a substantial variation in the static properties, this is perhaps surprising.

The graphs consistently show a strong peak at a period of 21ms, which is the driving frequency (for a nominal period of 20ms, plus about 1ms for system overhead and electronic delays). There are also some higher frequency components present in the data. resulting in spikes at shorter periods. These higher frequencies are the harmonics of the membrane system. It should be noted that the frequencies of these harmonics do not match those expected from a circular membrane, with edge boundary conditions, as summarised in Table 5.3. In the table, the predicted harmonics come from Bessel func-

tions (Soedel 1981). The literature provides examples of real drums posessing harmonics that do not fit with the predicted results, see for example, White and White (1980). In the MMDMs' case, though, the discrepancies from the predictions are quite large. However, the frequency multiples observed are consistent with a one dimensional oscillator fixed at one end. It is conjectured that the edges of the membrane have the effect of splitting the membrane into a finite number of 1-D oscillators, with the boundary edge fixed and the central point of the membrane being the driven free end, as per Figure 5.10. In the real MMDM, there are far more crenellations, so the length of each oscillator would be much greater than its width, indicating that each oscillator could be considered to be 1 dimensional. This relies on the oscillators being independent.

Harmonic	Period (ms)	Predicted Period (ms)	Frequency (multiples of fundamental)	Predicted frequency (multiples of fundamental)
Fundamental	21.275	21.275	1	1
2nd	7.042	6.65	3.02	3.196
3rd	4.219	3.37	5.04	6.306
4th	3.012	2.25	7.06	9.440

Table 5.3: Measured and predicted harmonics for membrane
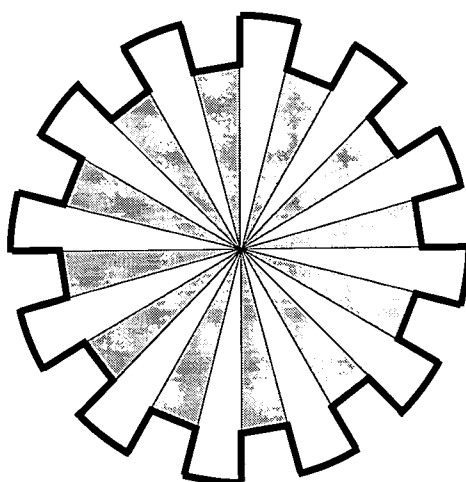
Figure 5.10: Illustration of finite number of strings model for MMDM harmonics

For a driving frequency of 250Hz, the results shown in figure 5.11 are obtained. Two other peaks are observed at lower frequencies, specifically 100Hz (period of 10ms) and
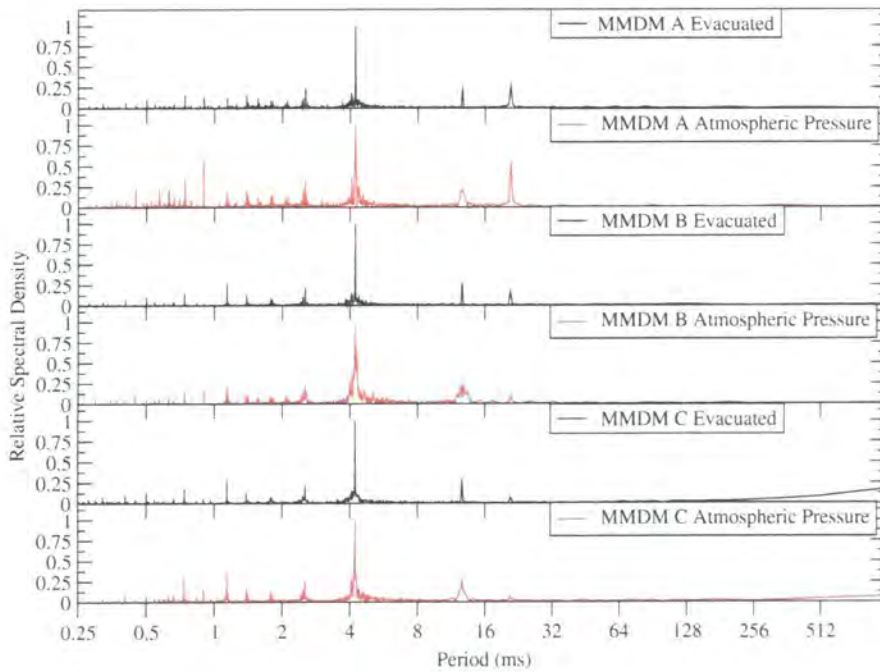
Figure 5.11: Power spectra for driving each MMDM at 250Hz

50Hz (period of 20ms). The 50Hz signal is electrical noise picked up somewhere in the
computer, photodiode and analogue to digital converter system. The 100Hz signal is
similar noise picked up from flourescent strip lights used in the rooms surrounding the
laboratory where these results were obtained. In the case of MMDMs B and C, the same
harmonic pattern is present as for the 50Hz results. In the case of MMDM A, these peaks
are still present, but there are also many other peaks, particularly in the atmospheric
pressure results. It is worth noting that the harmonics are another method to probe
the effect of air damping on the membrane. In particular, the lack of air damping does
not yield a stronger signal for the 1.25kHz peak (0.8ms period) spike in the case of the
evacuated results. This indicates that the effect of air damping, rather than being the
limiting factor in the response time of the MMDMs, is insignificant to frequencies above
the nominal maximum MMDM frequencies (Vdovin and Sarro 1995).

The results shown in Figure 5.12 were obtained for a driving frequency of 500Hz. It is
clear that the MMDM is not suitable for operation as a wavefront corrector at this speed
using the current hardware. It is believed that the cause of the multiple peaks obtained
in this set up is the control hardware, either at the electronics or at the computer. In the
case of the electronics, the units supplied with the MMDMs were used; no effort was made
to re-design the electronics for high speed operation. The computer used was similarly
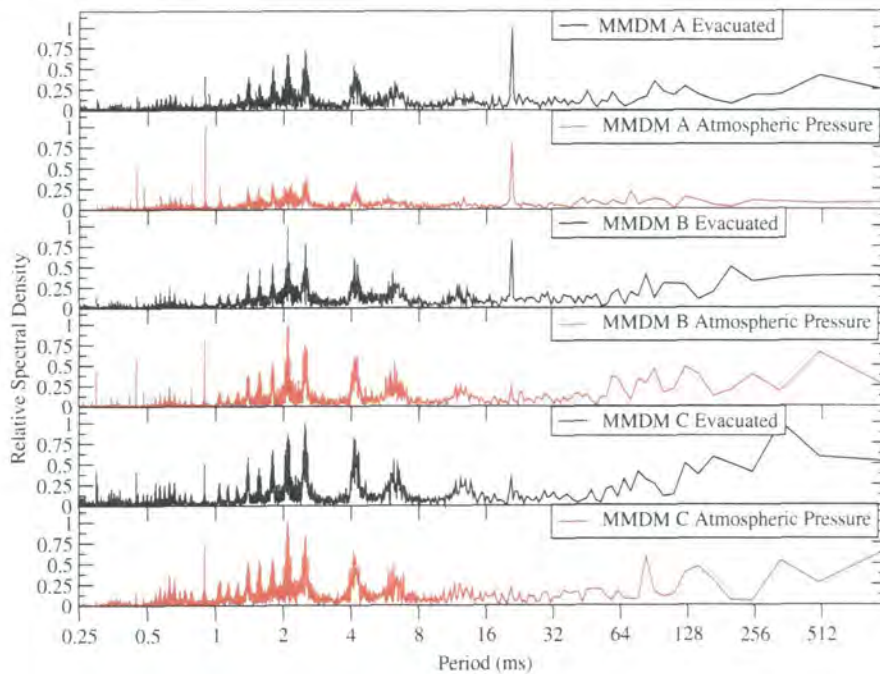
Figure 5.12: Power spectra for driving each MMDM at 500Hz

an off the shelf PC using a non-real time operating system.

However, of most interest when considering the mechanics of the MMDMs is that evacuating the dewar has not improved the high frequency performance of the membrane. Indeed, the presence of air in the atmospheric pressure results appears to amplify certain high frequency components above the accepted maximum frequency of 1kHz (Vdovin and Sarro 1995), such as the peak at a period of 0.9ms, corresponding to 1.1kHz. For frequencies below 1kHz, there is no effect on the membrane's frequency response from evacuating the dewar. Above this threshold frequency, the evacuated response appear to be marginally reduced compared to the response with air present. However, even in this regime, the effect is small.

5.4.2 Cryogenic Temperatures

Having established that evacuating the dewar does not affect the MMDMs dynamic response, it is now necessary to examine this response at 78K. This will be done by following the same methodology as for the previous room temperature results.
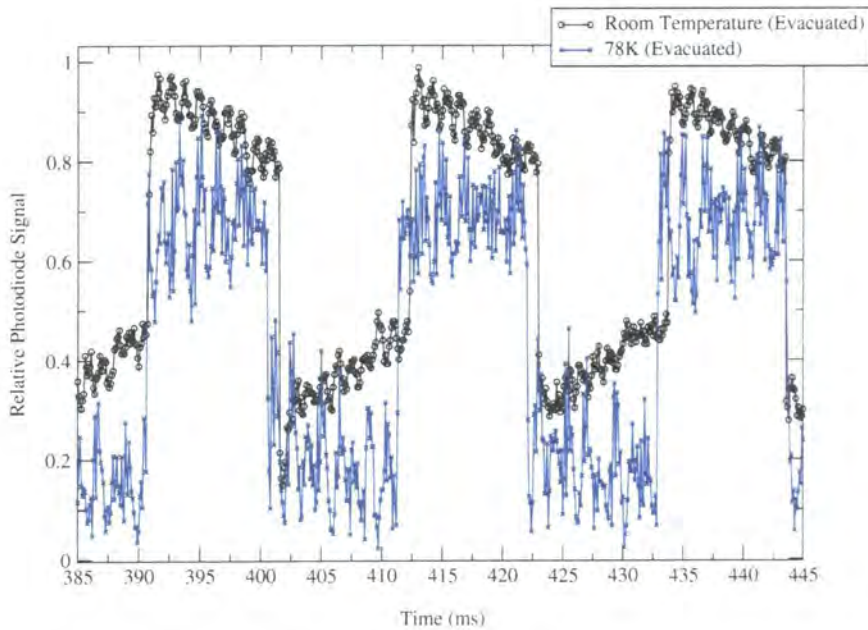
Figure 5.13: Comparison of room temperature and 78K MMDM dynamic responses for
MMDM A driven at 50Hz

5.4.2.1 Photodiode Response

Figure 5.13 shows a 60ms subset of the results obtained for MMDM A at 78K being
driven at 50Hz. It is clear that the driving signal does not have a 50% duty cycle, as was
discovered for the room temperature results. More interesting is that the signal is much
noisier; the membrane appears to be continually oscillating at a high frequency (1kHz).
This is swamping the 50Hz variation clearly visible as the dominant source of noise in
the room temperature results. It is also important that the rise and fall time of the cold
results is again comparable to or quicker than the Nyquist time of the measurements
(0.2ms).

The 78K results for MMDM B being driven at 100Hz are shown in Figure 5.14. There
is again a very clear high frequency oscillation in the signal, indicative of oscillations of
a frequency higher than 1kHz. Verification with an oscilloscope indicates that the high
frequency signal is in the region of 6.5kHz, so the results shown here are being aliased by
the measurement apparatus. Again, the rise and fall times seem to be of the order of the
Nyquist time, at most.

The signal to noise ratio for the measurements of the dynamic response of MMDM
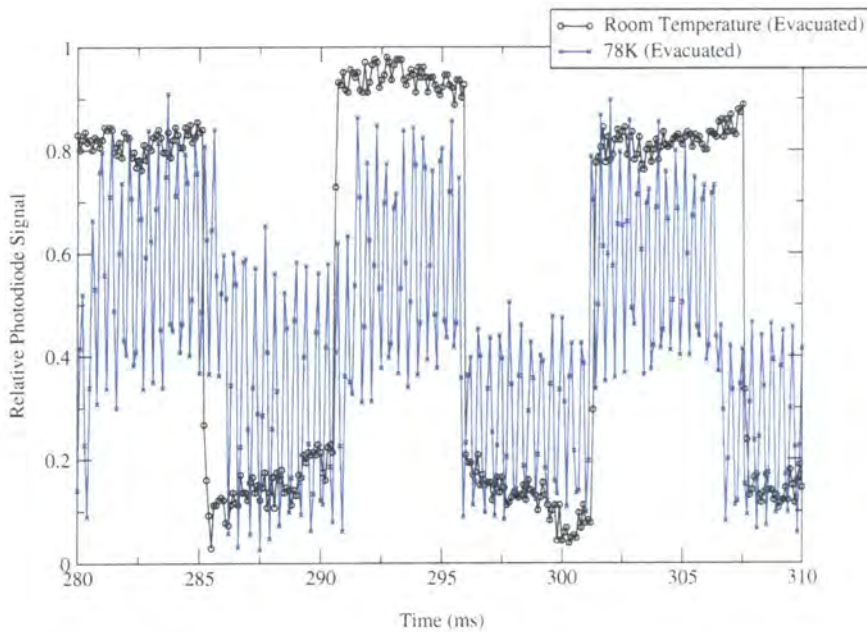
Figure 5.14: Comparison of room temperature and 78K MMDM dynamic responses for MMDM B driven at 100Hz

C, shown in Figure 5.15 at 250Hz is lower than for the preceding measurements, due to external factors. However, it is clear that the high frequency components observed for MMDM B are still present. The change in the response between 0V and 180V is not sufficient in this case for any meaningful comment on the rise and fall time. More information will be apparent in the power spectra, over the full 1s measurement.

Again, the signal to noise measurement for MMDM A at 500Hz, shown in Figure 5.16 is low. While it is clear that there is a strong noise component, this noise does not contain a very high frequency component as was observed for MMDMs B and C. It is possible that this high frequency noise is still present, but at a much higher frequency, such that the photodiode is merely detecting the time averaged noise component.

There are two potential reasons for the different noise characteristics between MMDM A and the other two MMDMs. The first is that the differences between the two MMDM batches cause genuinely different dynamic responses. The second is that the dynamic responses are directly dependent on the initial surface figure of the MMDMs. This will be discussed further in Section 5.5.
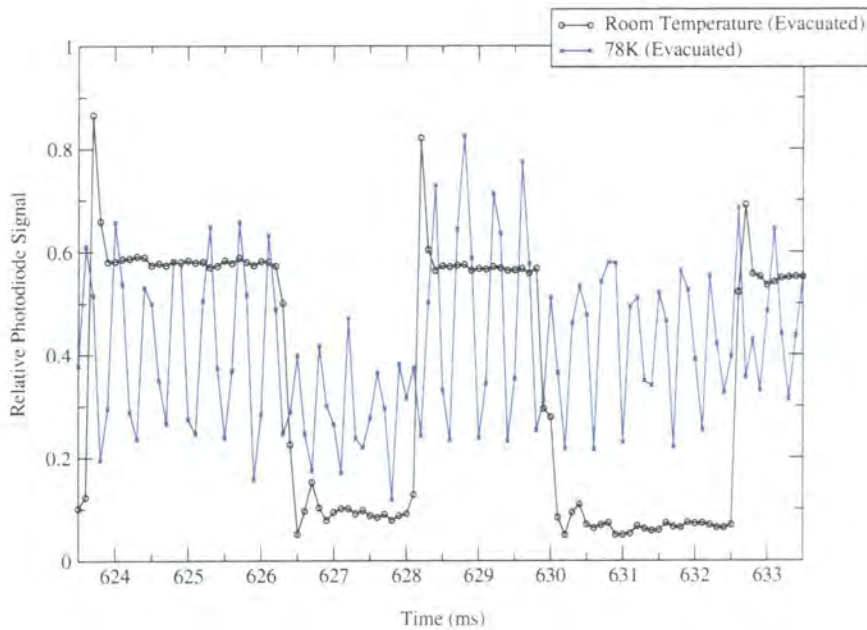
Figure 5.15: Comparison of room temperature and 78K MMDM dynamic responses for
MMDM C driven at 250Hz

5.4.2.2   Statistics

Statistics are not offered for the cold dynamic response of the MMDMs. The reason for
this is that there is no simple way to separate the upper and lower populations, since the
two populations occupy overlapping voltage ranges, see for example, Figure 5.14.

5.4.2.3   Power Spectra

The power spectra for the cryogenic tests are presented here. Figure 5.17 shows the
power spectra for the 3 MMDMs driven at 50Hz at 78K and at room temperature, with
the dewar evacuated in both cases. The blown up region for MMDM A at 78K illustrates
the high frequency component of the noise (note that the blown up region has linear axes:
for the main graphs, the time axis is logarithmic). These components are sufficiently
large to be visible without zooming in for MMDMs B and C. It is clear that the harmnics
of the cooled MMDM are the same as for the room temperature case. Also, with the
exception of frequencies over 2kHz, there is very little variation in the dynamic response
of the MMDMs upon cooling to 78K. The only other significant variation occurs at very
low frequencies for the results for MMDM C. It is unclear what the source of this noise
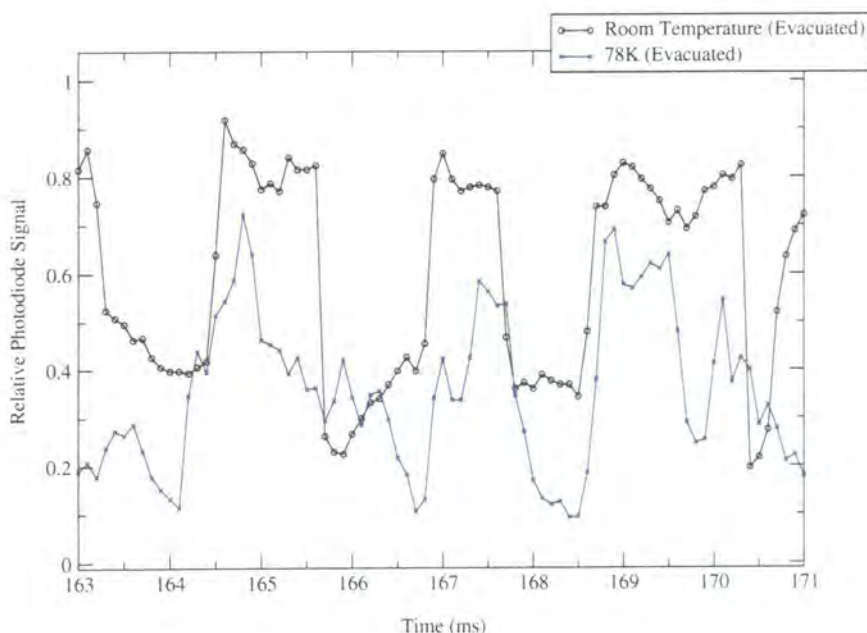
Figure 5.16: Comparison of room temperature and 78K MMDM dynamic responses for MMDM A driven at 500Hz

is, but it was common to each of the cold measurements of MMDM C. It should be noted that, in the case of MMDM C at 78K, the graph was normalised to the peak at 50Hz, rather than to the largest peak. This was done in order to aid comparisons to the other sets of results.

The results for the power spectra at 250Hz are presented in Figure 5.18. This again shows that there is no difference between the room temperature and 78K results for MMDM A for frequencies below ~2kHz. For MMDM B, the same is almost true, although there is some low frequency ($\lesssim$50Hz) component to the signal. This is potentially measurement noise, or some external factor (for example, a drift in the laser intensity). For MMDM C, the cold results are more noisy, and the low frequency noise component is apparent for frequencies $\lesssim$100Hz. Again, this could be due to some external factor. It should be noted that the results for MMDM C at 78K were normalised to the peak at 250Hz rather than the absolute maximum, which occurred at a very low frequency. In all three cases, it must be emphasised that the 78K results are similar to the room temperature results between 100Hz and 2kHz.

The power spectra for a driving frequency of 500Hz are presented in Figure 5.19. The case of MMDM A shows little variation between the cold and room temperature results,
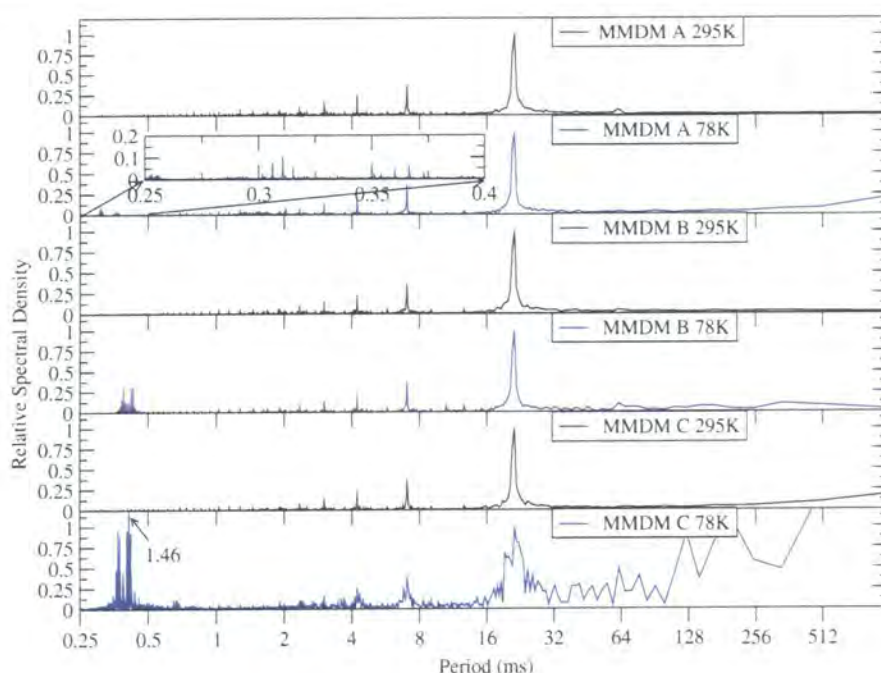
Figure 5.17: Power spectra for driving each MMDM at 50Hz at 78K and room temperature

although there is an additional spike at a period of 0.365 ms (2.7kHz) in the cold data. Again, for frequencies below 2kHz, there is little difference between the two sets of results. There is a slight difference in the scaling, since the graphs were normalised to different peaks. In this case, since there were several peaks near the driving frequency, it was decided to leave the scaling to be on the largest peak corresponding to a period less than 64ms. This meant that the room temperature MMDM A results were normalised to the 20ms (50Hz) noise peak, while the cold results were normalised to the peak at 1.4ms (~700Hz).

The cases of MMDM B and C are more interesting. The cold results bear little resemblance to the warm results, with a massive peak at 0.388ms (~2.6kHz) swamping the rest of the spectrum. What other detail that can be observed indicates that the smaller peaks do occur at frequencies that correspond to the observed room temperature peaks. It would appear that some sort of resonant mode at 2.6kHz is being excited by driving these two MMDMs at 500Hz.
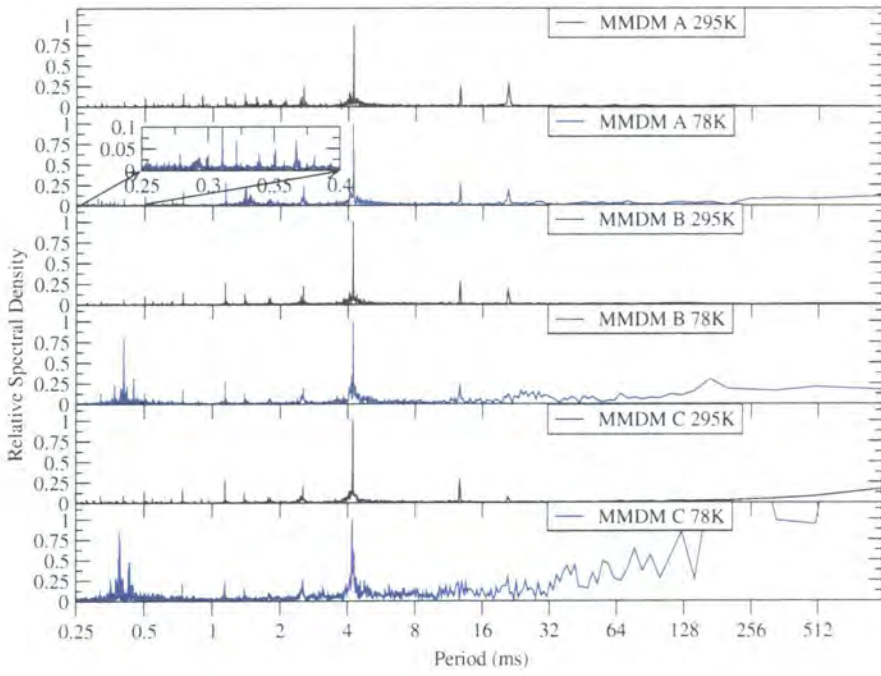
Figure 5.18: Power spectra for driving each MMDM at 250Hz at 78K and room temperature
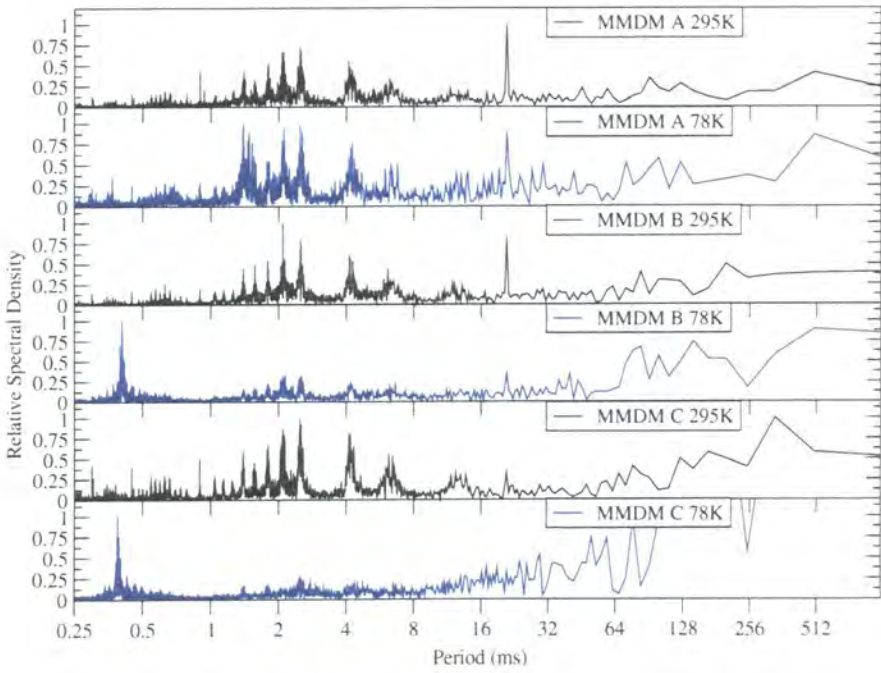
Figure 5.19: Power spectra for driving each MMDM at 500Hz at 78K and room temperature

5.5   Discussion

The preceding results show that the dynamic response of an MMDM is not affected by
evacuating the dewar. This implies that it will not be possible to increase the maximum
operating frequency of an MMDM by removing air damping through using the MMDM
in a vacuum. This is significant, as previously air damping had been considered to be
the factor limitng the maximum operating frequency of the MMDMs. However, it does
raise the potential of increasing the MMDM maximum frequency by optimising the man-
ufacturing process for an enhanced dynamic response by, for example, manipulating the
membrane tension.

It has also been established that, within certain limits, cooling the MMDM does not
effect the dynamic response of the MMDM. These limits are explored in Section 5.4.2.3.
Beyond the areas where the room temperature and cold results match, the main discrep-
ancy is a high frequency signal superimposed over the desired signal. This high frequency
signal is both larger and at a lower frequency for the revised MMDMs, B and C. There
are two potential causes for this effect. Firstly, the variation is due to the different initial
surface figures at 78K, where MMDMs B and C are substantially more deformed than A.
In this case, efforts to optimise the design of MMDMs for cryogenic operation would have
only one aim: to reduce the initial surface aberrations. A potential cause for this ringing is
that the membrane wafer is warped by the cooling process and is then rocking on the two
mounting points. This would suggest that the static and dynamic performance are linked,
since reducing the warping would both inprove the initial surface figure and reduce the
magnitude of the high frequency ringing. Alternatively, the correlation between inferior
initial surface profile and inferior dynamic response could be coincidental. In this case,
it may be possible to optimise the design for dynamic operation, although the designer
would have to take care to avoid improving the dynamic response to the detriment of the
initial surface figure.

It should be possible to discriminate between the two cases outlined above at room
temperatures by artifically introducing surface aberrations onto an MMDM, by either
actuator control or deforming the mounting, and examining the MMDM dynamic response
in this case. If no change is observed, then the dynamic response characteristics are
intrinsic to the MMDM; otherwise they are a consequence of the initial surface aberrations.

5.6 Conclusions

In this chapter, the dynamic characteristics of a sample of three MMDMs at room temperature and at 78K have been presented, for driving frequencies from 50Hz to 500Hz. It has been shown that evacuating the dewar has no effect, within measurement limits, on the dynamic properties of the MMDMs. Statistics have been presented for the room temperature results, both evacuated and at atmospheric pressure.

The 78K results are also very similar to the evacuated results. The principal difference is the presence of a high frequency (2kHz) ringing over the desired signal. This ringing was strongest for MMDM C. The initial stages towards further investigation and elimination of this phenomena are also discussed.

The MMDMs have been shown to be suitable for operation at room temperature for operation as wavefront correctors up to at least 250Hz; faster operation would require the use of alternative electronics. These tests have been conducted with the electronics provided with the MMDMs (as described in Section 5.2.1).

For cryogenic operation, only MMDM A appears to be suitable as a wavefront corrector. It is clear from the power spectra, that the high frequency component of the signals for MMDMs B and C are too large for these devices to be operated as wavefront correctors.

However, the fact that MMDM A is from a different batch to B and C does reinforce the prospect of optimising the design of MMDMs for cryogenic operation, an idea raised in Section 4.4.10. One method of investigating the potential optimisation process has been outlined in Section 5.5.

Considering the worst case scenario, where the dynamic response of MMDM A is the best that can be achieved, MMDMs would still be almost as suitable for operation as wavefront correctors at 78K as they are at room temperatures. The high frequency component illustrated in the insets for figures 5.17 and 5.18 would be the cause for some concern, however, it is equally clear from those figures that the vast majority of the power is going to the desired driving frequencies.

To summarise, of the three MMDMs tested, one (MMDM A) has a suitable dynamic response to be considered to be acceptable as a wavefront corrector at 78K. In addition, the prospect of optimising the design of MMDMs for cryogenic operation is intriguing. The idea of optimising the design is encouraged by the fact that MMDM A is from a different batch to the other two MMDMs, and has less intial surface deformation from

cooling. It is hoped that a design that minimises the initial surface deformation would also optimise the dynamic response.

Chapter 6

Simulated System for Wavefront Correction Using a Curvature Sensor

6.1 Introduction

Roddier (1988) proposed that an AO system could be constructed from a curvature sensor and membrane mirror in such a way that the response to an aberrated wavefront from the wavefront sensor was directly proportional to the wavefront corrector signals required to correct the aberrations in the wavefront. The main advantage of such a system is that it eliminates matrix multiplication within the control loop, and hence results in a shorter delay between detecting an aberration and correcting it. In this Chapter, the aim is to verify that this method works through the use of a simulated system. Note that this differs from the existing curvature sensing systems, such as CFHT (Rigaut, Salmon, Arsenault, Thomas, Lai, Rouan, Véran, Gigan, Crampton, Fletcher, Stilburn, Boyer and Jagourel 1998), in that the wavefront reconstruction step is being completely eliminated in this simulated system. This simulation utilises theoretical influence functions rather than the experimentally measured influence functions for reasons to be discussed in Section 6.4.1. These theoretical influence functions have been previously compared to room temperature experimental influence functions by Dayton et al. (2000). In this Chapter, the work in Section 6.4.1, which compares theoretical influence functions to cryogenic and room temperature experimental influence functions, has been previously published (Dyson et al. 2001). The effects of varying parameters within the simulated system, such as beam size, are also evaluated and discussed. This work is not specific to cryogenic adaptive optics; the conclusions will be applicable to both room temperature and cryogenic systems. The

motive for this particular system is that, by eliminating the wavefront reconstruction, the feedback loop within the adaptive optics system is simplified.

6.2 System

The simulated system is presented in Figure 6.1. It is based on the system proposed by Roddier (1988). The MMDM is shown as a transmissive, rather than a reflective component for clarity. Three systems are shown in the diagram; one showing the detector in the focal plane of the system, and two with the detector planes P_1 and P_2, which are the two defocussed images required for curvature sensing. Throughout this chapter, the term 'curvature image' will be used to describe the image obtained by taking the contrast between the images in planes P_1 and P_2; hence the pixel (x, y) in the curvature image is defined as:

$$\frac{P_1(x, y) - P_2(x, y)}{P_1(x, y) + P_2(x, y)} \tag{6.1}$$

The simulated system simply changes the distance between the final lens, L_3 and the detector. This would be awkward to implement in a real system, however a similar variation in optical path length can be achieved using a vibrating reflecting membrane (Roddier 1999). Alternatively, the same results can be achieved by utilising a beam splitter between the MMDM and the field lens, and having two duplicate systems from the field lens through to the detector. Due to the large focal length of the MMDM, this simulated system would not be practical. However, additional optics could be utilised to shorten the optical path length. This has not been simulated, since the simulation is intended as a proof of concept, rather than as a blueprint for an operational system.

This simulated system uses a 37 actuator MMDM, so 37 subapertures were used for the detector. This maintains the 1:1 correspondence between actuators and subapertures required to dispense with the wavefront reconstruction. The detector is considered to be a pixellated detector, such as a CCD, to allow for flexible definition of the subapertures (Burley, Walker and Johnson 1998). Although 37 acutators is low-order, existing systems have been deployed with lower order correction, such as PUEO on the CFHT which uses 19 actuators and 19 subapertures (Rigaut et al. 1998). CFHT is a 3.6m telescope; for Gemini North, an 8m telescope, a 36 channel system, Hokupa'a, was initialy installed, although this is intended to be superceded by a laser guide star system (Graves,
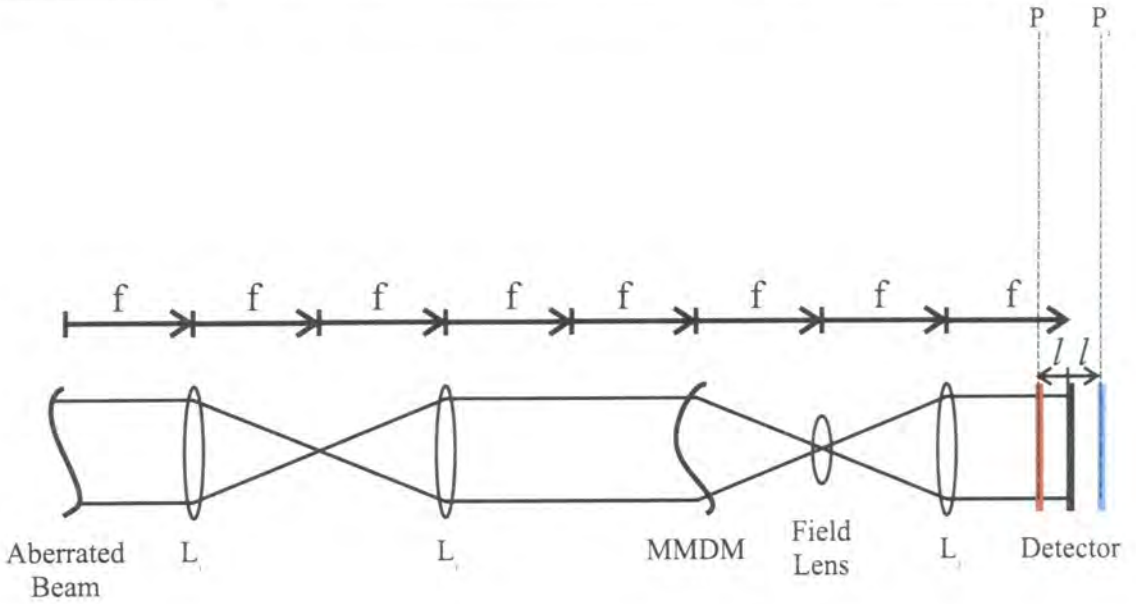
Figure 6.1: Layout of adaptive optics system using a curvature sensor.
For clarity, the MMDM has been shown as a transmissive, rather than reflective element. The focal length of the biased MMDM is f. The three lenses, L_1, L_2, L_3, each have the same focal length as the MMDM. The field lens has a focal length of $\frac{f}{2}$. The extra-focal distance, l, is the distance from the focal plane to planes P_1 and P_2, which are used to generate the curvature image.

Northcott, Roddier, Roddier and Close 1998, Roth, Guyon, Chun, Jensen, Jorgensen, Rigaut and Walther 2001). A similar 36-channel system is also used on the 8.2m SUBARU telescope (Takami 2001).

The most significant aspect of the simulated system described in this Chapter is that it eliminates the wavefront reconstruction completely. Each MMDM actuator and detector subaperture pair are considered independently of the other channels. This is one of the main advantages of curvature sensor wavefront sensors (Roddier 1988, Roddier 1991). It has been demonstrated through simulation that a curvature sensor system gives good wavefront correction where the drive signal to one actuator is generated from a linear combination of the signals on the corresponding suabperture, and the surrounding subapertures (Roddier and Roddier 1989). However, it has yet to be demonstrated that considering each channel independently provides wavefront correction. In addition, this simulation will use a model of a real membrane mirror, specifically an MMDM, rather than a theoretical perfect membrane.

This simulated system is not intended as a replacement for an astronomical AO system; rather, it is intended to highlight the feasibility of this method for low-cost low-order adaptive optics. By eliminating the control loop, however, this method may become significant for astronomy when very high order systems are required for future extremely large telescopes, where the computational burden of the matrix inversion in the control loop becomes overwhelming.

6.3 Software Toolkit

The requirements for the toolkit used in this simulation were that it had to be able to handle beam propagation and the application of lenses, aberrations and influence function to that beam. Hence, the Lightpipes beam propagation toolbox from Oko Technologies was chosen (Vdovin 2001c). This toolkit provided several programs that were essential in the construction of the simulation. Firstly, it includes several methods of beam propagation. The 'forvard' command was utilised, which implements a numerical solution of the Fresnel equation, using a method outlined in Southwell (1981) and Sziklas and Siegman (1975). Functions were included within the toolkit for the application of lenses and Zernike aberrations. The MMDM was modelled through two applications of the 'filter' program within Lightpipes. The first application applied an intensity filter to eliminate the parts of the beam outwith the MMDMs diameter, while the second application applied a phase filter to represent the membrane surface. The applied phase filter was generated by summing the 37 influence functions and dividing the result by an appropriate normalisation constant. Using this method, multiplying one influence function by a constant represented poking an actuator in the model. Initially, all the influence functions were multiplied by 0.5, to represent the biased position of the membrane.

The pseudo-code algorithm in Table 6.3 illustrates the structure of the open-loop simulation program.

The major limitation of this toolkit was that it only models monochromatic light, so diffraction effects can be significant. This simulation modelled the system with a Helium-Neon laser, of wavelength λ=633.9nm.

Read actuator signals

Generate global influence function (initially blank)

FOR each actuator

    add (signal × actuator influence function) to global influence function

NEXT actuator

Divide global influence function by normalisation constant

Create Lightpipes beam of chosen diameter

Read aberrations to be applied

Apply Zernike aberrations

Propagate beam to MMDM through relay optics

Apply generated global influence function

Propagate beam to field lens

Apply field lens

Propagate beam to lens L_2

Apply lens L_2

Split beam into beams 1, 2 and 3

Beam 1:

    Propagate beam to detector in plane P_1

Beam 2:

    Propagate beam to detector in plane P_2

Beam 3:

    Propagate beam to detector in focal plane of lens L_2

FOR each subaperture

    measure integrated signal, by subtracting beam 1 from beam 2 within area

of subaperture

NEXT subaperture

Table 6.1: Pseudo-code Algorithm for open-loop simulation.

Planes and Lenses are defined in Figure 6.1.

6.4 Simulation Preparation and Tuning

6.4.1 Theoretical Influence Functions

The evaluation of the simulated curvature sensor system was conducted with theoretically calculated influence functions. These were generated with another program from Oko Technologies, which uses a simultaneous over-relaxation algorithm to calculate the membrane shape, as described in Press (1993). This program was particularly suitable as it had been developed specifically to model the response of an MMDM, and the output was in a compatible format for the Lightpipes phase filter. These theoretical influence functions have been previously compared to room temperature influence functions by Dayton et al. (2000). Presented in Figure 6.2 are cross sections through the experimental and theoretical influence functions of actuators 1, 2, 8 and 20 from MMDM B, with a center to center actuator spacing of 1.25mm (see Figure 2.8). This Figure has previously been published (Dyson et al. 2001).

(a) By Actuator:
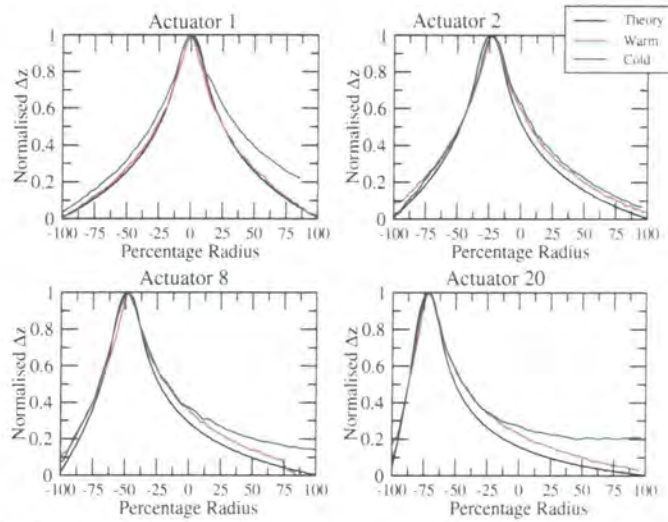
(b) By Conditions:
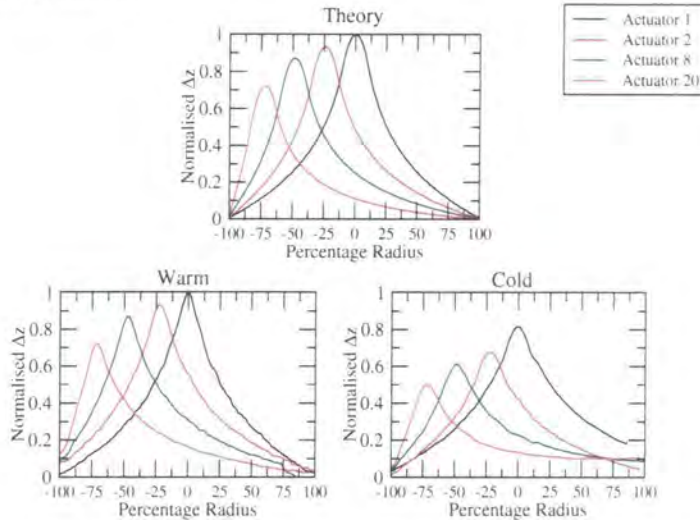
Figure 6.2: Cross-sections through theoretical and experimental influence functions. Figure 6.2a is normalised for each actuator independently, while 6.2b is normalised to the central actuator for the warm results.

It is clear that the theoretical influence functions are virtually interchangeable with the room temperature experimental influence functions. There is also a strong similarity between the shapes of the cold influence functions and the theoretical influence functions. However, these experimental influence functions are not suitable for use in this simulation due to the noise present in the experimental results. The simulation generates the membrane surface by summing the 37 individual actuator influence functions, and then dividing by a normalisation constant, determined in Section 6.4.2. Considering the area

over one actuator pad, the local shape is therefore determined by the measured local signal, plus the noise from each measured actuator influence function. Cosequently, for the area, over one actuator, the contribution consists of 1 part signal and 37 parts noise. This effect is compounded by the noise being a systematic artefact from the Zygo phase shifting interferometer used in Section 4.4.4 to measure the influence functions. This results in a noise-dominated modelled surface of the MMDM. This does not apply to the theoretical influence functions as there was no noise present. This is illustrated in Figure 6.3, which shows an image of the biased membrane for a set of experimental influence functions, and a similar image for the theoretical influence functions. The systematic banding from the Zygo can be seen in the model of the biased membrane generated from the experimental influence functions. Hence, for this simulation work, the theoretical influence functions were used exclusively.

(a) Experimental   (b) Theoretical
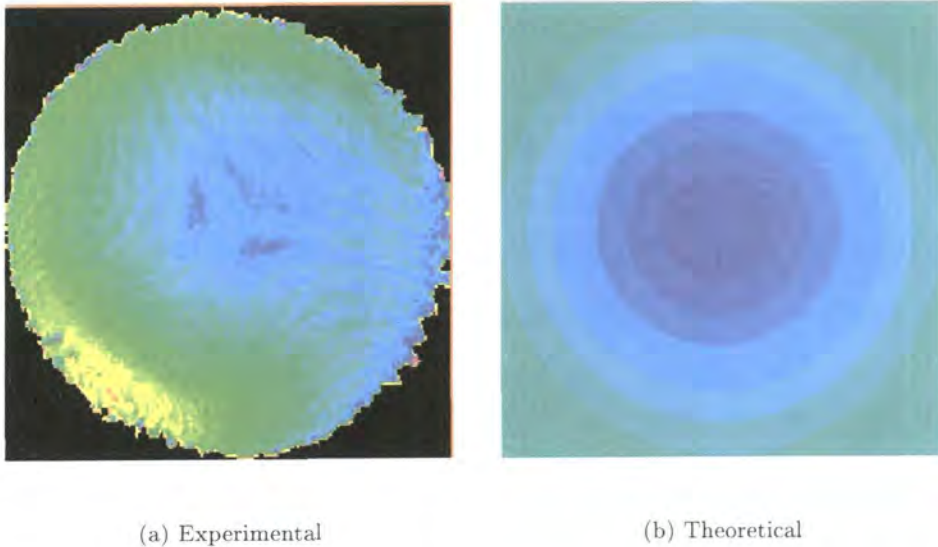
Figure 6.3: Biased membrane shape composed by summing and averaging influence functions.

6.4.2 Focal Length of Simulated MMDM

Several parameters within the simulation had to be tuned. The focal length was the first parameter to be adjusted. This was done by tweaking the normalisation factor in the generation of the influence functions until a simulated MMDM at maximum throw had the same focal length as the physical MMDM, which is 1200mm.

6.4.3 Subaperture Generation

The subaperture pattern used to detect the signals was constructed by examining the curvature image, formed by subtracting the image in plane P_2 from the image in plane P_1. 37 such curvature images were examined, with a different actuator poked in each image. The area with a dramatic difference from the null image was marked out as the subaperture for the relevant actuator. Note that these subapertures were not contiguous. Since this is a proof of concept simulation, the loss of light is not an issue. For a practical system, it would be beneficial to maximise the fill-factor. Further, for a practical system, it would be possible to have the subapertures automatically generated during calibration by tagging pixels where the change from the null image is over a certain threshold value. For simplicity of computation, square subapertures were used. Flexible specification of subapertures could be achieved in a practical system by foregoing the commonly used avalanche photodiodes in the wavefront sensor, and utilising a CCD detector instead (Burley et al. 1998). Having constructed the subapertures, it was then possible to examine the wavefront sensor response to poking actuators of the MMDM for various beam diameters. Note that the subaperure positioning was generated with a beam radius of 7.5mm and an l (distance from focal plane to either P_1 or P_2, as defined in Figure 6.1) of 400mm.

Note that the peripheral subapertures need to be defined such that the edge of the pupil image passes through the subaperture. This is to ensure that the outermost subapertures measure the tip on the beam, rather than curvature (Roddier 1988). In the system described here, the outermost subapertures were sufficently large that this condition was met for all beam diameters greater than 4.5mm; for smaller beams fewer actuator-subaperture pairs would need to be used to ensure that this edge condition was met. The importance of this edge condition is that the remaining subapertures detect the Laplacian of the wavefront; however Zero-Laplacian modes, such as astigmatism, are not detected by these subapertures. Hence, the peripheral subapertures are the only ones to detect these modes. Zero-Laplacian modes are still corrected away from the periphery of the beam, due to the extensive influence functions of the actuators. However, since the sensing is only done by a subset of the subapertures, this correction is likely to be less good than that for the modes that are sensed by all of the subapertures.

6.4.4   Beam Diameter

The second paramter to be tuned was the beam diameter. The wavefront sensor response was examined for beam radii between 2.5mm and 7.5mm, which corresponds to the diameter of the MMDM.

(a) Actuator 1

(b) Actuator 2

(c) Actuator 8
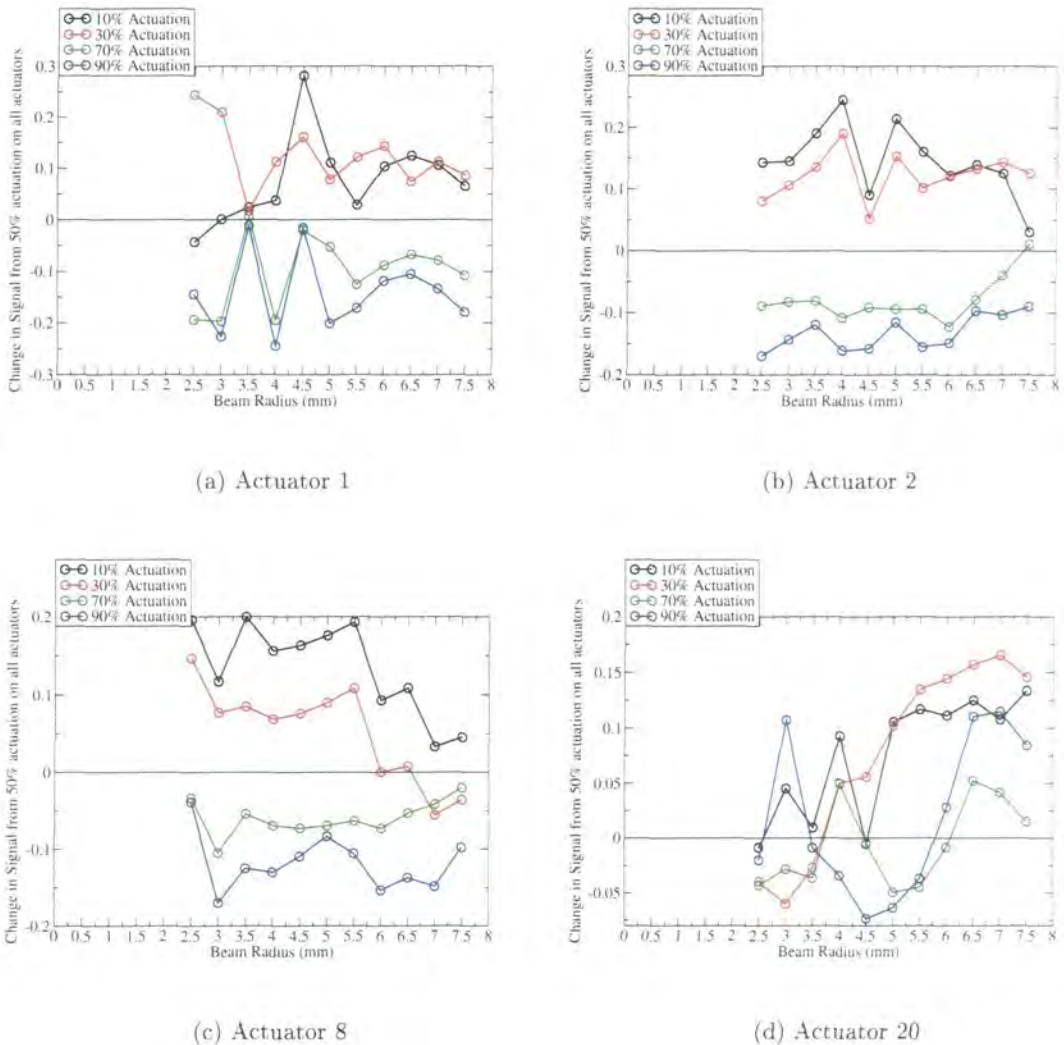
(d) Actuator 20

Figure 6.4: Response of wavefront sensor to poking individual actuators for varying beam size.

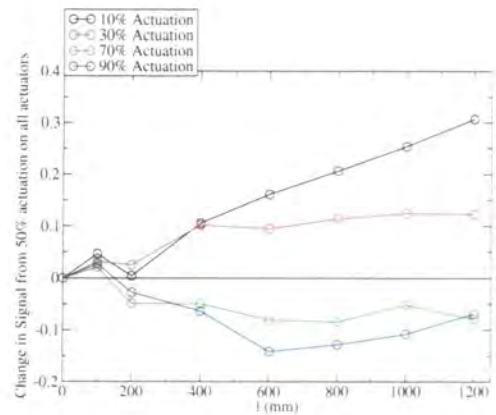Figure 6.4 shows the wavefront sensor response against beam radius, for actuator and subaperture pairs 1, 2, 8 and 20. For reference, Figure 2.8 is reproduced as Figure 6.5, and illustrates the positions of the actuators. The graphs show the difference in the corresponding wavefront sensor subaperture signal from the null signal (with all actuators at 50%) for poking each actuator to 10, 30, 70 and 90%. For comparison, the distance of each actuator from the center of the MMDM is shown in Table 6.2. From this, it is clear
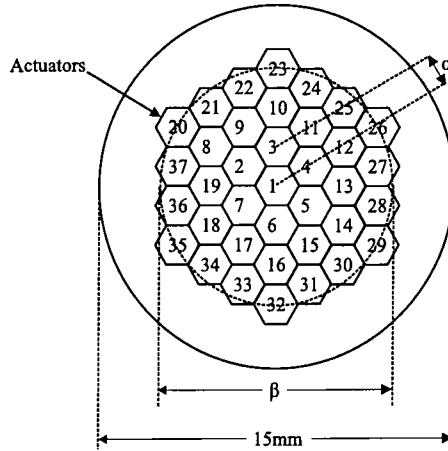
Figure 6.5: Actuator structure of the MMDMs

In the case of MMDM A, dimension α in the diagram corresponds to 1.75mm, hence β is 10.5mm. In the cases of MMDMs B and C, dimension α is 1.25mm, and β is 7.5mm

that the measurement with a beam radius of 2.5mm for subaperture 20 is likely to be simply noise. The main component of the noise generated is from diffraction effects; no random noise is added to the system. The detected signals for actuator 20 for all beam radii less than 5.0mm appear to be essentially random. Hence, the signal at these radii is considered to be noise-dominated. This puts a useful constraint on the minimum beam diameter that can be used for 37-channel correction.

The detected signal for large beam radii, over about 6.0mm, behaves erratically. Thus, there must be some effect from the periphery of the membrane, where there is no actuation, affecting the beam, which then gets detected by the subapertures. This idea is reinforced by this effect being greatest for actuator 20, and least for actuator 2, with a negligible effect on actuator 1. This provides a constraint on the largest beam radius that may usefully be used.

Actuator	Distance (mm)
1	0
2	1.25
8	2.50
20	3.75

Table 6.2: Distance from center of MMDM to center of actuator for actuators 1, 2 8 and 20

This leaves a narrow range of beam sizes, from 5.0 to 6.0mm which may be useful for the forthcoming tests. There are two characteristics of the wavefront sensor response that can be assessed within this regime in this test. Firstly, the polarity of the measurements is significant. For an actuation of greater than 50% to a given actuator, the response on the corresponding subaperture should be negative. Similarly, for an actuation of less than 50%, a positive signal should be detected. This polarity requirement is met for all actuators for all radii within the region of interest (5.0mm to 6.0mm), with the single exception of actuator 20 with a beam radius of 6.0mm.

The second requirement was that the response for a 40% change from the bias signal to an actuator should be greater than the response for a 20% change. This requirement was met for all beam radii for actuators 2 and 8. However, a beam radius of 5.0mm was the only appropriate radius for actuators 1 and 20. Hence a beam radius of 5.0mm was used for the tests in the remainder of this chapter.

The cause of this variation in subaperture response with beam size is that the MMDM response is not pure curvature. Figure 6.6 shows best fit power laws fits to the theoretical influence functions for actuators 1, 2 8 and 20. The influence functions have been split into two parts, each going from the perimeter to the maximum value in opposite directions. To fit the data, one of these sections has then been mirror-imaged. Consequently, one section is longer than the other for actuators 2, 8 and 20 since these actuators are not central. Actuator one is also not central, due to a slight misalignment between the actuator pad and the membrane in the input data used to generate the influence functions. As has been previously shown, in Section 4.4.5, real MMDMs may also have an offset between the actuators and the membrane.

The power law fits (generated by the software package Grace (Stambulchik 2000)) for these influence function sections range from $y \propto x^{1.2}$ to $y \propto x^{1.6}$. For a pure curvature influence function, these would be $y \propto x^2$. If the fit is restricted to a subsection of the influence function, this behaviour can be seen with the theoretical influence functions, as demonstrated by the fit shown in Figure 6.7. This region is from the center out to 60% radius of the membrane. This region where the power law fit corresponds to pure curvature varies with the radial position of the actuator. Hence, the beam diameter has to be tuned to correspond as well as possible to the region where all actuators produce pure curvature.
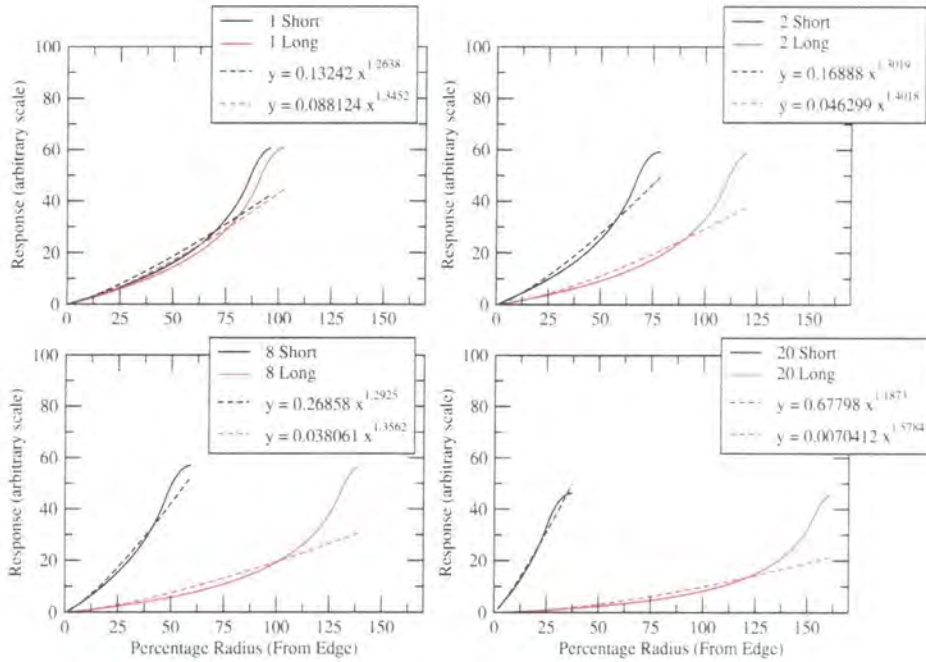
Figure 6.6: Power law fits to theoretical influence functions.
Data in solid lines, fit in dashed lines.

6.4.5 Extra-focal Distance, l

The third parameter to be tuned was l, the separation between the focal plane and either of the defocussed planes, P_1 or P_2, presented in Figure 6.8. The response should vary linearly with increasing l, with variable sensitivity being one of the advantages of a curvature sensor system (Roddier 1988). This behaviour is observed, to an extent, for all actuators. However, saturation appears to occur for l greater than 600mm for actuator 1, at 10% and 90% actuation, and actuator 20, at 90% actuation. Hence, an l of 600mm was used for the subsequent tests.
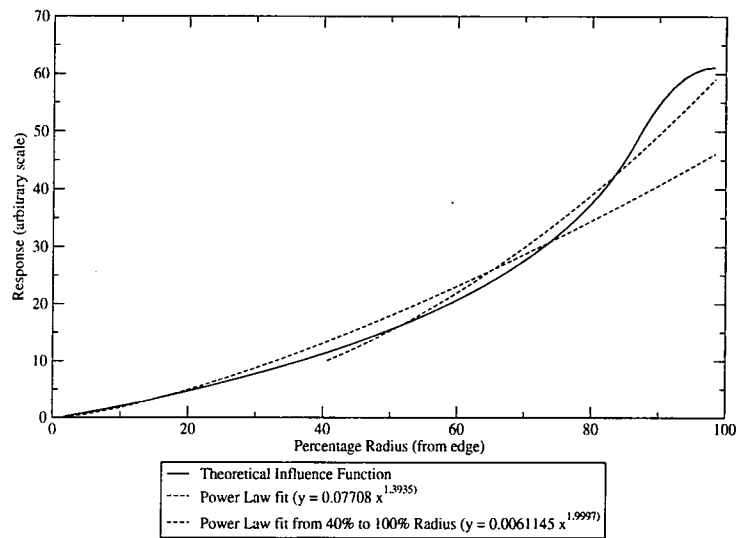
Figure 6.7: Power law fit for one subsection of actuator 1 influence function

Dashed lines show fits, solid line shows data.
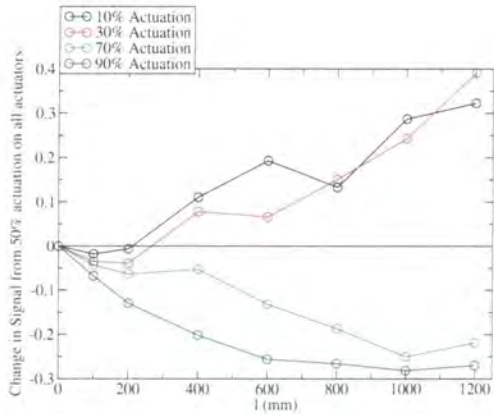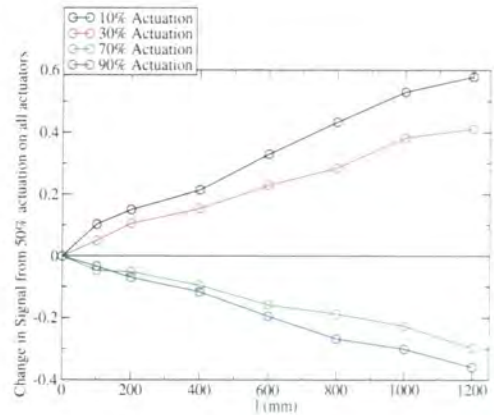
(a) Actuator 1
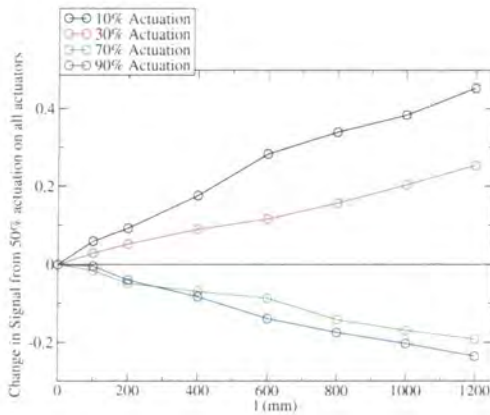
(b) Actuator 2

(c) Actuator 8

(d) Actuator 20

Figure 6.8: Response of wavefront sensor to poking individual actuators for varying extra-focal distance, l.

l is defined in Figure 6.1, and is the separation from either P_1 or P_2 to the focal plane.

6.5 Curvature Sensor Response to Individual Actuators

In this section the wavefront sensor response across all subapertures will be presented for a selection of actuators. For the optimal curvature sensor and membrane mirror system, each actuator will produce a signal in one and only one subaperture. It should be noted that the initial membrane formed by applying 50% actuation to all actuators does not give a zero signal on all subapertures. The wavefront sensor signals obtained for the theoretical biased membrane are shown in Figure 6.9. This is indicative of the biased membrane not providing pure focus, as a consequence of, for example, slight actuator misalignment in the model for generating the influence functions. The first step in the wavefront correction to be shown in Section 6.7 will be to 'flatten' the theoretical biased membrane to a pure defocus shape. For the results shown in this section, though, the base wavefront sensor signals shown in Figure 6.9 are subtracted from the results.
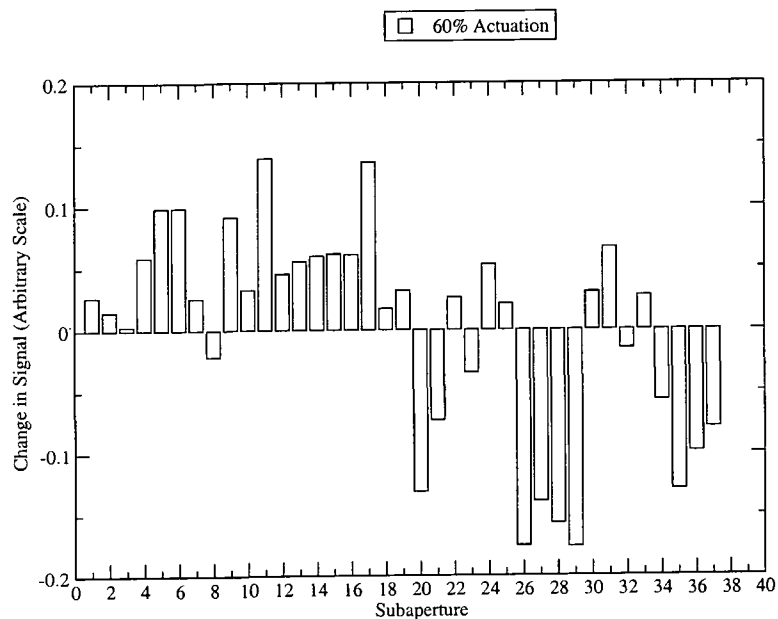
Figure 6.9: Response of all wavefront sensor subapertures to biased membrane.

Some actuator and subaperture pairings show responses that are close to the ideal of a signal in one and only one wavefront sensor subaperture. An example of this behaviour is shown in Figure 6.10, which depicts the wavefront sensor response to driving actuator 7 to 30% and 70%.

The remaining actuators have substantial signals in the corresponding subaperture, but also produce a signal in other subapertures. Actuator 21 is in this category, as
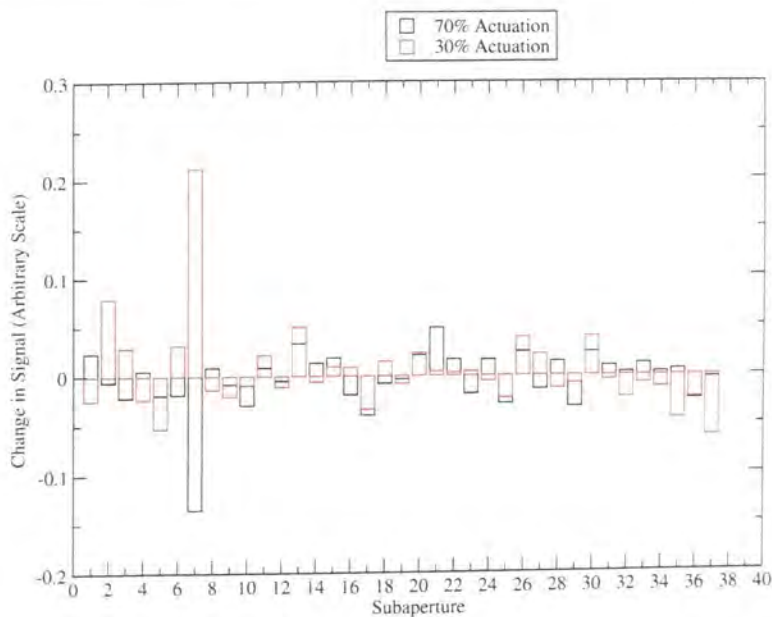
Figure 6.10: Response of all wavefront sensor subapertures to poking actuator 7
Red bars denote 30% stroke of actuator 7, Black bars denote 70%.

shown in Figure 6.11. This behaviour will be ignored in the attempts to correct zernike aberrations described in Section 6.7; for actuator N, it will be assumed that the signals for each subaperture M is zero if $M \neq N$. Additional figures showing the response of the wavefront sensor to poking each individual actuator are presented in Appendix A.

The most significant aspect of the wavefront sensor responses to each individual actuator is that it allows the interaction between the two to be calibrated. Hence, by reversing this process, it should be possible to correct a given subaperture signal by simple application of the corresponding signal to the appropriate actuator. In this scheme, e actuator and corresponding subaperture channel should be independent. Therefore, subaperture signal is multiplied by a linear gain to determine the appropriate cha the signal driving the relevant actuator. In this simulated system, since the test were $\pm 20\%$ from the bias position, then the gain for each actuator is $0.2 \div \frac{\delta}{2}$ v the difference between the upper and lower signals detected by the wavefront
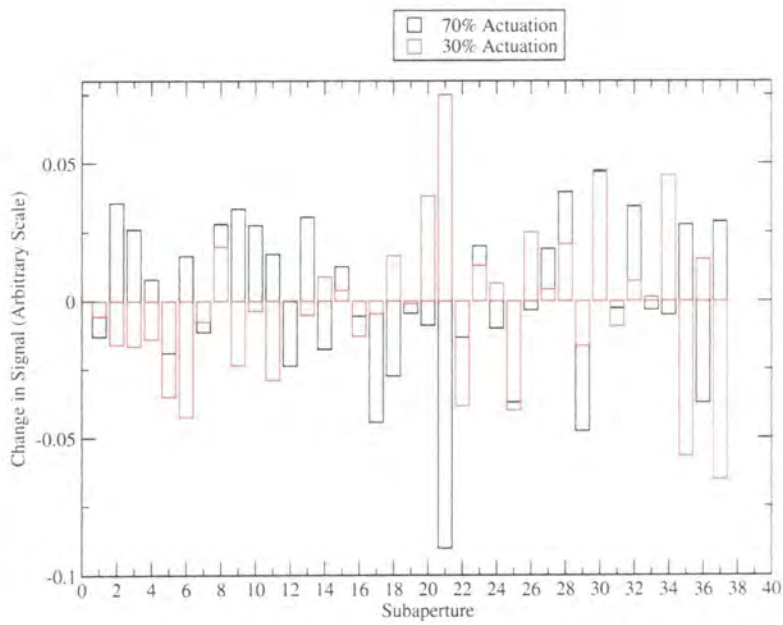
Figure 6.11: Response of all wavefront sensor subapertures to poking actuator 21

Red bars denote 30% stroke of actuator 21, Black bars denote 70%.

6.6   Application of Zernike Aberrations

Having constructed and tuned a simulated wavefront sensor, it was necessary to examine the response of this sensor to the application of Zernike aberrations to the system. Figure 6.9 in Section 6.5 shows the wavefront sensor signals for the biased membrane without the application of any aberration. If the biased membrane introduced pure focus into the system, then the signal for each subaperture would be the same, with a small error due to diffraction effects. Since this is not what is observed, it is apparent that there are other static aberrations introduced into the biased membrane formed from the individual influence functions. In order to demonstrate the sensitivity to Zernike aberrations, the static aberrations introduced by the biased membrane will be subtracted from the following results; for the wavefront correction steps in Section 6.7, the integral aberrations of the MMDM will be restored. The Zernike aberration definitions used are those from Born and Wolf (1980). The Zernike aberrations discussed here are in three groups; those with purely radial dependence, purely azimuthal dependence and those that depend on both. This is summarised in Table 6.3. The following results were all taken with all MMDM actuators at an actuation of 50%, such that the membrane was biased with a focal length of 2400mm. Only the lowest order Zernike aberrations are considered here; for higher order correction, more actuators would be required.

The first two aberrations to be considered will be focus and defocus. These are the aberrations most suited to the MMDMs, as the application of a single voltage to all actuators should generate focus. Figure 6.12 shows the response of the curvature wavefront sensor to the application of focus, while Figure 6.13 shows the response to defocus. Defocus and focus are the same aberration, but defocus has a negative amplitude

Aberration	Dependence
Defocus	Radial
Spherical aberration	Radial
Tip	Azimuthal
Astigmatism	Radial and Azimuthal
Coma	Radial and Azimuthal

Table 6.3: Radial and azimuthal dependencies of the Zernike aberrations used in this section.
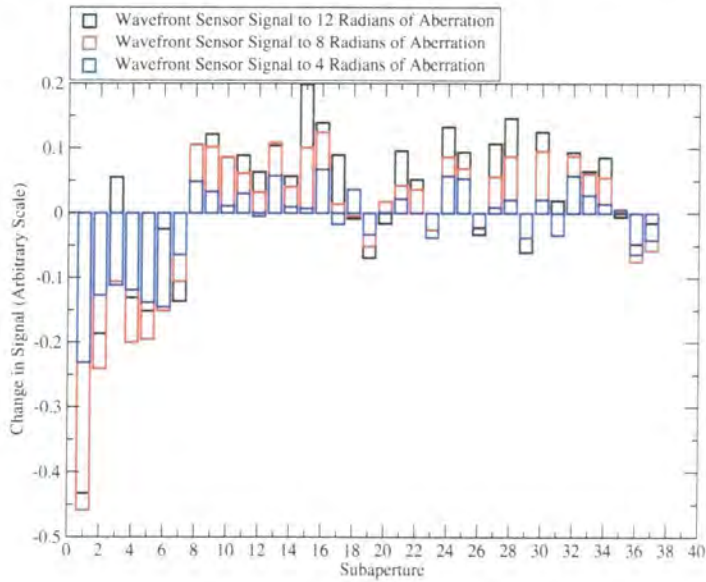
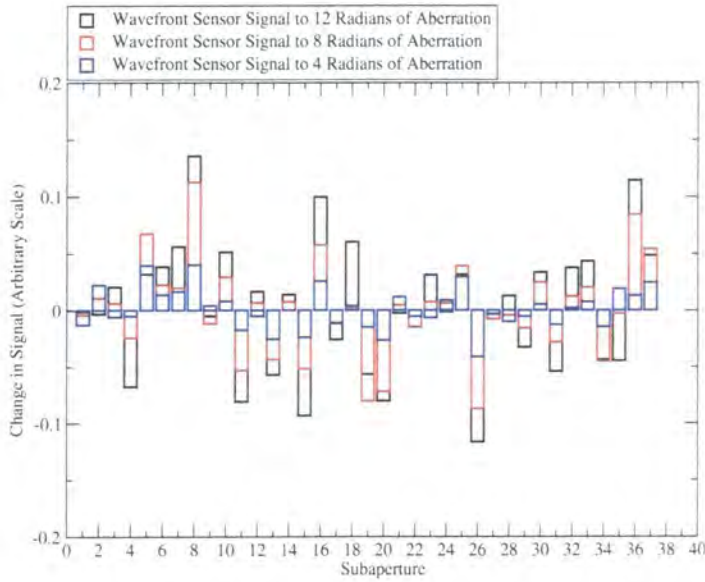Definition of aberrations from Born and Wolf (1980).
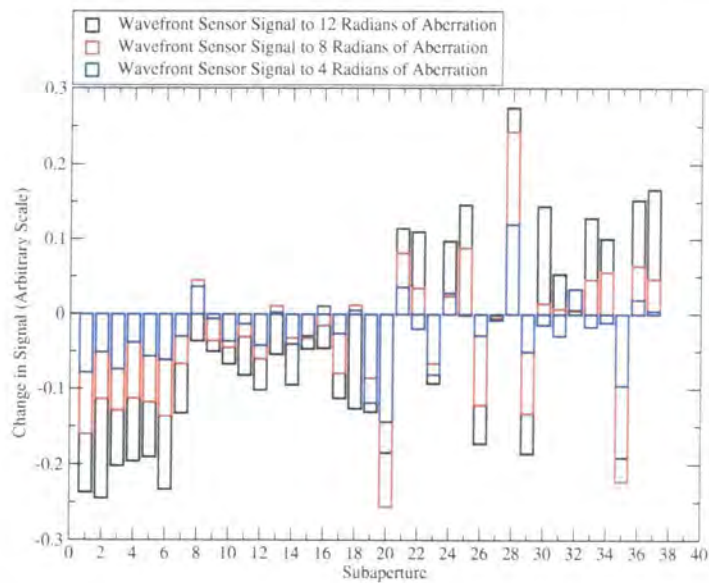
Figure 6.12: Response of all wavefront sensor subapertures to focus.
3 amplitudes of aberration are shown; 4, 8 and 12 radians of aberration at the
membrane perimeter. (2π radians $= 1\lambda = 633.9$nm)

relative to focus. They are both shown here to demonstrate that the outermost, or zone 3,
subapertures do not behave in a similar manner to the central 19 subapertures. The outer
subapertures in a curvature sensor do not measure the second derivative of the wavefront,
curvature, rather they measure the first derivative, tip (Ftaclas and Kostinski 2001). Note
that, for the central 19 actuators, there is a radial dependence to the wavefront sensor
signals. This is most obvious for the case of 8 or 12 radians of focus. This is indicative
of the wavefront sensor detecting spherical aberration as well as the applied focus. The
aberrations are applied purely theoretically in software, therefore this detected spherical
aberration has to be in the wavefront sensor, as opposed to the MMDM.

The next aberration to be considered is spherical aberration, shown in Figure 6.14.
Again, for the central 19 actuators, the wavefront sensor signal is clearly dependent on
the radial position of the subaperture. Extrapolating the trend from the central 19 sub-
apertures out to the outermost subapertures would give a larger signal than that which
is observed. This is again indicative of the outer subapertures measuring tip, rather than
curvature.

The only aberration with pure azimuthal dependence is tip. The wavefront sensor
response to tip is shown in Figure 6.15. It is clear that there is no radial dependence.
However, the expected signal would be to have a strong positive signal on one side of the
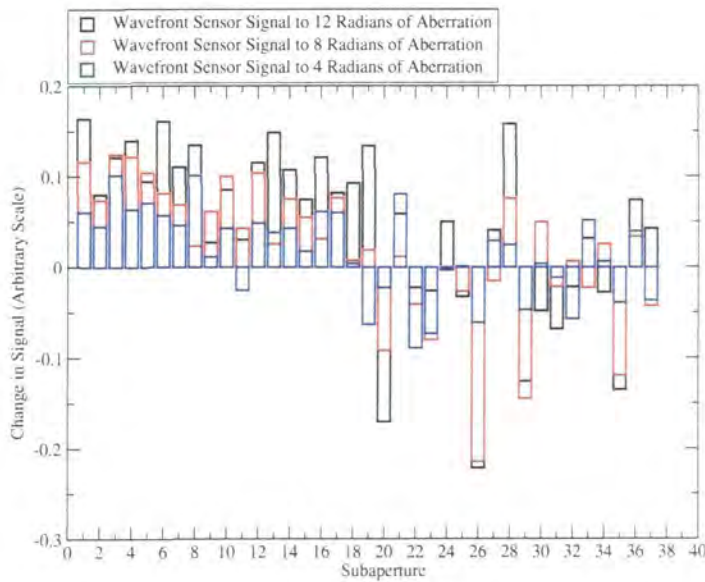
Figure 6.13: Response of all wavefront sensor subapertures to defocus.
3 amplitudes of aberration are shown; 4, 8 and 12 radians of aberration at the
membrane perimeter. (2π radians $= 1\lambda = 633.9$nm)

wavefront sensor, and a corresponding negative signal on the opposite side. This is not
observed, hence the use of this simulated curvature sensor for the detection of tip may
not be possible. Hence, although the outermost actuators are not detecting curvature
in the case of the other aberrations, it is possible that they are also not detecting tip.
It is possible that the outer subapertures are detecting a hybrid combination of tip and
curvature.

The remaining two aberrations, astigmatism and coma, are shown in Figures 6.16
and 6.17 respectively. These aberration have both a radial and an azimuthal component.
The radial component can be observed in both cases, where the strongest signals are
present in the outermost actuators. Note that, in the case of astigmatism, the signal from
some subapertures appears to be saturating for 12 radians of aberration, for example,
subapertures 28 and 36. There is also some evidence of the azimuthal dependence. In
the case of astigmatism, the strongest negative signals in zone 1 are actuators 2 and
5, which are opposite. This is the symmetry anticipated for astigmatism. The zone 1
actuators that are in the region perpendicular to the line defined by actuators 2 and 5
have exclusively positive signals, which is again the symetry expected for astigmatism.
This trend is continued into zone 2, with negative signals being observed in subapertures
14, 15 and 9; and positive signals in the complementary actuators 17, 18 and 12. This

Figure 6.14: Response of all wavefront sensor subapertures to spherical aberration. 3 amplitudes of aberration are shown; 4, 8 and 12 radians of aberration at the membrane perimeter. (2π radians $= 1\lambda = 633.9$nm)

trend does not extend into the periphery actuators.

In the case of coma, the azimuthal dependence is more clear. With the single exception of a small signal on subaperture 26, the subapertures with negative signals for all amplitudes of coma are 2, 7, 8, 17–19, 20–22 and 33–37. Referring to Figure 6.5, it is clear that these subapertures are a contiguous block. All the remaining actuators have a positive signal for at least 2 of the three aberration amplitudes studied.

Figure 6.15: Response of all wavefront sensor subapertures to tip.

3 amplitudes of aberration are shown; 4, 8 and 12 radians of aberration at the

membrane perimeter. (2π radians $= 1\lambda = 633.9$nm)
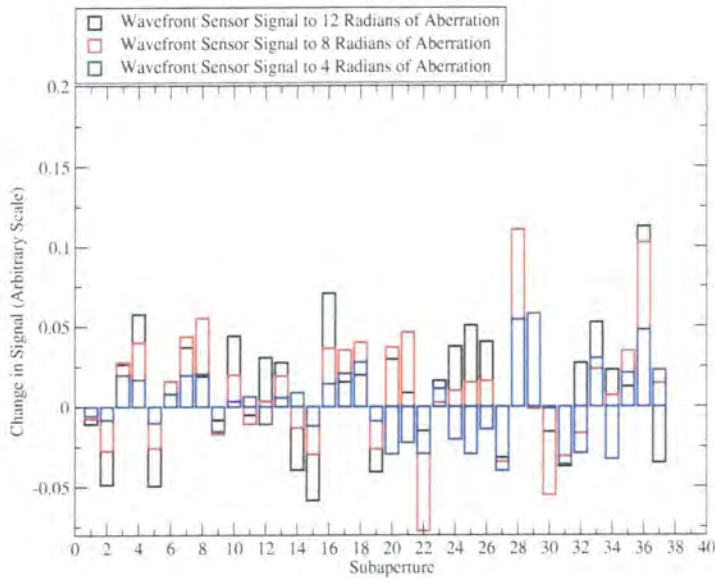
Figure 6.16: Response of all wavefront sensor subapertures to astigmatism.

3 amplitudes of aberration are shown; 4, 8 and 12 radians of aberration at the

membrane perimeter. (2π radians $= 1\lambda = 633.9$nm)
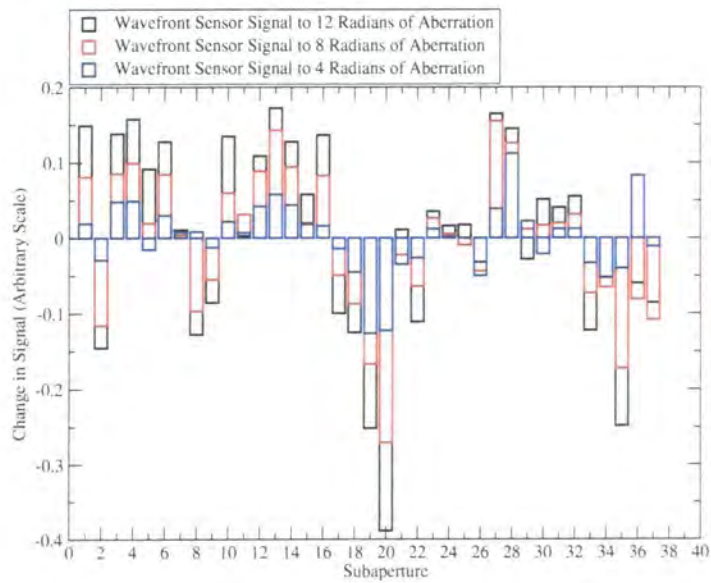
Figure 6.17: Response of all wavefront sensor subapertures to coma.

3 amplitudes of aberration are shown; 4, 8 and 12 radians of aberration at the

membrane perimeter. (2π radians $= 1\lambda = 633.9$nm)

6.7 Wavefront Correction Using the Purely Theoretical MMDM

In Section 6.5, the wavefront sensor response to the individual actuators of the MMDM was determined. In Section 6.6, the response to several Zernike aberrations was measured. Combining these two sets of data should allow the MMDM to correct the aberrations. This Section will determine whether that is indeed the case, and therefore whether the influence functions of the MMDM are sufficiently similar to pure curvature to allow a curvature sensor-MMDM combination to correct wavefronts without reconstructing the wavefront in the control loop. For the corrected wavefronts, three iterations through the feedback loop are used. The first two iterations were identical, while the final iteration used slightly different parameters, as the system tended to overcorrect small signals; possibly due to the 8-bit digitisation of the actuators' influence functions. A threshold of 10% was used for the first two iterations, so any correction to a channel that involved moving an actuator by less than 10% was ommitted. For the final iteration, this threshold was reduced to 5%, and the correction applied to the actuators was also halved.

6.7.1 Point Spread Functions
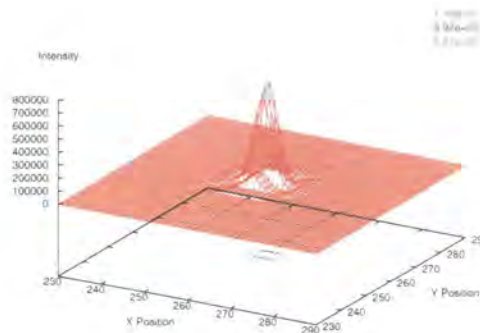
Figure 6.18: Point spread function for perfect system, using lens instead of MMDM. The intensity scale is arbitrary.

The point spread functions are plotted on a square 520 × 520 pixel grid. of side 30mm, giving a resolution of just over 17 pixels per mm in the focal plane. A subset of this grid is presented in each Figure, to show the detail of the point spread funciton in each case. Three iterations through the feedback loop are used to generate the corrected point spread functions. For comparison with the aberrated and corrected results, the perfect system point spread function, replacing the MMDM with a perfect lens of equivalent focal

length, is shown in Figure 6.18. This perfect system is used to calculate the Strehl ratios of the uncorrected and corrected systems, shown in Section 6.7.2. The contours in the Figures are intended to be indicative of the beam quality, being one quarter, half and three quarters of the beam peak intensity.

(a) Uncorrected   (b) Corrected
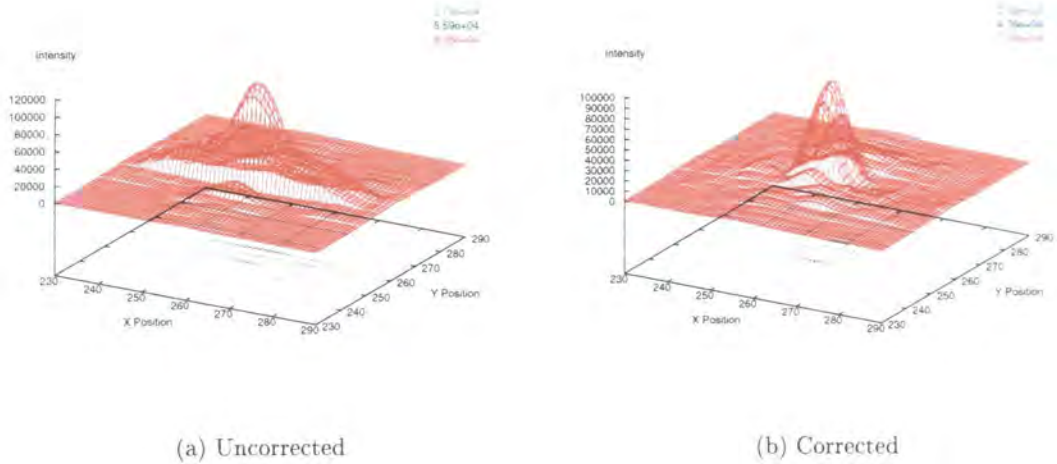
Figure 6.19: Point-spread functions for biased membrane.

Corrected results after 3 iterations through feedback loop. The intensity scale is arbitrary.

The first test for the simulated AO system is to correct the aberrations integral to the biased membrane. Figure 6.19a shows the point spread function of the MMDM, and clearly shows the presence of some astigmatism. Figure 6.19b shows the corrected point spread function. The main point of interest is that, although the contours are closer together, and better centralised on $(x=260, y=261)$[1] , the peak intensity is actually reduced. This demonstrates that the Strehl ratio, being a measure from the peak intensity, does not give a full description of a beam profile, or quality of AO loop correction. However, since Strehl ratios are the most common measure of beam correction, they will be shown in Section 6.7.2. The main indication that the AO loop has improved the beam quality is that the stretched-out point spread function, indicative of astigmatism, present in the uncorrected Figure, has been almost completely eliminated in the corrected figure. Note that, for the following Figures showing correction of external aberrations, the initial surface figure of the MMDM remains as the aberrated figure, rather than the corrected figure.

---

[1]The location of the optimal peak intensity was obtained from the perfect system point spread function in Figure 6.18.

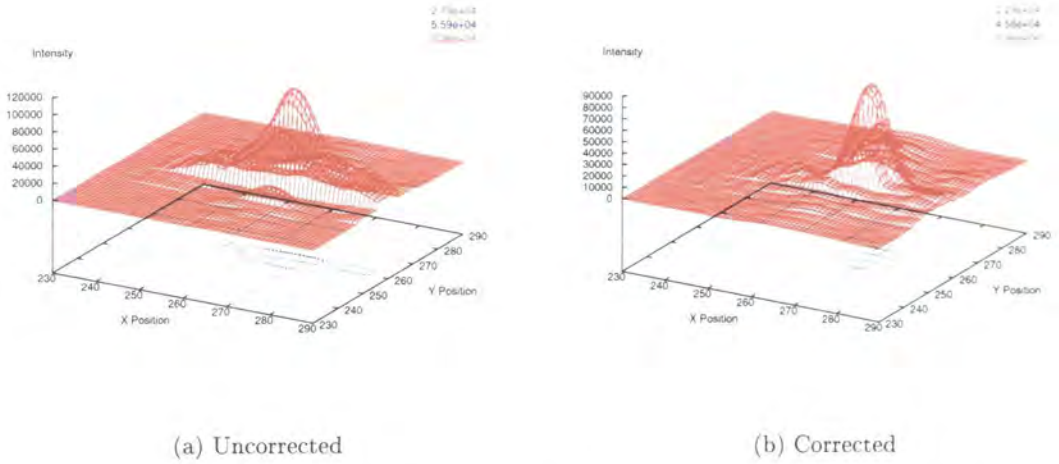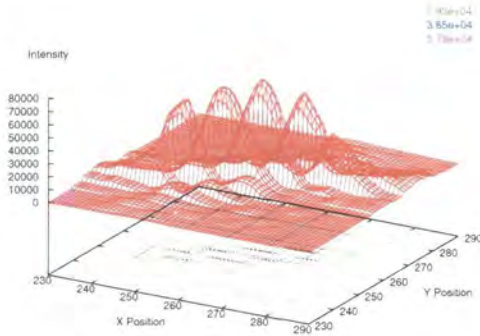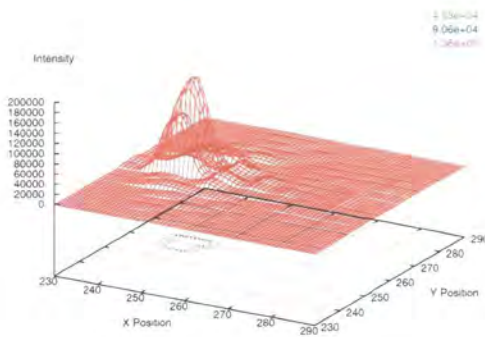(a) Uncorrected   (b) Corrected
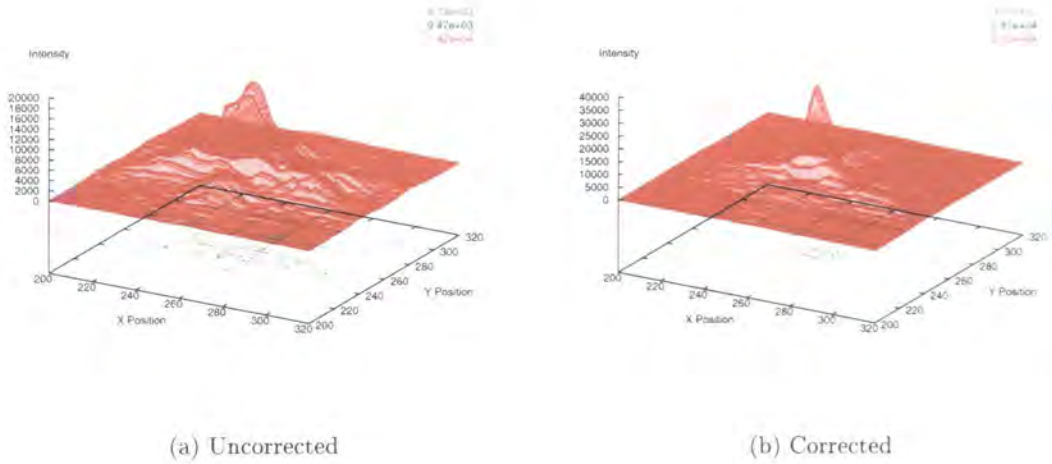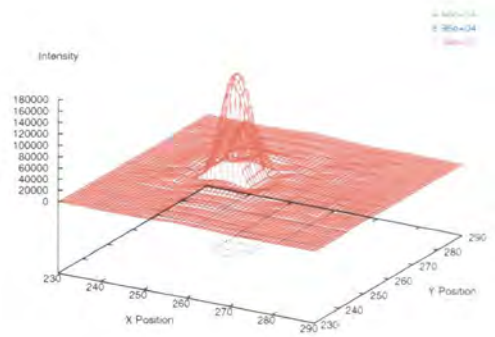
Figure 6.20: Point-spread functions for application of 8 radians of Defocus.
Corrected results after 3 iterations through feedback loop. The intensity scale is
arbitrary.

The uncorrected point spread function for defocus is shown in Figure 6.20a, with the
corrected beam after three iterations of the feedback loop in Figure 6.20b. Note that the
hexagonal structure from the MMDM actuators is apparent in the point spread function.
This may be due to the way in which the MMDM surface is constructed, with the 37
individual influence functions being averaged together, which results in a certain amount
of print through in the theoretical membrane. This is smoothed out in the real device.
The corrected point spread function is again much more compact than the uncorrected.
This time, however, the peak intensity is also substantially improved.

Figure 6.21 shows the uncorrected and corrected point spread functions for the ap-
plication of 8 radians of spherical aberration. The structure in the uncorrected point
spread function is interesting. The structure may be an artefact of the simulation, arising
from the interaction between the sphercial aberration and any print through present in
the theoretically generated membrane. It is clear in Figure 6.2 that there is a hexago-
nal structure present in the theoretical membrane. Whether this structure can cause a
result as complex as that observed for the uncorrected spherical aberration is not clear.
The corrected peak intensity is marginally off-axis, by 1 pixel in each direction. This
corresponds to a displacement of under 60μm, and so is not considered to be significant.

The results for tip are unusual, and are shown in Figure 6.22. The peak intensity
actually moves further from the center of the detector after correction. Further iterations
through the feedback loop cause the peak intensity to progressively track further from

(a) Uncorrected   (b) Corrected
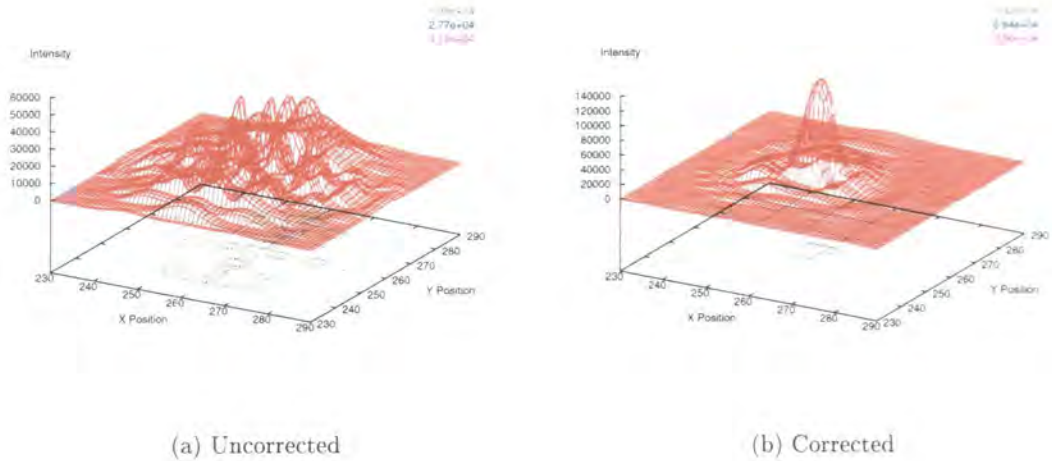
Figure 6.21: Point-spread functions for application of 8 radians of Spherical Aberration. Corrected results after 3 iterations through feedback loop. The intensity scale is arbitrary.

the center of the detector. Hence, were this simulated system to be constructed, it would be necessary to ensure that tip-tilt correction was handled by some other means, such as a dedicated tip-tilt mirror. It is known that MMDMs are inefficient tip-tilt correctors, so a separate tip-tilt corrector is likely to be implemented regardless of wavefront sensor choice (Vdovin et al. 1999). Note that the beam shape is still improved for tip, despite the peak intensity moving off-axis.

In the case of astigmatism, illustrated in Figure 6.23, the beam shape is improved, but some residual astigmatism is still present. Since the predominant aberration inherent to the MMDM is astigmatism, and the correction for this worked well in Figure 6.19, this result is a little surprising. Subsequent iterations through the feedback loop did reduce this residual astigmatism to negligible levels, however, three iterations have been shown to give good wavefront correction using an MMDM, Shack-Hartmann wavefront sensor and full wavefront reconstruction (Vdovin et al. 1999). Hence, the results here are shown after the same number of iterations for comparison.

Uncorrected coma shows some beam shape degradation in Figure 6.24a, however, the most significant effect is moving the peak intensity off-axis. The corrected beam, in Figure 6.24b shows that, unlike tip, this deviation from the axis is at least partially corrected. The point spread function is also improved, becoming more compact.

To summarise the performance of the AO loop system in improving the point spread function for the application of 8 radians of the low-order Zernike aberrations, good correc-

(a) Uncorrected   (b) Corrected

Figure 6.22: Point-spread functions for application of 8 radians of Tip. Corrected results after 3 iterations through feedback loop. The intensity scale is arbitrary.

tion is achieved for defocus, spherical aberration and coma. Some correction is observed for astigmatism, while tip is amplified, rather than corrected.

(a) Uncorrected
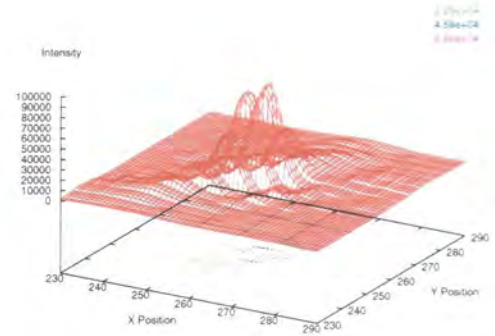
(b) Corrected

Figure 6.23: Point-spread functions for application of 8 radians of Astigmatism. Corrected results after 3 iterations through feedback loop. The intensity scale is arbitrary.

(a) Uncorrected

(b) Corrected

Figure 6.24: Point-spread functions for application of 8 radians of Coma. Corrected results after 3 iterations through feedback loop. The intensity scale is arbitrary.

6.7.2 Strehl Ratios and Beam Statistics

The peak intensities and normalised Strehl ratios for the application of 4, 8 and 12 radians of low-order Zernike aberrations are shown in Table 6.4, along with the Strehl ratios after three iterations through the feedback loop.

Considering the first case, that of the inherent aberrations in the system, the Strehl ratio for the corrected system is reduced from that of the uncorrected system. However, it is clear from the contour plots shown in Figure 6.19 that the astigmatism has been reduced. This is indicative of the Strehl ratio, by being a simple measure of peak intensity, not being a perfect measure of beam quality. Strehl ratios are still presented here, since Strehl ratios are a standard measure of wavefront correction. The contours in the Figures in Section 6.7.1 are more accurate measures of the beam quality. Hence the Table includes the area, in pixels (each pixel is a square of side 60μm), of the contours at one quarter, half and three quarters peak beam intensity. Note that, for the cases where there are multiple peaks within a contour, such as in Figure 6.21, the area is the total area of all of the peaks. The contour areas are not independent of the peak intensity, and hence are not independent of the Strehl ratio. As the peak intensity drops, the quarter, half and 3 quarters intensity also drops, and hence the number of pixels over these thresholds increases.

It is notable that, in the case of Coma, the Strehl ratio increases and the area within each contour decreases as the amplitude of the aberration applied goes from 4 radians to 8 radians. This suggests that the coma is cancelling out some of the initial aberrations in the system.

The contour areas are a better measure of beam correction than the simple Strehl ratio, particularly when all three are taken into consideration, as this gives some idea of the three-dimensional structure of the point-spread function. The smaller the area in a given contour, the better the beam correction. The advantage of the contour areas for determining the point spread function structure is clearly illustrated for the case of 8 radians of spherical aberration. Here, the quarter and half maximum contours are dramatically reduced (by factors of 6.6 and 2 respectively), but the 3 quarter maximum contour is larger. This indicates that the beam correction is predominantly in the fringes of the point spread function.

The best corrections observed with this system are observed when correcting spherical aberration and defocus. Note that for coma and tip, the most obvious effect observed in

Figures 6.24 and 6.22 was to move the point spread function, rather than distort it. This is not effectively measured by either the Strehl ratio or the contour area data.

However, over-correction may still be present in the system, as the system does not give good correction for the application of small amplitude aberrations. For the 3 quarters maximum intensity contour, that is correction of the parts of the wavefront that are already near-perfect, the area increases for the correction of some aberrations. This lends further credence to the idea that the feedback loop may be overcorrecting. This effect is most prominent for 4 radians of astigmatism, which yields an increase in the area of the 3 quarter maximum intensity contour by a factor of 2.4. Similarly, the area of this contour is increased by a factor of 2 for spherical aberration at 4 radians, and by a factor of 1.5 for the application of 8 radians of spherical aberration. This overcorrection is quite likely to be caused, at least in part, by the 8-bit digitisation of the theoretical actuator influence functions. This 8-bit digitisation limitation also applies to the electronics provided with the real MMDMs, so may be a factor in a real system.

However, for the areas of the half and quarter maximum intensity contours, where the larger wavefront deviations are being corrected, the system performs well. Considering the case of the one quarter maximum contour, a reduction in the area by a factor of 6.6 is observed for the application of 8 radians of spherical aberration. An improvement by a factor of 3.5 is observed for 8 radians of defocus, and 1.8 for astigmtatism. Coma actually deteriorates in this contour, for the application of 8 or 12 radians of aberration, albeit marginally. However, it was shown through the point spread functions that the main effect of coma was to move the peak intensity off-axis, which was corrected, while the beam shape was not dramatically deformed. The half maximum intensity contour shows an improvement for coma of a factor of 1.8 for the application of 12 radians of aberration. Hence, for coma, it can be concluded that the small wavefront deviations are over-corrected, the large ones uncorrected, but the intermediate deviations are well-corrected. The area of the half maximum intensity contour is reduced by a factor of about 2 for each of the remaining aberrations, at an amplitude of 8 radians. A dramatic improvement is observed for 12 radians of spherical aberration, with a reduction in the area of the half maximum intensity contour, by a factor of 4. Hence, it has been shown that the simulated system gives good correction for defocus and spherical aberration and reasonable correction for astigmatism.

Aberration	Peak Intensity (Arbitrary Scale)	Strehl Ratio	FWQM	FWHM	FW3QM
Perfect System	7.832009e+05		28	20	10
None	1.117109e+05	0.143	200	77	29
None (Corrected)	9.529071e+04	0.122	126	77	34
Astigmatism (4 radians)	1.040995e+05	0.133	189	95	42
Astigmatism (Corrected)	2.618753e+04	0.033	714	242	99
Astigmatism (8 radians)	7.701376e+04	0.098	278	148	67
Astigmatism (Corrected)	9.152752e+04	0.117	153	73	34
Astigmatism (12 radians)	6.017339e+04	0.077	459	155	51
Astigmatism (Corrected)	6.636551e+04	0.085	274	115	42
Coma (4 radians)	1.409462e+05	0.180	120	68	25
Coma (Corrected)	1.289612e+05	0.165	111	52	23
Coma (8 radians)	1.811965e+05	0.231	78	56	20
Coma (Corrected)	1.792808e+05	0.229	88	38	19
Coma (12 radians)	1.675440e+05	0.214	75	51	19
Coma (Corrected)	1.756008e+05	0.224	79	28	20
Defocus (4 radians)	3.760683e+04	0.048	557	149	103
Defocus (Corrected)	5.752399e+04	0.073	175	68	35
Defocus (8 radians)	1.893285e+04	0.024	944	241	109
Defocus (Corrected)	3.628216e+04	0.046	267	101	27
Defocus (12 radians)	9.306946e+03	0.012	2767	566	135
Defocus (Corrected)	1.386025e+04	0.018	1224	347	47
Spherical (4 radians)	1.580896e+05	0.202	114	44	16
Spherical (Corrected)	1.306044e+05	0.167	80	52	33
Spherical (8 radians)	5.548252e+04	0.071	430	79	12
Spherical (Corrected)	1.328583e+05	0.170	65	40	19
Spherical (12 radians)	2.920867e+04	0.037	610	98	20
Spherical (Corrected)	7.421476e+04	0.095	249	24	15

Table 6.4: Peak intensities and Strehl ratios for aberrated and corrected wavefronts. Perfect beam uses lens instead of MMDM. None shows AO loop performance for correcting aberrations inherent in the simulated MMDM surface. Amplitude of aberration applied shown in parentheses. FWQM, FWHM and FW3QM are the areas, in pixels, of the intensities above the quarter, half and three quarter peak intensities respectively.

Aberration	Peak Intensity (Arbitrary Scale)	Strehl Ratio	FWQM	FWHM	FW3QM
Tip (4 radians)	1.114212e+05	0.142	203	79	30
Tip (Corrected)	9.183153e+04	0.117	124	70	23
Tip (8 radians)	1.117576e+05	0.143	196	79	29
Tip (Corrected)	8.806417e+04	0.112	130	68	24
Tip (12 radians)	1.114176e+05	0.142	197	79	30
Tip (Corrected)	9.881158e+04	0.126	125	60	20

Table 6.5: Peak intensities and Strehl ratios for wavefronts with tip applied. Amplitude of tip applied shown in parentheses. FWQM, FWHM and FW3QM are the areas, in pixels, of the intensities above the quarter, half and three quarter peak intensities respectively.

6.8 Conclusions

In this Chapter, the principles of an adaptive optics system utilising a curvature wavefront sensor in conjunction with an MMDM have been explored. A simulated system has been developed, with some comments as to the areas of the simulation that would need to be altered for a practical, physical system. This system has then been fine-tuned, identifying the optimum beam radius of 5.0mm and extra-focal distance of 600mm. The wavefront sensor subaperture responses to poking each individual actuator has been measured, along with the responses to low-order Zernike aberrations. These have been combined to correct the aberrations. The correction of the integral aberrations in the simulated MMDM has been demonstrated, by examining the point spread functions of the initial MMDM and the beam after three iterations through the feedback loop. For the application of pure tip to the system, an amplification of the movement of the peak intensity in the point spread function was observed. Hence, for a system designed to use an MMDM and curvature sensor without wavefront reconstruction, a separate tip-tilt correction device would also be required. Strehl ratios have also been presented, along with some caveats as to their interpretation.

An alternative means to measure the beam quality was presented, by examining the area of intensities over one quarter, half and three quarters peak intensity. It is shown that the system may be over-correcting small aberrations, both by examining the area within the three-quarters maximum intensity contour, and examing the results for the application of small aberrations. This may be due to the 8-bit digitisation in the generation of the influence functions; similar digitisation is present in the control electronics for the real MMDMs. Using the areas in the quarter and half maximum intensity contours, it was shown that the system gives best correction for spherical aberration and defocus. The area within the quarter maximum intensity contour is reduced by a factor of 6.6 for the correction of 8 radians of spherical aberration, and 3.5 for the application of 8 radians of defocus.

Hence, it has been shown that the simulated system gives good correction for defocus and spherical aberration and reasonable correction for astigmatism. Coupled with the obsevation of the movement of the peak intensity directly from the point spread functions, coma can be added to the list of well-corrected aberrations.

This simulation has been demonstrated to correct low order Zernike aberrations. The simulation is applicable to both room temperature and cryogenic operation of the

MMDMs; the only change required to more closely examine a particular case, such as a different radius MMDM, is to adjust the influence functions of the MMDM and repeat the calibration steps. The case examined has used influence functions with the same magnitude as the room temperature influence functions. The extension to the cryogenic case would require adjusting the magnitudes of these influence functions, and would reduce the magnitudes of the aberrations that can be corrected. However, since this is a proof-of-concept system, and not a model of a physical system, this was deemed unnecessary. By removing the wavefront reconstruction step, it also points the way to a system where the wavefront correction is performed through simple electronics, possibly even mounted on the same silicon wafer as the MMDM.

Chapter 7

Conclusions

In this Thesis, the application of Micromachined Membrane Deformable Mirrors (MMDMs) to cryogenic adaptive optics has been explored. In particular, three questions have been examined:

- How can MMDMs be cooled to cryogenic temperatures, and do they survive the process?

- What is the effect on the MMDMs properties of operating them in a vacuum and at low temperature.

- Is it feasible to perform wavefront correction using an MMDM and a curvature wavefront sensor without performing an explicit wavefront reconstruction. This final question was not specific to cryogenic adaptive optics, but applied equally to room temperature and cryogenic adaptive optics.

7.1 MMDM Cooling

The initial system for cooling an MMDM was described in Chapter 3. This original system was used to cool the MMDM to a temperature of 126K, a temperature determined by the use of diodes as thermometers. A model was then constructed to investigate why the MMDM was not reaching a lower temperature. It was shown that the initial method of cooling, by conducting the heat away from the MMDM was not as efficient as preventing the energy from reaching the MMDM in the first place. Therefore, a re-designed mount was developed which utilised a filter to block incoming thermal radiation from reaching the MMDM. As a consequence of this, it was no longer necessary to conduct energy away from the MMDM. Since there was no longer any material attached to the MMDM, a method of remotely sensing the MMDM temperature was developed and verified. Finally, it was experimentally determined that the re-designed mount led to the MMDM being cooled to, and surviving, a temperature of 80K.

152

7.2   MMDM Static Properties

A method for measuring the surface of the reflective membrane of the MMDM was outlined in Chapter 4, which utilised a Zygo PTI phase shifting interferometer. Using this, the variation in the aberrations inherent in the membrane surface with changing temperature was analysed. In a sample of three MMDMs, one (identified as MMDM A) had substantially better performance than the other two. Each MMDM had less than 1λ (λ=633.9nm) of aberrations, predominantly astigmatism, at room temperature. Upon cooling the MMDMs to 78K, MMDM A showed under 5λ of astigmatism, with a negligible increase in the other Seidel aberrations. The remaining two MMDMs developed approximately 10λ of aberrations in total, with varying magnitudes of each aberration. The effect of cooling the devices on the initial surface figure was further illustrated through the use of phase maps. In the case of the first MMDM, the aberrations introduced by cooling are well within the dynamic range of the MMDM.

The influence functions of each actuator for each MMDM were then examined qualitatively through the use of phase maps. Subsequently, a selection of influence functions were quantitatively examined by exploring the cross-sections of the influence functions. The first question to be explored was to determine the variation in the influence function with the azimuthal position of an actuator. This was necessary to establish the validity of examining a subset of the actuators. It was determined that the azimuthal position had a negligible effect on the shape of an influence function, but did alter the magnitude. The second question to be examined was the effect of evacuating the dewar on the influence functions. Evacuation was determined to have no effect on the influence functions of an MMDM. The final question was to assess the effect of cryogenically cooling an MMDM on the influence functions. It was determined that the shape of the influence functions remained the same at 78K, but the magnitude was reduced by 20%. It should be noted that this is the first demonstration of a wavefront corrector functioning at 78K.

7.3   MMDM Dynamic Properties

A method has been developed in Chapter 5 to measure the dynamic response of an MMDM, for driving frequencies of up to 500Hz. It has been shown that evacuating the dewar has no effect on the dynamic properties of all three MMDMs tested, within measurement limits. It was determined that all three MMDMs were suitable for room temperature operation as wavefront correctors, using the supplied electronics, at frequen-

cies up to 250Hz. Evacuation was found to have no effect on the dynamic response of the MMDMs, which demonstrates that the most significant damping force on the membrane was the membrane tension, rather than air damping. Faster driving electronics would be required for evaluating higher frequency operation. Upon cooling the MMDMs, a high frequency ringing (2kHz) was observed. This effect was much more prominent for MMDMs B and C, compared to MMDM A. It is unclear as to whether this is connected to the increased aberrations inherent in the membrane surface for MMDMs B and C. However, since MMDM A was from a different batch to B and C, it does raise the prospect that the MMDM design could be optimised for cryogenic operation. If the dynamic response is connected to the static properties, then there is only one degree of optimisation required. If, however, the dynamic response and static properties are independent, then a trade-off may need to be made between the two performance characteristics. The high frequency ringing for MMDMs B and C was too substantial for them to be considered for operation at 78K. MMDM A was found to have a suitable dynamic response at 78K to perform as a wavefront corrector. Hence, not only are MMDMs the first adaptive optical element to have been deomnstrated to work at 78K, but they also function at sufficiently high frequencies to be considered to be useful for a practical AO system.

7.4   Simulation of an AO System Using MMDMs as a Wavefront Corrector

A simulated AO system has been constructed in Chapter 6, utilising an MMDM as a wavefront corrector, and a curvature sensor as a wavefront sensor. This system demonstrated that it is feasible to correct a wavefront with a MMDM and curvature sensor without reconstructing the wavefront. A novel technique for determining the wavefront sensor subapertures was described, which could be applied in a real system to any pixellated detector, such as a CCD. The system was then tuned, using the pre-determined subapertures, to an optimum beam diameter and extra-focal distance for the two detector planes. The wavefront sensor response to driving each actuator in turn was evaluated, along with the response to the low-order Zernike aberrations. Combining these led to wavefront correction being demonstrated, through the presentation of point spread functions and Strehl ratios. The reasons why the point spread functions are a better indication of beam quality than the Strehl ratio were also discussed. The system could not correct tip, but instead amplified it, thus highlighting the need for a separate tip-tilt correction system.

In addition, astigmatism was not as well corrected as had been hoped. However, good correction was demonstrated for defocus, spherical aberration and coma. This simulated system lays the foundations for a simple, rapid and low-cost adaptive optics system.

7.5   Future Work

The most significant avenue for further exploration is that of MMDM optimisation for operation at cryogenic temperatures. Particular encouragement can be gained from the fact that, of the sample of 3 MMDMs, 1 had substantially better performance than the other 2. Since this one was from a separate batch, it is likely that certain parameters, such as membrane thickness, differed from this device to the other 2, both of which were from the same batch. As these parameters for the specific devices tested are no longer available, future projects studying MMDMs at cryogenic temperatures need to obtain as much information about the manufacturing parameters as possible for the devices being tested. The key area of investigation should be whether the dynamic response of an MMDM is related to the static aberrations caused by cooling. It would greatly simplify the optimisation process if they were indeed linked.

A second area of further investigation is to determine how much of the aberrations introduced to the membrane surface by the cooling process is due to edge effects, and how much to the coefficient of thermal expansion mismatch between the Silicon Nitride membrane and the reflective surface. This can be explored in two ways; firstly, through using alternative reflective coatings, and secondly by using larger devices, such that the edge effects should not be prominent near the center of the device.

The simulated system can also be extended. Three potential areas for improvement are available. Firstly, if the systematic Zygo noise can be removed from the experimentally measured influence functions, then it will be possible to use the physical influence functions in the simulated system. The second avenue is to implement the measured dynamic response of the MMDMs to correct time-varying aberrations. The third avenue is to compare the wavefront correction without explicit reconstruction with that achieved by reconstructing the wavefront. It may also be useful to compare a curvature sensor (with or without wavefront reconstruction) to other wavefront sensors, such as a Shack-Hartmann sensor.

This Thesis has described the first steps towards the application of MMDMs to the field of cryogenic adaptive optics. The results of this work have been positive, identifying

one MMDM from a sample of three that has characteristics consistent with being a viable wavefront corrector at cryogenic temperatures. Perhaps the largest remaining hurdle is to demonstrate the feasibility of optimising the design of MMDMs for cryogenic operation; all the results included herein are for devices optimised for room temperature operation. The prospect of a functioning cryogenic adaptive optics system is now within reach.

Appendix A

Response of Simulated Curvature Wavefront Sensor to each Individual Actuator
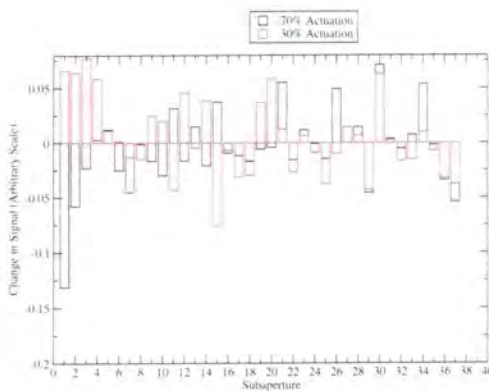
(a) Actuator 1
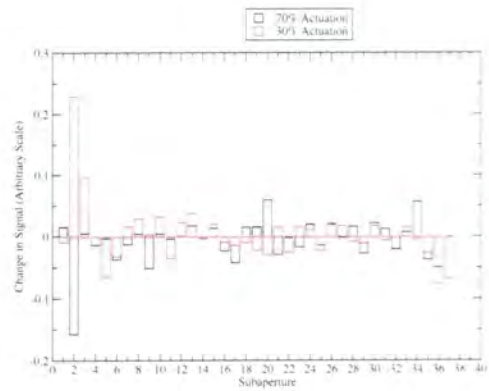
(b) Actuator 2
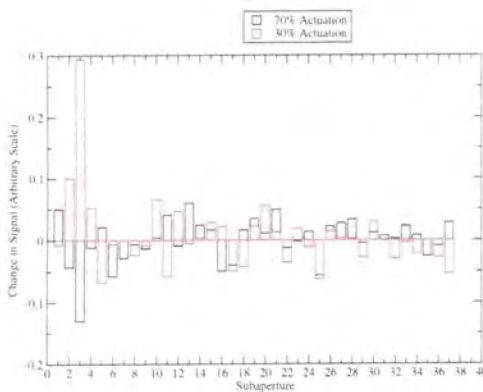
(c) Actuator 3
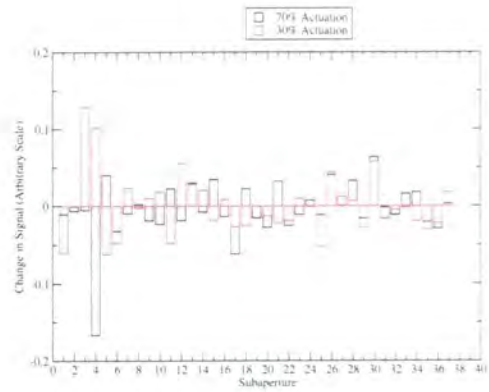
(d) Actuator 4

Figure A.1: Response of wavefront sensor to poking actuators 1 to 4.
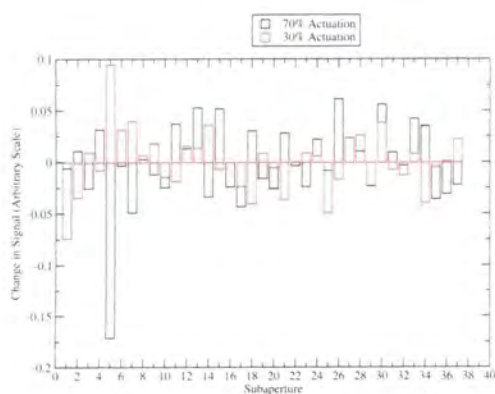
(a) Actuator 5
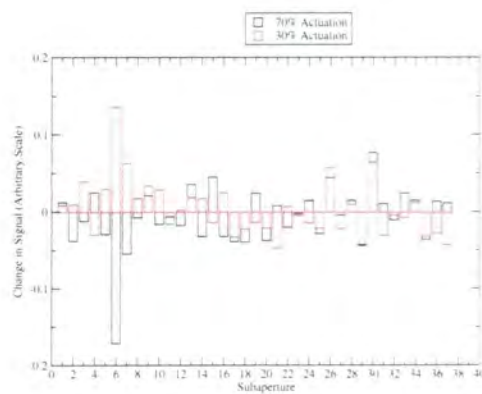
(b) Actuator 6
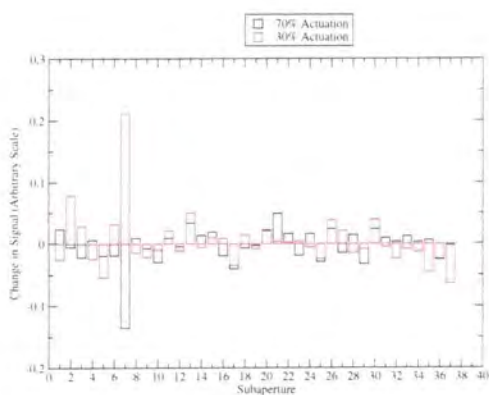
(c) Actuator 7
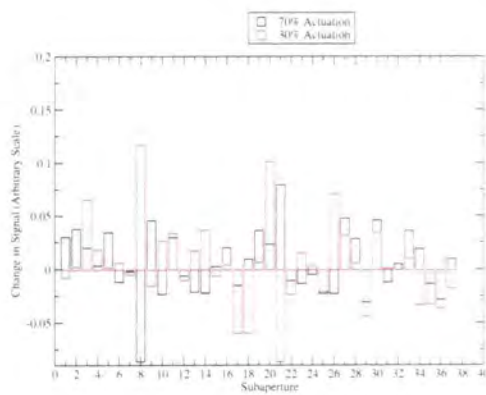
(d) Actuator 8
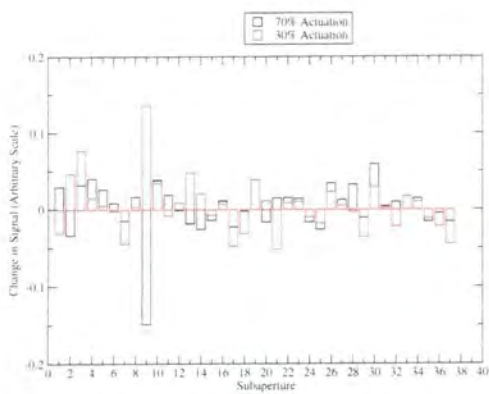
(e) Actuator 9
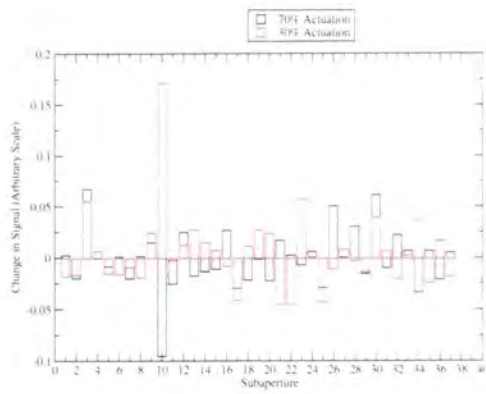
(f) Actuator 10

Figure A.2: Response of wavefront sensor to poking actuators 5 to 10.
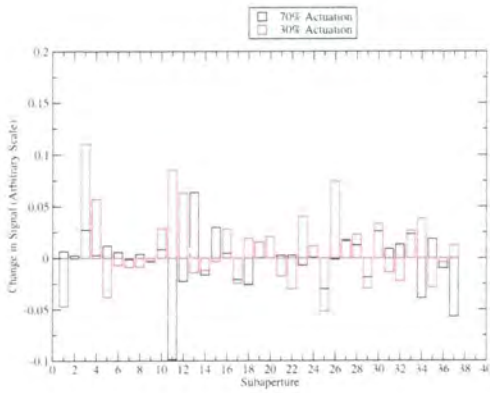
(a) Actuator 11
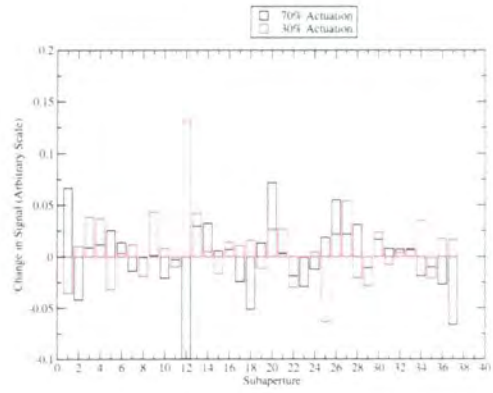
(b) Actuator 12
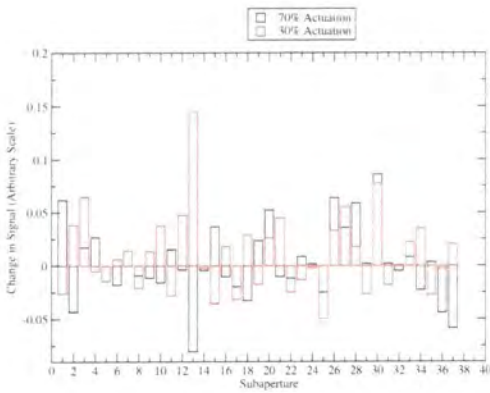
(c) Actuator 13
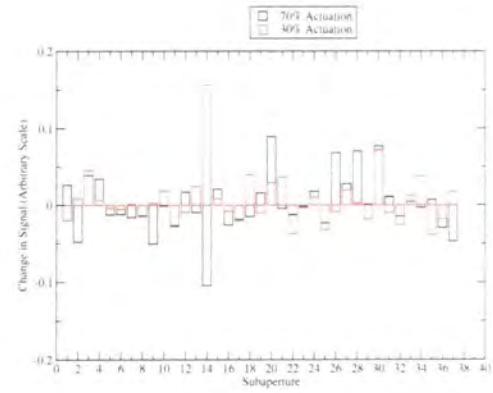
(d) Actuator 14
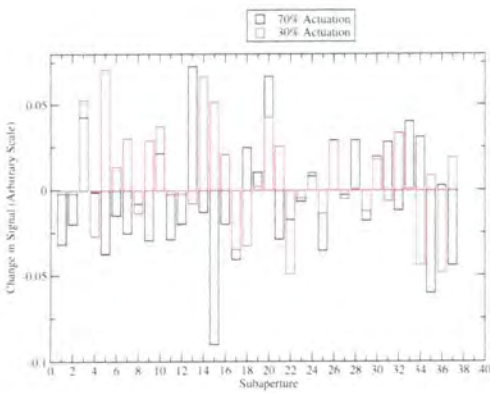
(e) Actuator 15
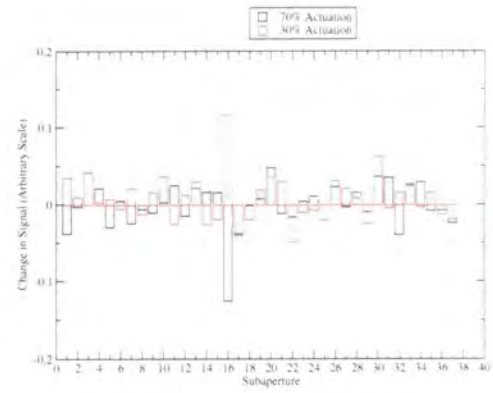
(f) Actuator 16

Figure A.3: Response of wavefront sensor to poking actuators 11 to 16.
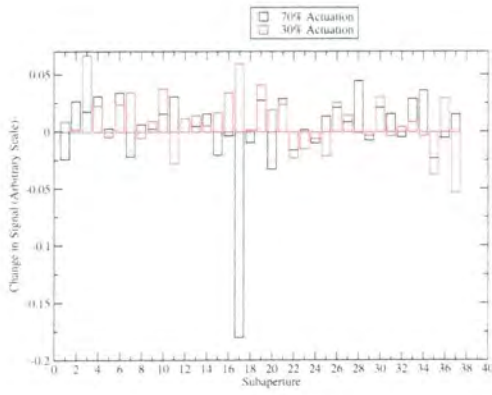
(a) Actuator 17
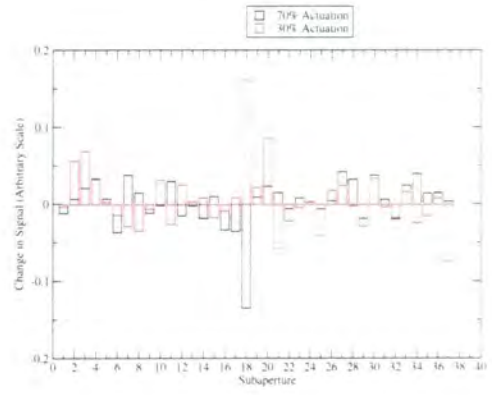
(b) Actuator 18
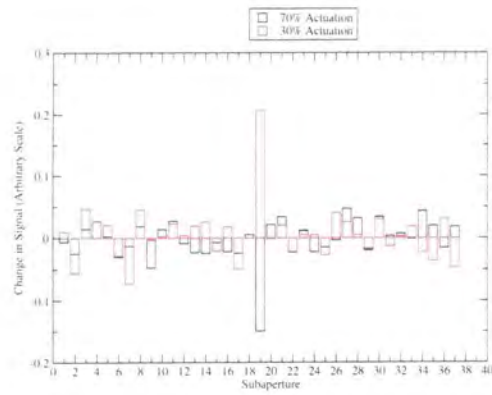
(c) Actuator 19
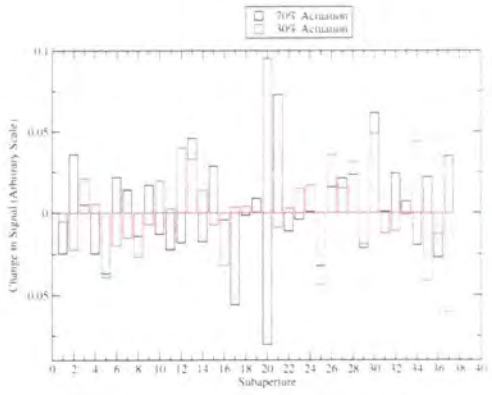
(d) Actuator 20
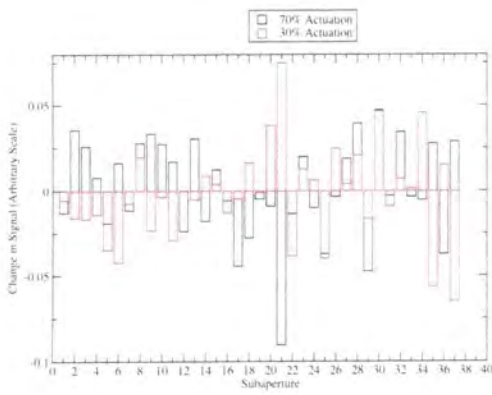
(e) Actuator 21
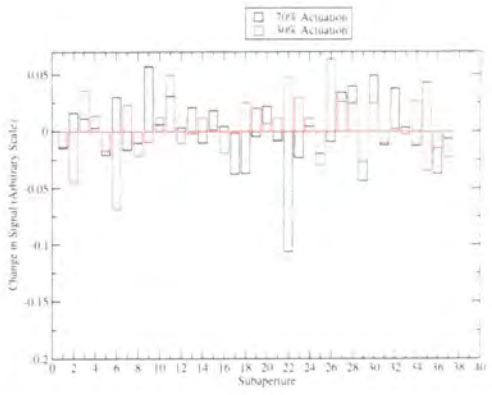
(f) Actuator 22

Figure A.4: Response of wavefront sensor to poking actuators 17 to 22.
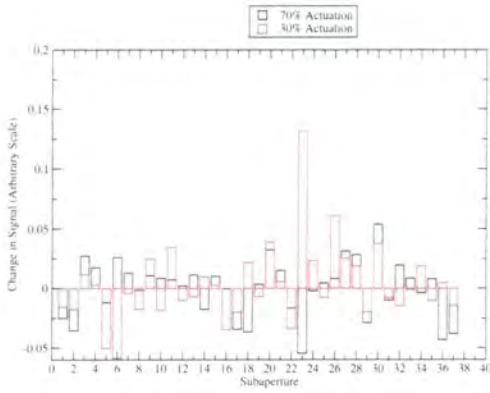
(a) Actuator 23
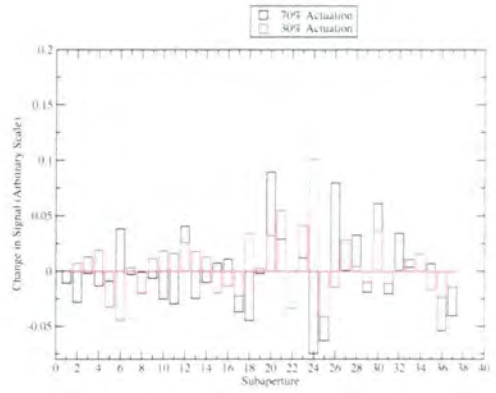
(b) Actuator 24
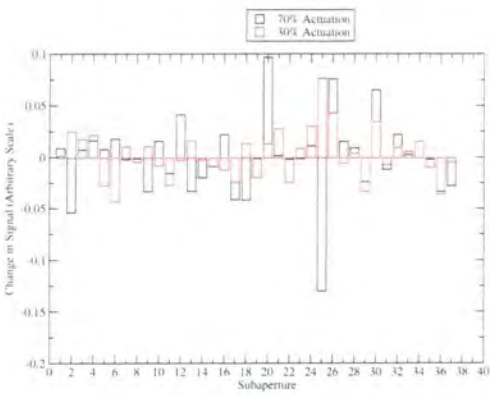
(c) Actuator 25
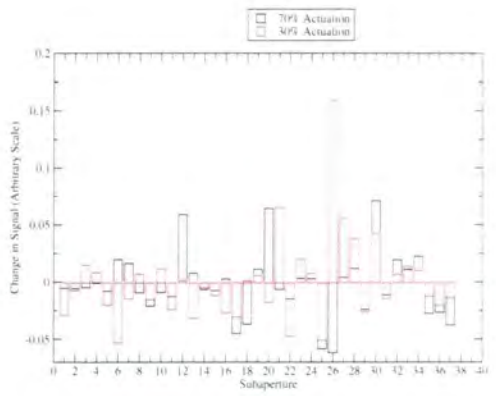
(d) Actuator 26
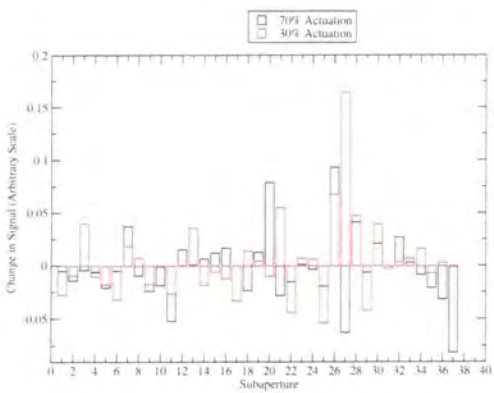
(e) Actuator 27
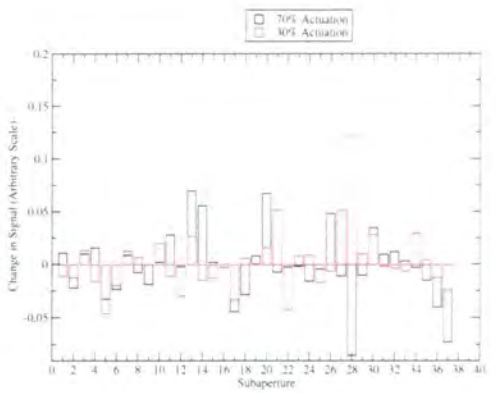
(f) Actuator 28

Figure A.5: Response of wavefront sensor to poking actuators 23 to 28.
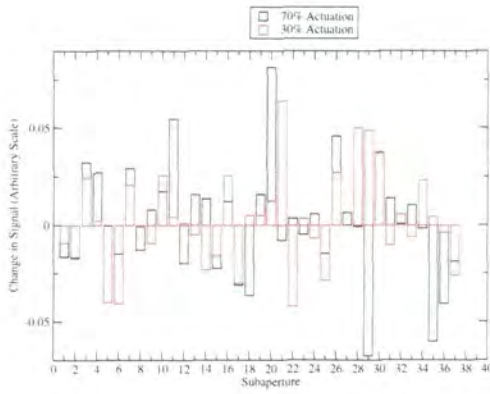
(a) Actuator 29
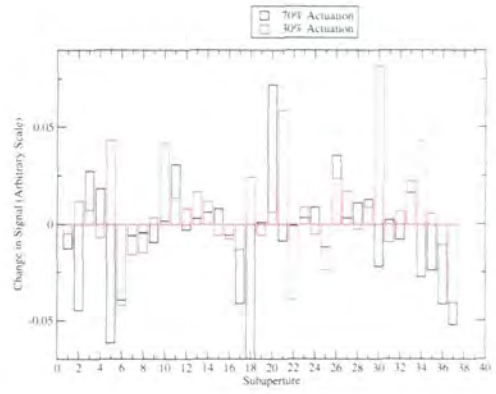
(b) Actuator 30
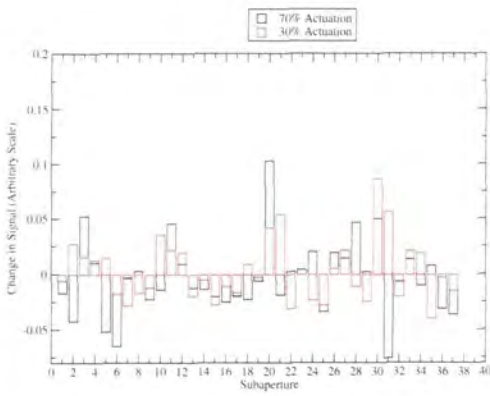
(c) Actuator 31
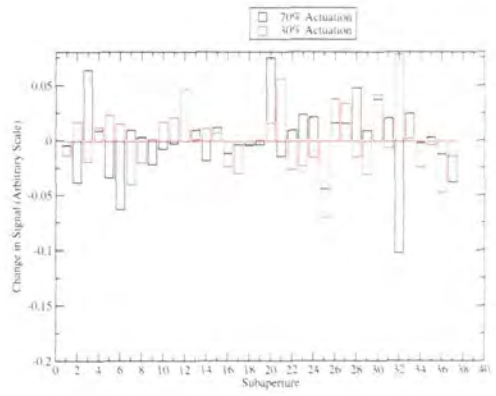
(d) Actuator 32
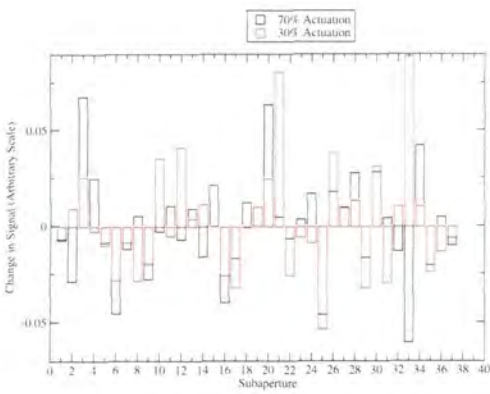
(e) Actuator 33
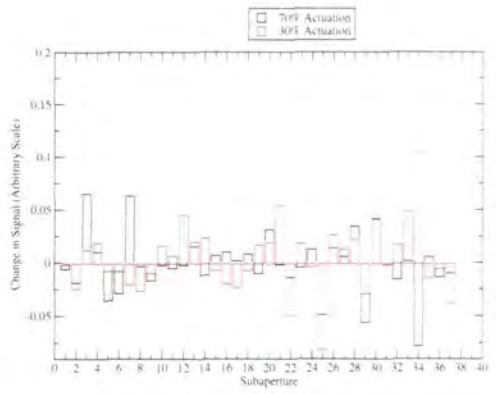
(f) Actuator 34

Figure A.6: Response of wavefront sensor to poking actuators 29 to 34.
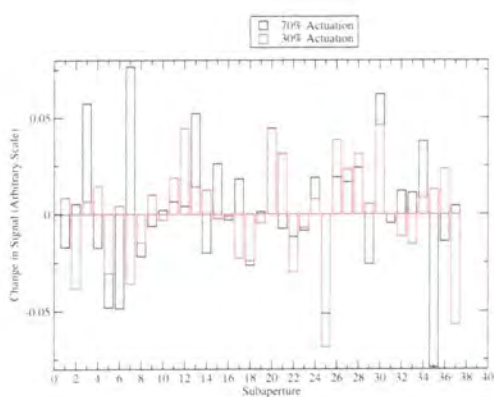
(a) Actuator 35
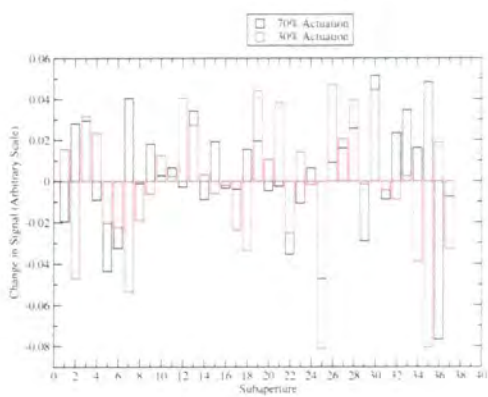
(b) Actuator 36
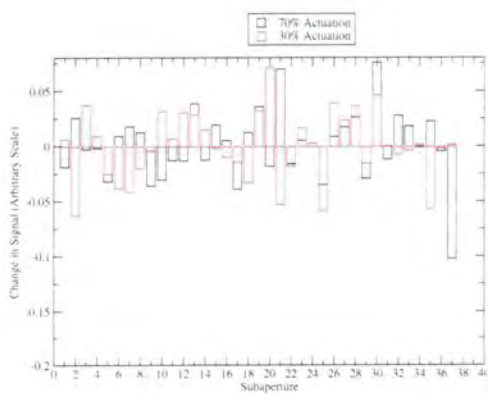
(c) Actuator 37

Figure A.7: Response of wavefront sensor to poking actuators 35 to 37.

Bibliography

Andersen, T., Owner-Petersen, M. and Gontcharov, A.: 2001, Concepts for dual conjugate adaptive optics for the swedish 50 m extremely large telescope, <u>Beyond Conventional Adaptive Optics</u>.
URL: *http://nastol.astro.lu.se/ torben/50m/torben-venice.pdf*

Angel, J. R. P.: 1994, Ground-based imaging of extrasolar planets using adaptive optics, <u>Nature</u> **368**, 203–207.

Angel, J. R. P., Burge, J. H., Hege, E. K., Kenworthy, M. A. and Woolf, N. J.: 2000, Stretched membrane with electrostatic curvature (SMEC): a new technology for ultralightweight space telescopes, <u>Proc. SPIE Vol. 4013, p. 699-705, UV, Optical, and IR Space Telescopes and Instruments, James B. Breckinridge; Peter Jakobsen; Eds.,</u> Vol. 4013, pp. 699–705.
URL: *http://ukads.nottingham.ac.uk/cgi-bin/nph-bib_query?bibcode= 2000SPIE.4013..699A&db_key=AST*

Babcock, H. W.: 1953, The Possibility of Compensating Astronomical Seeing, <u>Publications of the Astronomical Society of the Pacific</u> **65**, 229+.
URL: *http://ukads.nottingham.ac.uk/cgi-bin/nph-bib_query?bibcode= 1953PASP...65..229B&db_key=AST*

Benn, C., Longmore, A., Myers, R., Gregory, T. and Davenhall, C.: 2001, NAOMI - Adaptive Optics at the WHT, <u>The Newsletter of the Isaac Newton Group of Telescopes (ING Newsl.), issue no. 4, p. 21-22</u> **4**, 21–22.
URL: *http://ukads.nottingham.ac.uk/cgi-bin/nph-bib_query?bibcode= 2001INGN....4...21B&db_key=AST*

Benn, C. R.: 2001, Adaptive optics at the WHT, <u>New Astronomy Review</u> **45**, 59–62.
  URL: *http://ukads.nottingham.ac.uk/cgi-bin/nph-bib_query?bibcode=*
  2001NewAR..45...59B&db_key=AST

Bifano, T. G., Krishnamoorthy Mali, R., Dorton, J. K., Perreault, J., Vandelli, N.,
  Horenstein, M. N. and Castanon, D. A.: 1997, Continuous-membrane surface-
  micromachined silicon deformable mirror, <u>Optical Engineering</u> **36**, 1354–1360.
  URL: *http://ukads.nottingham.ac.uk/cgi-bin/nph-bib_query?bibcode=*
  1997OptEn..36.1354B&db_key=INST

Bifano, T. G., Perreault, J., Krishnamoorthy Mali, R. and Horenstein, M. N.: 1999,
  Microeletromechanical deformable mirrors, <u>IEEE Journal on Selected Topics in
  Quantum Electronics</u> **5**(1).

Bold, G. T., Barnes, T. H., Gourlay, J., Sharples, R. M. and Haskell, T. G.: 1998,
  Practical issues for the use of liquid crystal spatial light modulators in adaptive
  optics, <u>Optics Communications</u> **148**, 323–330.
  URL: *http://ukads.nottingham.ac.uk/cgi-bin/nph-bib_query?bibcode=*
  1998OptCo.148..323B&db_key=INST

Bonicel, S. L.: 1999, <u>Micro-deformable mirrors: a low cost technology for cryogenic active
  and adaptive optics</u>, Master's thesis, University of Durham.

Born, M. and Wolf, E.: 1980, <u>Principles of optics. Electromagnetic theory of propagation, interfere</u>
  Oxford: Pergamon Press, 1980, 6th corrected ed.
  URL: *http://ukads.nottingham.ac.uk/cgi-bin/nph-bib_query?bibcode=*
  1980poet.book.....B&db_key=AST

Boyer, C. and Gaffard, J.: 1991, Adaptive optics, transfer loops modeling, <u>Active and
  adaptive optical systems; Proceedings of the Meeting, San Diego, CA, July 22-24,
  1991 (A93-39451 15-74), p. 46-61.</u>, Vol. 1542, pp. 46–61.
  URL: *http://ukads.nottingham.ac.uk/cgi-bin/nph-bib_query?bibcode=*
  1991SPIE.1542...46B&db_key=AST

Bresee, L. D.: 1999.
  URL: *http://www.ucolick.org/ lance/diodes/diodes.html*

Burley, G. S., Walker, G. A. H. and Johnson, R.: 1998, A Versatile CCD Wave Front Cur-
  vature Sensor, <u>Publications of the Astronomical Society of the Pacific</u> **110**, 330–

338.

URL: *http://ukads.nottingham.ac.uk/cgi-bin/nph-bib_query?bibcode=*
1998PASP..110..330B&db_key=AST

Burns, B. E., Ionescu, A. C., Geneczko, J. M., Grasso, R. J. and Davidson, S. F.: 1997, Silicon spatial light modulator fabrication, Technical Digest of Spatial Light Modulator Conference, Lake Tahoe, pp. 87–89.

Cao, G. and Yang, Q.: 1997, Study of the bimorph deformable mirror, Proc. SPIE Vol. 3134, p. 138-147, Optical Manufacturing and Testing II, H. Philip Stahl; Ed., Vol. 3134, pp. 138–147.

URL: *http://ukads.nottingham.ac.uk/cgi-bin/nph-bib_query?bibcode=*
1997SPIE.3134..138C&db_key=INST

Collings, N.: 1999, Review of wavefront modulators and sensors for adaptive optics, Proceedings of 2nd International Workshop on Adaptive Optics for Industry and Medicine, p323-327, Gordon D. Love; Ed.

ComputerBoards Inc.: 1999, PCI-DAS08/JR Manual.

Dayton, D., Restaino, S., Gonglewski, J., Gallegos, J., McDermott, S., Browne, S., Rogers, S., Vaidyanathan, M. and Shilko, M.: 2000, Laboratory and field demonstration of a low cost membrane mirror adaptive optics system, Optics Communications **176**, 339–345.

URL: *http://ukads.nottingham.ac.uk/cgi-bin/nph-bib_query?bibcode=*
2000OptCo.176..339D&db_key=INST

Dicke, R. H.: 1975, Phase-contrast detection of telescope seeing errors and their correction, Astrophysical Joural **198**, 605–615.

URL: *http://ukads.nottingham.ac.uk/cgi-bin/nph-bib_query?bibcode=*
1975ApJ...198..605D&db_key=AST

Doel, A. P., Dunlop, C. N., Buscher, D. F., Myers, R. M., Sharples, R. M. and Major, J. V.: 2000, The MARTINI adaptive optics instrument, New Astronomy **5**, 223–233.

URL: *http://ukads.nottingham.ac.uk/cgi-bin/nph-bib_query?bibcode=*
2000NewA....5..223D&db_key=AST

Domenicali, P. L. and Hunter, G. C.: 1980, Optical interferometer system with cctv camera for measuring a wide range of aperture sizes, US Patent 4,201,473 .

Dyson, H. M., Sharples, R. M., Dipper, N. A. and Vdovin, G. V.: 2001, Cryogenic
wavefront correction using membrane deformable mirrors, Optics Express **8**(1).
URL: *http://www.opticsexpress.org/oearchive/source/29573.htm*

Farnell Catalogue: 1999.

Foy, R. and Labeyrie, A.: 1985, Feasibility of adaptive telescope with laser probe,
Astronomy and Astrophysics **152**, L29–L31.
URL: *http://ukads.nottingham.ac.uk/cgi-bin/nph-bib_query?bibcode=*
1985A%26A...152L..29F&db_key=AST

Ftaclas, C. and Kostinski, A.: 2001, Curvature sensors, adaptive optics, and Neumann
boundary conditions, Applied Optics **40**, 435–438.
URL: *http://ukads.nottingham.ac.uk/cgi-bin/nph-bib_query?bibcode=*
2001ApOpt..40..435F&db_key=INST

Gao, C., Ftaclas, C., Shelton, C. and Turner, N.: 2000, The Mount Wilson Adaptive
Optics Coronagraph, American Astronomical Society Meeting, Vol. 197, pp. 5206+.
URL: *http://ukads.nottingham.ac.uk/cgi-bin/nph-bib_query?bibcode=*
2000AAS...197.5206G&db_key=AST

Giovanelli, R., Darling, J., Sarazin, M., Yu, J., Harvey, P., Henderson, C., Hoffman,
W., Keller, L., Barry, D., Cordes, J., Eikenberry, S., Gull, G., Harrington, J.,
Smith, J. D., Stacey, G. and Swain, M.: 2001a, The Optical/Infrared Astro-
nomical Quality of High Atacama Sites. I. Preliminary Results of Optical Seeing,
Publications of the Astronomical Society of the Pacific **113**, 789–802.
URL: *http://ukads.nottingham.ac.uk/cgi-bin/nph-bib_query?bibcode=*
2001PASP..113..789G&db_key=AST

Giovanelli, R., Darling, J., Sarazin, M., Yu, J., Harvey, P., Henderson, C., Hoffman,
W., Keller, L., Barry, D., Cordes, J., Eikenberry, S., Gull, G., Harrington, J.,
Smith, J. D., Stacey, G. and Swain, M.: 2001b, The Optical/Infrared Astro-
nomical Quality of High Atacama Sites. I. Preliminary Results of Optical Seeing,
Publications of the Astronomical Society of the Pacific **113**, 789–802.
URL: *http://ukads.nottingham.ac.uk/cgi-bin/nph-bib_query?bibcode=*
2001PASP..113..789G&db_key=AST

Gonsalves, R. A.: 1976, Phase retrieval from modulus data, Journal of the Optical Society of America **66**(9), 961–964.

Gourlay, J., Love, G. D., Birch, P. M., Sharples, R. M. and Purvis, A.: 1998, A real-time closed-loop liquid cdrystal adaptive optics system: first results, Optics Communications **137**, 17–21.

Graves, J. E., Northcott, M. J., Roddier, F. J., Roddier, C. A. and Close, L. M.: 1998, First light for Hokupa'a: 36-element curvature AO system at UH, Proc. SPIE Vol. 3353, p. 34-43, Adaptive Optical System Technologies, Domenico Bonaccini; Robert K. Tyson; Eds., Vol. 3353, pp. 34–43.
URL: *http://ukads.nottingham.ac.uk/cgi-bin/nph-bib_query?bibcode= 1998SPIE.3353...34G&db_key=AST*

Graves, J. E., Northcott, M. J., Roddier, F. J., Roddier, C. A., Potter, D., O'Connor, D. J., Rigaut, F. J. and Chun, M. R.: 2000, First light for Hokupa'a 36 on Gemini North, Proc. SPIE Vol. 4007, p. 26-30, Adaptive Optical Systems Technology, Peter L. Wizinowich; Ed., Vol. 4007, pp. 26–30.
URL: *http://ukads.nottingham.ac.uk/cgi-bin/nph-bib_query?bibcode= 2000SPIE.4007...26G&db_key=AST*

Greenwood, D. P.: 1977, Bandwidth specification for adaptive optics systems, Optical Society of America Journal **67**, 390–393.
URL: *http://ukads.nottingham.ac.uk/cgi-bin/nph-bib_query?bibcode= 1977OSAJ...67..390G&db_key=INST*

Greenwood, D. P. and Fried, D. L.: 1976, Power spectra requirements for wave-front-compensative systems, Optical Society of America Journal **66**, 193–206.
URL: *http://ukads.nottingham.ac.uk/cgi-bin/nph-bib_query?bibcode= 1976OSAJ...66..193G&db_key=INST*

Greenwood, D. P. and Primmerman, C. A.: 1992, Adaptive optics research at Lincoln Laboratory, Lincoln Laboratory Journal **5**, 3–24.
URL: *http://ukads.nottingham.ac.uk/cgi-bin/nph-bib_query?bibcode= 1992LLabJ...5....3G&db_key=INST*

Hamdani, S.: 2001, The Adaptive Optics Project for the GI2T Interferometer, SF2A-2001: Semaine de l'Astrophysique Francaise, pp. E71–+.

URL: *http://ukads.nottingham.ac.uk/cgi-bin/nph-bib_query?bibcode=*
2001sf2a.confE..71H&db_key=AST

Hardy, J. W. (ed.): 1998, Adaptive optics for astronomical telescopes.
URL: *http://ukads.nottingham.ac.uk/cgi-bin/nph-bib_query?bibcode=*
1998aoat.conf.....H&db_key=AST

Hardy, J. W., Lefebvre, J. E. and Koliopoulos, C. L.: 1977, Real-time atmospheric compensation, Optical Society of America Journal **67**, 360–369.
URL: *http://ukads.nottingham.ac.uk/cgi-bin/nph-bib_query?bibcode=*
1977OSAJ...67..360H&db_key=INST

Hariharan, P.: 1988, Lateral and radial shearing interferometers: a comparison, Applied Optics **27**, 3594–3596.
URL: *http://ukads.nottingham.ac.uk/cgi-bin/nph-bib_query?bibcode=*
1988ApOpt..27.3594H&db_key=INST

Hidas, M. G., Burton, M. G., Chamberlain, M. A. and Storey, J. W. V.: 2000, Infrared and submillimetre observing conditions on the Antarctic Plateau, Publications of the Astronomical Society of Australia **17**, 260–269.
URL: *http://ukads.nottingham.ac.uk/cgi-bin/nph-bib_query?bibcode=*
2000PASA...17..260H&db_key=AST

Hippler, S., Kasper, M. E., Feldt, M., Weiss, R., Looze, D. P., Montoya, L., Aceituno, J., Ott, T. and Davies, R. I.: 2000, ALFA: three years of experience in adaptive optics with a laser guide star, Proc. SPIE Vol. 4007, p. 41-49, Adaptive Optical Systems Technology, Peter L. Wizinowich; Ed., Vol. 4007, pp. 41–49.
URL: *http://ukads.nottingham.ac.uk/cgi-bin/nph-bib_query?bibcode=*
2000SPIE.4007...41H&db_key=AST

Holota, W., Vdovin, G., Collings, N., Sodnik, Z., Sesselmann, R. and Manhart, S.: 1999, The Need of AO in Future Space Optical Instruments, Astronomy with adaptive optics : present results and future programs, pp. 235+.
URL: *http://ukads.nottingham.ac.uk/cgi-bin/nph-bib_query?bibcode=*
1999aaop.conf..235H&db_key=AST

Image Magick Studio: 2001.
URL: *http://www.ImageMagick.org*

Johnson, H. L.: 1962, Infrared Stellar Photometry., <u>Astrophysical Joural</u> **135**, 69+.

    URL: *http://ukads.nottingham.ac.uk/cgi-bin/nph-bib_query?bibcode=*

    1962ApJ...135...69J&db_key=AST

Jones, T. and Savage, D.: 1997.

    URL: *http://www.gsfc.nasa.gov/gsfc/service/gallery/fact_sheets/spacesci/hst-*

    cost.htm

Kendrick, R. L., Acton, D. S. and Duncan, A. L.: 1994, Phase-diversity wave-front sensor for imaging systems, <u>Applied Optics</u> **33**, 6533–6546.

    URL: *http://ukads.nottingham.ac.uk/cgi-bin/nph-bib_query?bibcode=*

    1994ApOpt..33.6533K&db_key=INST

Lee, M. K., Cowan, W. D., Welsh, B. M., Bright, V. M. and Roggemann, M. C.: 1998, Aberration-correction results from a segmented microelectromechanical deformable mirror and a refractive lenslet array, <u>Optics Letters</u> **23**, 645–647.

    URL: *http://ukads.nottingham.ac.uk/cgi-bin/nph-bib_query?bibcode=*

    1998OptL...23..645L&db_key=INST

Lena, P., Lebrun, F. and Mignard, F. (eds): 1998, <u>Observational astrophysics</u>, Springer Astronomy and Astrophysics Library, Berlin: Springer.

    URL: *http://ukads.nottingham.ac.uk/cgi-bin/nph-bib_query?bibcode=*

    1998obas.conf.....L&db_key=AST

Lloyd-Hart, M., Wildi, F. P., Martin, B., McGuire, P. C., Kenworthy, M. A., Johnson, R. L., Fitz-Patrick, B. C., Angeli, G. Z., Miller, S. M. and Angel, J. R. P.: 2000, Adaptive optics for the 6.5-m MMT, <u>Proc. SPIE Vol. 4007, p. 167-174, Adaptive Optical Systems Technology, Peter L. Wizinowich; Ed.</u>, Vol. 4007, pp. 167–174.

    URL: *http://ukads.nottingham.ac.uk/cgi-bin/nph-bib_query?bibcode=*

    2000SPIE.4007..167L&db_key=AST

Loktev, M., De Lima Monteiro, D. W. and Vdovin, G.: 2001, Comparison study of the performance of piston, thin plate and membrane mirrors for correction of turbulence-induced phase distortions, <u>Optics Communications</u> **192**, 91–99.

    URL: *http://ukads.nottingham.ac.uk/cgi-bin/nph-bib_query?bibcode=*

    2001OptCo.192...91L&db_key=INST

Love, G. D.: 1997, Wave-front correction and production of Zernike modes with a liquid-crystal spatial light modulator, Applied Optics 36, 1517–1524.
URL: *http://ukads.nottingham.ac.uk/cgi-bin/nph-bib_query?bibcode=*
1997ApOpt..36.1517L&db_key=INST

Marquardt, E. D., Le, J. P. and Radebaugh, R.: 2000, Cryogenic material properties database, Proceedings of the 11th International Cryocooler Conference (in press).
URL: *http://cryogenics.nist.gov/Cryo_Materials.pdf*

Masciadri, E. and Garfias, T.: 2001, Wavefront coherence time seasonal variability and forecasting at the San Pedro Mártir site, Astronomy and Astrophysics 366, 708–716.
URL: *http://ukads.nottingham.ac.uk/cgi-bin/nph-bib_query?bibcode=*
2001A%26A...366..708M&db_key=AST

Max, C. E.: 2000, Laser Guide Star Operational Issues, Laser Guide Star Adaptive Optics for Astronomy, Edited by N. Ageorges, and C. Dainty. Kluwer Academic Publishers (Dordrecht), 2000., p.89, pp. 89+.
URL: *http://ukads.nottingham.ac.uk/cgi-bin/nph-bib_query?bibcode=*
2000lgsa.conf...89M&db_key=AST

NASA: 2001, Next generation space telescope.
URL: *http://ngst.gsfc.nasa.gov/*

Oppenheimer, B. R., Palmer, D., Dekany, R. and Sivaramakrishnan, A.: 1997, Investigations of a xinetics deformable mirror, Proceedings of the SPIE, Vol. 3126, pp. 569–579.

Oxford Instruments, p.: 2002.
URL: *http://www.oxinst.com*

Paik, D., Park, S. and Shrout, T. R.: 1999, Dielectric and piezoelectir properties of perovskite materials at cryogenic temperatures, Journal of Materials Science 34(3), 469–473.

Paterson, C., Munro, I. H. and Dainty, C.: 2000, A low cost adaptive optics system using a membrane mirror, Optics Express 6(9).

Paxman, R. G. and Fienup, J. R.: 1988, Optical misalignment sensing and image reconstruction using phase diversity, Optical Society of America Journal 5, 914–923.

URL: *http://ukads.nottingham.ac.uk/cgi-bin/nph-bib_query?bibcode=*
1988OSAJ....5..914P&db_key=INST

Paxman, R. G., Schulz, T. J. and Fienup, J. R.: 1992, Joint estimation of object and aberrations by using phase diversity, <u>Optical Society of America Journal</u> **9**, 1072–1085.
URL: *http://ukads.nottingham.ac.uk/cgi-bin/nph-bib_query?bibcode=*
1992OSAJ....9.1072P&db_key=INST

Platt, J. R.: 1957, Increase of Telescope Resolution with Time-Selection with an Image-Forming Stellar Interferometer., <u>Astrophysical Joural</u> **125**, 601+.
URL: *http://ukads.nottingham.ac.uk/cgi-bin/nph-bib_query?bibcode=*
1957ApJ...125..601P&db_key=AST

Press, W. H.: 1993, Books-Received - Numerical Recipes in C - ED.2, <u>Science</u> **259**, 1931+.
URL: *http://ukads.nottingham.ac.uk/cgi-bin/nph-bib_query?bibcode=*
1993Sci...259Q1931P&db_key=AST

Quirrenbach, A.: 2000, Adaptive Optics with Laser Guide Stars: Basic Concepts and Limitations, <u>Laser Guide Star Adaptive Optics for Astronomy, Edited by N. Ageorges, and C. Dainty. Kluwer Academic Publishers (Dordrecht), 2000., p.23</u>, pp. 23+.
URL: *http://ukads.nottingham.ac.uk/cgi-bin/nph-bib_query?bibcode=*
2000lgsa.conf...23Q&db_key=AST

Ragazzoni, R.: 1996, Pupil plane wavefront sensing with an oscillating prism, <u>Journal Of Modern Optics</u> **43**(2), 289–293.

Ragazzoni, R., Ghedina, A., Baruffolo, A., Marchetti, E., Farinato, J., Niero, T., Crimi, G. and Ghigo, M.: 2000, Testing the pyramid wavefront sensor on the sky, <u>Proc. SPIE Vol. 4007, p. 423-430, Adaptive Optical Systems Technology, Peter L. Wizinowich; Ed.</u>, Vol. 4007, pp. 423–430.
URL: *http://ukads.nottingham.ac.uk/cgi-bin/nph-bib_query?bibcode=*
2000SPIE.4007..423R&db_key=AST

Restaino, S. R., Baker, J. T., Dayton, D. C. and Finkner, L. G.: 2000, Experimental results from an adaptive optics system based on a dual frequency nematic device, <u>Proc. SPIE Vol. 3955, p. 54-57, Liquid Crystal Materials, Devices, and Flat Panel Displays, Ranganathan Shashidhar; Bruce Gnade; Eds.</u>, Vol. 3955, pp. 54–57.

URL: *http://ukads.nottingham.ac.uk/cgi-bin/nph-bib_query?bibcode=*
2000SPIE.3955...54R&db_key=INST

Rigaut, F.: 1996, Review of astronomical adaptive optics systems on medium-sized (1.5–
5m) telescopes, <u>OSA Topical meeting on adaptive optics 1996</u>.
URL: *http://www.cfht.hawaii.edu/Instruments/Imaging/AOB/survey.html*

Rigaut, F. J., Ellerbroek, B. L. and Flicker, R.: 2000, Principles, limitations, and per-
formance of multiconjugate adaptive optics, <u>Proc. SPIE Vol. 4007, p. 1022-1031,</u>
<u>Adaptive Optical Systems Technology, Peter L. Wizinowich; Ed.</u>, Vol. 4007, pp. 1022–
1031.
URL: *http://ukads.nottingham.ac.uk/cgi-bin/nph-bib_query?bibcode=*
2000SPIE.4007.1022R&db_key=AST

Rigaut, F., Salmon, D., Arsenault, R., Thomas, J., Lai, O., Rouan, D., Véran, J. P.,
Gigan, P., Crampton, D., Fletcher, J. M., Stilburn, J., Boyer, C. and Jagourel, P.:
1998, Performance of the Canada-France-Hawaii Telescope Adaptive Optics Bon-
nette, <u>Publications of the Astronomical Society of the Pacific</u> **110**, 152–164.
URL: *http://ukads.nottingham.ac.uk/cgi-bin/nph-bib_query?bibcode=*
1998PASP..110..152R&db_key=AST

Rimmele, T. R.: 2000, Solar adaptive optics, <u>Proc. SPIE Vol. 4007, p. 218-231, Adaptive</u>
<u>Optical Systems Technology, Peter L. Wizinowich; Ed.</u>, Vol. 4007, pp. 218–231.
URL: *http://ukads.nottingham.ac.uk/cgi-bin/nph-bib_query?bibcode=*
2000SPIE.4007..218R&db_key=AST

Rimmele, T. R., Radick, R. R., Richards, K. and Dunn, R. B.: 1999, The NSO Solar
Adaptive Optics Program: First Results., <u>American Astronomical Society Meeting</u>,
Vol. 194, pp. 10307+.
URL: *http://ukads.nottingham.ac.uk/cgi-bin/nph-bib_query?bibcode=*
1999AAS...19410307R&db_key=AST

Roberts, S., Fitzsimmons, J. T., Szeto, K., Anthony, A., Siddall, G., Gaunt, R., Shott,
P., Sebesta, J., Taylor, K. and Duncan, D.: 2000, Mechanical design of Altair, the
Gemini-North adaptive optics system, <u>Proc. SPIE Vol. 4008, p. 956-967, Optical</u>
<u>and IR Telescope Instrumentation and Detectors, Masanori Iye; Alan F. Moorwood;</u>
<u>Eds.</u>, Vol. 4008, pp. 956–967.

URL: *http://ukads.nottingham.ac.uk/cgi-bin/nph-bib_query?bibcode=*
2000SPIE.4008..956R&db_key=AST

Roche, P.: 2000.
URL: *http://gemini.physics.ox.ac.uk/misc/uk-involvement.html*

Roddier, F.: 1987, Curvature sensing: A diffraction theory, NOAO R&D Note 87-3 .

Roddier, F.: 1988, Curvature sensing and compensation - a new concept in adaptive optics, Applied Optics **27**(7), 1223–1225.

Roddier, F.: 1995, Error propagation in a closed-loop adaptive optics system - a comparison between shack-hartmann and curvature wave-front sensors, Optical Communications **113**(4-6), 357–359.

Roddier, F. (ed.): 1999, Adaptive Optics in Astronomy, Cambridge University Press.

Roddier, F. J.: 1991, Wavefront curvature sensing and compensation methods in adaptive optics, Proc. SPIE Vol. 1487, p. 123-128, Propagation Engineering: Fourth in a Series, Luc R. Bissonnette; Walter B. Miller; Eds., Vol. 1487, pp. 123–128.
URL: *http://ukads.nottingham.ac.uk/cgi-bin/nph-bib_query?bibcode=*
1991SPIE.1487..123R&db_key=INST

Roddier, N. and Roddier, F.: 1989, Curvature sensing and compensation - A computer simulation, Active telescope systems; Proceedings of the Meeting, Orlando, FL, Mar. 28-31, 1989 (A90-30852 12-74). Bellingham, WA, Society of Photo-Optical Instrumentation Engineers, 1989, p. 92-96. Research sponsored by Kaman Aerospace Corp., Vol. 1114, pp. 92–96.
URL: *http://ukads.nottingham.ac.uk/cgi-bin/nph-bib_query?bibcode=*
1989SPIE.1114...92R&db_key=AST

Roth, K. C., Guyon, O., Chun, M., Jensen, J. B., Jorgensen, I., Rigaut, F. and Walther, D. M.: 2001, Hokupa'a Performance and Point Spread Function Characterization, American Astronomical Society Meeting **198**.
URL: *http://ukads.nottingham.ac.uk/cgi-bin/nph-bib_query?bibcode=*
2001AAS...198.0202R&db_key=AST

Rousset, G., Fontanella, J. C., Kern, P., Gigan, P. and Rigaut, F.: 1990, First diffraction-limited astronomical images with adaptive optics, Astronomy and Astrophysics

230, L29–L32.

URL: *http://ukads.nottingham.ac.uk/cgi-bin/nph-bib_query?bibcode=*
1990A%26A...230L..29R&db_key=AST

Sandler, D. G., Cuellar, L., Lefebvre, M., Barrett, T., Arnold, R., Johnson, P., Rego, A., Smith, G., Taylor, B. and Spiv, G.: 1994, Shearing interferometry for laser-guide-star atmospheric correction at large D/r¡SUB¿0¡/SUB¿, J. Opt. Soc. Am. A, vol. 11, issue 2, page 858 **11**, 858+.

URL: *http://ukads.nottingham.ac.uk/cgi-bin/nph-bib_query?bibcode=*
1994OSAJA..11..858S&db_key=INST

Sasiela, R. J.: 1994, Electromagnetic wave propagation in turbulence. Evaluation and application Springer Series on Wave Phenomena, Berlin: Springer, 1994.

URL: *http://ukads.nottingham.ac.uk/cgi-bin/nph-bib_query?bibcode=*
1994ewpt.book.....S&db_key=AST

Schmutz, L. E., Bowker, J. K., Feinleib, J., Landon, S. N. and Tubbs, S. J.: 1980, Experimental performance of the I3 wavefront sensor for closed-loop adaptive optics, Active optical devices and applications; Proceedings of the Seminar, Washington, DC, April 10, 11, 1980. (A81-37719 17-74) Bellingham, WA, Society of Photo-Optical Instrumentation Engineers, 1980, p. 14-20. USAF-sponsored research., Vol. 228, pp. 14–20.

URL: *http://ukads.nottingham.ac.uk/cgi-bin/nph-bib_query?bibcode=*
1980SPIE..228...14S&db_key=INST

Schott Glass Technologies, Inc.: 1998, Filter Glass Catalogue, 400 York Avenue, Duryea, PA 18642, USA.

Shackleford, J. F. e.: 1997, CRC Materials Science and Engineering Handbook.

Soedel, W.: 1981, Vibrations of shells and plates.

Soobitsky, J. A.: 1985, Micromotion actuator, EU Patent 0 147 534 .

Southwell, W. H.: 1981, Validity of the Fresnel approximation in the near field, Optical Society of America Journal **71**, 7+.

URL: *http://ukads.nottingham.ac.uk/cgi-bin/nph-bib_query?bibcode=*
1981OSAJ...71....7S&db_key=INST

Stambulchik, E.: 2000, Grace.
URL: *http://plasma-gate.weizmann.ac.il/Grace*

Strojnik, M. and Paez, G.: 1999, Simulated interferometric patterns generated by a nearby star-planet system and detected by a rotational shearing interferometer, Optical Society of America Journal **16**, 2019–2024.
URL: *http://ukads.nottingham.ac.uk/cgi-bin/nph-bib_query?bibcode= 1999OSAJ...16.2019S&db_key=INST*

Sziklas, E. A. and Siegman, A. E.: 1975, Mode calculations in unstable resonators with flowing saturable gain. 2: Fast Fourier transform method, Applied Optics **14**, 1874–1889.
URL: *http://ukads.nottingham.ac.uk/cgi-bin/nph-bib_query?bibcode= 1975ApOpt..14.1874S&db_key=INST*

Szmyrka-Grzebyk, A. and Lipinski, L.: 1995, Linear diode thermometer in the 4-300 k temperature range, Cryogenics **35**(4), 281–284.

Takami, H.: 2001, Subaru AO 1¡SUP¿st¡/SUP¿ light, Beyond Conventional Adaptive Optics.
URL: *http://ukads.nottingham.ac.uk/cgi-bin/nph-bib_query?bibcode= 2001bcao.confE..63T&db_key=AST*

Trueblood, M.: 1999, Usgp instrument program.
URL: *http://www.noao.edu/noao/noaonews/sep99/node50.html*

Tyler, G. A.: 1994, Bandwidth considerations for tracking through turbulence, J. Opt. Soc. Am. A, vol. 11, issue 1, page 358 **11**, 358+.
URL: *http://ukads.nottingham.ac.uk/cgi-bin/nph-bib_query?bibcode= 1994OSAJA..11..358T&db_key=INST*

Tyson, R. K. (ed.): 2000, Adaptive Optics Engineering Handbook, Adaptive Optics Engineering Handbook, Publisher: Marcel Decker, Inc., 2000, ISBN: 0824782755.

Underwood, K., Wyant, J. C. and Koliopoulos, C. L.: 1983, Self-referencing wavefront sensor, Vol. 351, pp. 108–114.

Vdovin, G.: 2001a, Private Communication .

Vdovin, G.: 2001b, Flexible optical.

> **URL:** *http://www.okotech.com*

Vdovin, G., Middelhoek, S. and Sarro, P. M.: 1997, Technology and applications of micromachined silicon adaptive mirrors, Optical Engineering **36**(5), 1382–1390.

Vdovin, G. V.: 1996, Adaptive mirror micromachined in silicon, Delft, The Netherlands: Delft University.

> **URL:** *http://ukads.nottingham.ac.uk/cgi-bin/nph-bib_query?bibcode=*
> *1996amms.book.....V&db_key=AST*

Vdovin, G. V.: 1998, Optimization-based operation of micromachined deformable mirrors, Proc. SPIE Vol. 3353, p. 902-909, Adaptive Optical System Technologies, Domenico Bonaccini; Robert K. Tyson; Eds., Vol. 3353, pp. 902–909.

> **URL:** *http://ukads.nottingham.ac.uk/cgi-bin/nph-bib_query?bibcode=*
> *1998SPIE.3353..902V&db_key=AST*

Vdovin, G. V.: 2001c, Lightpipes beam propogation toolbox.

> **URL:** *http://www.okotech.com/pipes/index.php3*

Vdovin, G. V.: 2001d, Mmdm with 5 to 15mm apertures.

> **URL:** *http://www.okotech.com/mirrors/small.php3*

Vdovin, G. V. and Sarro, P. M.: 1995, Flexible mirror micromachined in silicon, Applied Optics **34**, 2968–2972.

Vdovin, G. V., Sarro, P. M. and Middelhoek, S.: 1999, Technology and applications of micromachined adaptive mirrors, Journal of Micromechanics and Microengineering **9**, R8–R20.

Weast, R. C. e.: 1975-1976, Handbook of Chemistry and Physics 56th Edition, CRC Press.

White, H. E. and White, D. H.: 1980, Physics and Music.

Willard, B. C.: 1993, Rotational shearing interferometer, Applied Optics **32**, 7118+.

> **URL:** *http://ukads.nottingham.ac.uk/cgi-bin/nph-bib_query?bibcode=*
> *1993ApOpt..32.7118W&db_key=INST*

Zygo Corporation: 1992, ZyMOD/PC Phase Shift Adapter, Laurel Brook Road, PO Box 448, Middlefield, CT 06455, USA.